# ABSTRACT

Title of thesis: REFINED PERFORMANCE AND LOADS OF A MACH-SCALE ROTOR AT HIGH ADVANCE RATIOS

Lauren N. Trollinger, Master of Science, 2017

Thesis directed by: Professor Inderjit Chopra
Department of Aerospace Engineering

This work will investigate the performance and vibratory loads of a Mach-scale rotor with highly similar, non-instrumented blades at advance ratios ($\mu$) up to 0.9. Wind tunnel tests were performed on a 4-bladed, articulated rotor with a diameter of 2.78 ft. The slowed rotor was operated at 30%, 40%, and 50% of nominal speed, corresponding to advancing tip Mach numbers up to 0.53, and shaft tilt angles of -4°, 0°, and 4° were tested. Collective sweeps from -2° to 12° were performed for each flight condition, and blade motion, control cyclics, and hub loads were measured. Blade similarity was shown to improve rotor track and trim at high $\mu$. Thrust reversal was observed at $\mu = 0.9$, but positive (aft) shaft tilt increased lift at high $\mu$. Vibratory hubloads are shown to increase with advance ratio. Correlations performed using the comprehensive analysis code UMARC show good agreement for rotor performance.

# REFINED PERFORMANCE AND LOADS OF A MACH-SCALE ROTOR AT HIGH ADVANCE RATIOS

by

Lauren N. Trollinger

Thesis submitted to the Faculty of the Graduate School of the
University of Maryland, College Park in partial fulfillment
of the requirements for the degree of
Master of Science
2017

Advisory Committee:
Professor Inderjit Chopra, Chair
Professor Anubhav Datta
Professor Anya Jones

© Copyright by
Lauren N. Trollinger
2017

# Acknowledgments

In my first semester at Maryland, Dr. Chopra hired me to work on the Human-Powered Helicopter team. Being a part of the Gamera family was an experience that cemented my interest in rotorcraft, and I cannot thank Dr. Chopra enough for all of the guidance, the wisdom, and the opportunities he has given me since.

I must also thank my other committee members, Dr. Anubhav Datta and Dr. Anya Jones, for their constant willingness to share their knowledge and advice.

I am exceedingly grateful to Dr. Alison Flatau for exposing me to research and for being such a wonderful professor, mentor, and adviser; her drive to encourage women in STEM is something I will not soon forget.

Thank you to everyone in and around the lab, for your friendship and for the long days in the wind tunnel: Xing, Vikram, VT, Peter, Andrew, Jon, Brandyn, Fred, Dan, and Peter Ryseck. Thank you to Andrew Lind and the STAL crew, who made two hard weeks of testing fun. Of course, the assistance of the GLMWT personnel — Dr. Barlow, Ahmad, Alex, and Noah — was absolutely invaluable.

I am incredibly fortunate to have met so many people and made so many friends during my time at Maryland; thank you all for your friendship, the long nights spent working much too late, and for making the last two years so much fun.

Finally, I must thank my family, my parents and my sister, for so much love and laughter. And more than anything, I must thank my boyfriend Gary for his unyielding support, and for spending his only free weekend in Manufacturing when I was too busy with Design. I can't wait for our next adventure in Boston.

# Table of Contents

# List of Tables



# List of Figures

# List of Abbreviations

| | |
|---|---|
| $a$ | Sectional airfoil lift-curve slope, $rad^{-1}$ |
| $A_{rotor}$ | Rotor disk area, $\pi R^2$ |
| $A_{tunnel}$ | Wind tunnel test section area |
| $c$ | Blade chord |
| $c_d$ | Sectional drag coefficient |
| $c_l$ | Sectional lift coefficient |
| $C_D$ | Drag coefficient, $\frac{D}{\rho A(\Omega R)^2}$ |
| $C_{De}$ | Equivalent drag coefficient, $\frac{C_P}{\mu} + C_D$ |
| $C_H$ | H-force coefficient, $\frac{H}{\rho A(\Omega R)^2}$ |
| $C_L$ | Lift coefficient, $\frac{L}{\rho A(\Omega R)^2}$ |
| $C_P$ | Shaft power coefficient, $\frac{P}{\rho A(\Omega R)^3}$ |
| $C_Q$ | Torque coefficient, $\frac{Q}{\rho A(\Omega R)^2 R}$ |
| $C_T$ | Thrust coefficient, $\frac{T}{\rho A(\Omega R)^2}$ |
| $D_e$ | Rotor equivalent drag force |
| $f$ | Frequency, Hz |
| $L$ | Rotor lift force |
| $\frac{L}{D_e}$ | Rotor lift-to-drag ratio |
| $N_b$ | Number of rotor blades |
| $P, /rev$ | Frequency per revolution, $\frac{2\pi f}{\Omega}$ |
| $R$ | Rotor radius |
| $U_\infty$ | Freestream velocity |
| $X$ | Rotor longitudinal axis, parallel to disk, positive aft |
| $Y$ | Rotor lateral axis, parallel to disk, positive starboard |
| $Z$ | Rotor vertical axis, normal to disk, positive up |
| | |
| $\alpha$ | Angle of attack |
| $\alpha_s$ | Rotor shaft tilt angle, positive aft |
| $\beta$ | Blade flapping angle |
| $\beta_{1C}$ | Longitudinal flapping angle, $cos(\psi)$ |
| $\beta_{1S}$ | Lateral flapping angle, $sin(\psi)$ |
| $\gamma$ | Lock number |
| $\theta$ | Blade pitch angle |
| $\theta_0$ | Rotor collective pitch angle, at root |
| $\theta_{1C}$ | Rotor lateral pitch angle, $cos(\psi)$ |
| $\theta_{1S}$ | Rotor longitudinal pitch angle, $sin(\psi)$ |
| $\mu$ | Advance ratio, $\frac{U_\infty cos(\alpha_s)}{\Omega R}$ |
| $\rho$ | Air density |
| $\sigma$ | Rotor solidity, $\frac{A_b}{A}$ |
| $\psi$ | Rotor blade azimuth, degrees |
| $\omega$ | Frequency, $rad/s$ |
| $\Omega$ | Rotor angular velocity, $rad/s$ |

| | |
|---|---|
| AGRC | Alfred Gessow Rotorcraft Center |
| BET | Blade element theory |
| CFD | Computational fluid dynamics |
| CSD | Computational structural dynamics |
| DAQ | Data acquisition system |
| FFT | Fast Fourier transform |
| GLMWT | Glenn L. Martin Wind Tunnel |
| RPM | Revolutions per minute |
| TPP | Tip path plane |
| UMD | University of Maryland |
| UMARC | University of Maryland Advanced Rotorcraft Code |

# Chapter 1: Introduction

Helicopters are inherently unique in the world of aircraft; the ability to take-off and land vertically and to maintain hovering flight enables an enormously beneficial operational envelope and allows a range of applications. Hover-capable aircraft that are runway independent and permit efficient low-speed operation can facilitate rescue missions, precision cargo and package delivery, and steady, sustained reconnaissance that fixed-wing aircraft are unable to accomplish. These abilities, however, come at a cost: because the design of an optimal hovering vehicle directly conflicts with that of a vehicle optimized for efficient forward flight, helicopters have traditionally been limited in forward flight speed and efficiency. Now, the focus in the rotorcraft industry has shifted toward the development of high-speed configurations that simultaneously possess the efficient low-speed operational capabilities that make helicopters unique.

Over the last few years, there has been an industry-wide push for faster, high-speed rotorcraft capable of operation over 250 knots. The current DARPA (Defense Advanced Research Projects Agency) challenge calls for a VTOL X-Plane capable of both high hover efficiency and sustained forward flight speeds of more than 300 knots [1]. This push is necessary because the flight envelope of conventional helicopters

with edgewise rotors has traditionally been limited at high forward flight speeds by compressibility effects on the advancing side as well as reverse flow and dynamic stall on the retreating side. Slowing the rotor can minimize these compressibility effects and decrease the profile power, but also results in high advance ratio ($\mu$) that can cause loss of lift on the retreating side and high vibratory loads.

This work will begin by providing a more detailed background on the challenges associated with high advance ratio flight because of slowed rotors, focusing in particular on experimental studies that have been performed. While many numerical and computational studies of high $\mu$ flight have been attempted over the years, comprehensive experimental studies are needed to validate these predictive methodologies. Many existing analyses rely on certain assumptions, such as blade similarity, that may not be strictly possible in experimental testing. There is a need to investigate the dynamics of a single rotor at high speeds to understand the effects of blade similarity on tracking and trimming at high advance ratio. The objective, scope, and contributions of the current research is discussed at the end of this chapter.

## 1.1 Background and Motivation

Conventional helicopters are limited in their ability to achieve high speed flight by factors such as retreating blade dynamic stall and reverse flow as well as compressibility effects on the advancing side. This is illustrated in Fig. 1.1: in hover, when the helicopter is not moving forward (1.1(a)), the rotor is under the influ-

ence of symmetric flow distribution. As the helicopter transitions into forward flight (1.1(b)), that additional velocity adds to the rotor angular velocity, increasing the combined rotor speed on the advancing side and decreasing the total speed on the retreating side. This imbalance in lift causes a roll moment on the rotor, and the blade pitch on the retreating side must therefore be increased to preserve lift and maintain roll equilibrium.

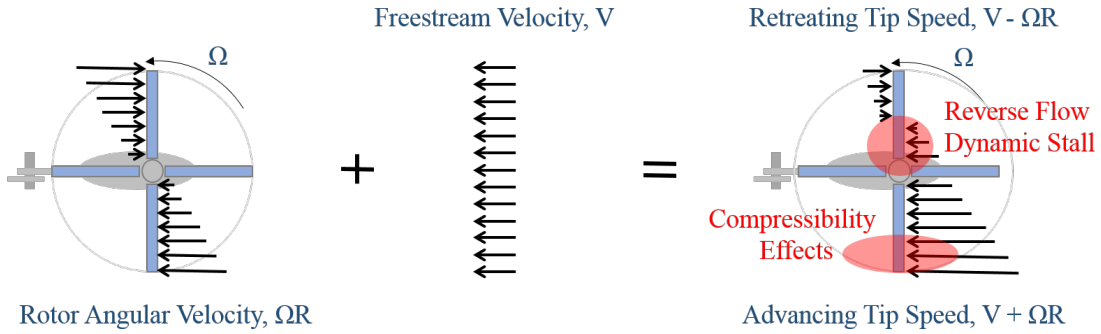


Figure 1.1: Effects of high speed forward flight on a conventional edgewise rotor.

There are multiple challenges associated with this high speed flight regime:

- **Compressibility Effects:** First, conventional edgewise rotors at high speeds experience compressibility effects on the advancing side blade tip. As the combined velocity on the advancing side increases, the flow over the airfoil begins to approach its critical Mach number. Typical modern-day helicopters, such as the military's UH-60 Blackhawk, operate at hovering tip Mach numbers of approximately 0.65; thus, even moderate forward flight speeds can result in transonic flow and even local shocks over the advancing blade tip. This results

in a sharp increase in sectional airfoil drag, large pitching moments, and high levels of vibration.

- **Dynamic Stall:** Another problem is retreating blade dynamic stall, which occurs when retreating blade pitch is increased with forward flight speed. At sufficiently high pitch angles, the retreating blade reaches its critical angle of attack and experiences dynamic stall. During the onset of retreating blade dynamic stall, there is a very large increase in vibratory loads and significant degradation of handling quality and flight dynamics.

- **Reverse Flow:** A third consideration when operating edgewise rotors at high speeds is reverse flow. At high forward flight velocities, the oncoming flow exceeds the rotor's rotational speed and results in reverse flow, which travels from the geometric trailing edge of the blade to the leading edge, in the region near the root of the blade. The reverse flow region causes a significant increase in blade pitching moment and vibration that can severely impact rotor performance.

The aforementioned challenges are all aggravated by higher forward flight velocities. One method of reducing compressibility effects is to slow the rotor RPM such that the advancing blade tip Mach number is lower than the critical Mach number. Slowing the rotor minimizes compressibility effects and maintains a lower profile power, but also results in high advance ratio that can cause a net loss of lift and more vibratory loads. Compound helicopter configurations can overcome these limitations by adding supplemental lifting surfaces, additional rotors, or auxiliary

propellers; adding additional lift and thrust offloads the main rotor enough to allow the rotor RPM to be slowed.


Figure 1.2: The Optimum Speed Rotor concept, developed by Karem, was implemented on the A160 Hummingbird to achieve variable rotor speed.

There are, however, additional problems associated with the use of slowed rotors. Modern helicopter engines and transmissions are typically incapable of maintaining efficient operation (less than 5% variation from minimum specific fuel consumption) with more than 15-20% change from nominal rotor RPM [2]. While there are a few exceptions, like the Optimum Speed Rotor concept patented by Karem [3] and tested on the A160 Hummingbird shown in Fig. 1.2, where the rotor speed was slowed by more than 50% [4]. Variable-speed engine technology is not available at this time, and this presents many challenges. The Army Aviation Technology Directorate is attempting to address this challenge, beginning a program in 2016 to develop a transmission system capable of 50% reduction in rotor speed [5]. The rotors must be modified as well, because variable-speed rotors need to be stiffened

to avoid the possibility of resonance as the rotor RPM is changed.

a) Sikorsky X2 Demonstrator


b) Sikorsky S-97 RAIDER

Figure 1.3: Modern coaxial helicopters with augmented propulsive thrust.

a) Cartercopter PAV

b) Airbus Helicopter $X^3$

Figure 1.4: Lift-compound configurations with additional fixed-wing surfaces.

To counter the lift imbalance induced by single rotor configurations, modern coaxial helicopters utilize rigid contra-rotating rotors to balance the roll moment induced by high speed flight. Additionally, a pusher propeller is used to provide propulsive thrust. Sikorsky Aircraft, a division of the Lockheed Martin Corporation, has incorporated this technology into many of their products, like the X-2 Technology Demonstrator [6] and the S-97 Raider [7] shown in Fig. 1.3.

As shown in Fig. 1.4, lift-compound rotorcraft have been developed that utilize additional lifting surfaces to offload the slowed rotors in high speed flight, such as

Carter Aviation's Personal Air Vehicle [8] and Airbus Helicopter's $X^3$ [9].

The aeromechanics of a rotor at high advance ratios, which involves the coupled structural, aerodynamic, and inertial response, is not yet completely understood at very high advance ratios. Typically, legacy helicopters have not exceeded advance ratios above $\mu = 0.4$; this is because of many dynamics, performance, and flight dynamics issues associated with high advance ratios. Additionally, high advance ratio flight (above $\mu = 0.8$) causes many critical phenomena such as thrust reversal, reverse flow, and high vibratory loads, all of which impact the performance of the rotor. While numerical models have been created to predict the aeromechanics of a rotor at high advance ratio, these have not been optimally validated because of limited comprehensive experimental data for advance ratios above $\mu = 0.5$. High quality experimental studies must be continue to be performed to create a dataset that can be used to validate these predictive models. This work investigates the aeromechanics of a slowed rotor by obtaining experimental test data for a rotor with a highly similar set of blades at advance ratios up to 0.9.

## 1.2 Previous Work in High Advance Ratio Flight

Slowing the rotor to achieve high advance ratios has been investigated by researchers in industry, government, and academia to further the development of high speed rotorcraft. This section will provide a detailed review of previous work involving high advance ratio experimental testing, followed by a review of analytical studies and predictive models that have been developed as design tools for future

high speed rotorcraft.

### 1.2.1 Experimental Investigations

Wheatley and Hood (1935) performed wind tunnel experiments on an isolated Pitcairn PCA-2 autogiro rotor in the full-scale Langley Research facility in 1933, obtaining force and airloads data for the rotor [10]. The unpowered rotor (Fig. 1.5) was started using the wind tunnel jet stream, and several rotor speeds were tested for each of three collective pitch settings to achieve advance ratios between 0.1 and 0.7. Rotor lift-to-drag ratio was observed to reach a maximum of approximately 7.0 at about $\mu = 0.35$ regardless of pitch setting. Blade tracking was achieved by slowly lowering a paint brush from above the rotor disk to mark the blade (or blades) with the highest flapping angle, thereby observing which blades were out-of-track.

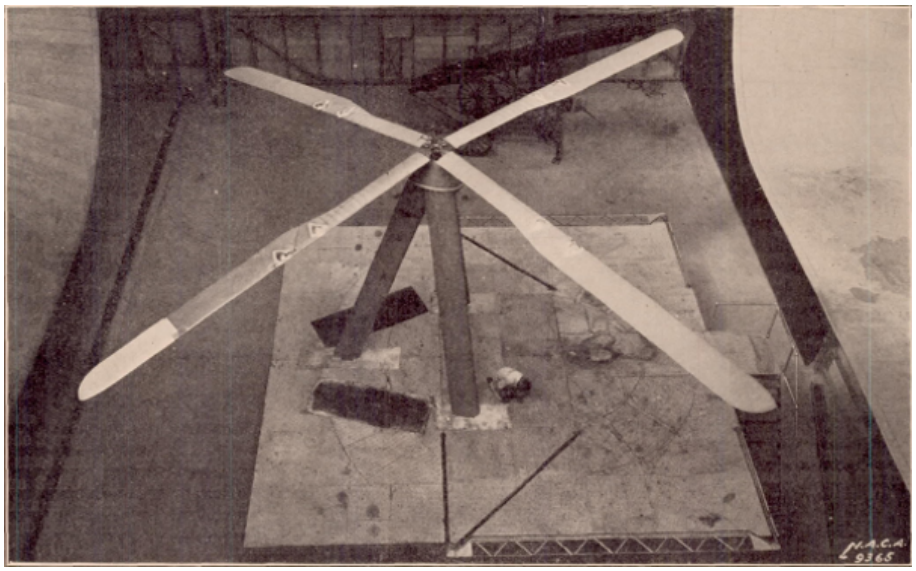


Figure 1.5: The isolated PCA-2 autogiro rotor tested in the Langley Aeronautical Laboratory full-scale wind tunnel in 1933.

Adjustments of the pitch links were then made, and the process was repeated until the blade tips were within 1.5 inches of one another.

Jenkins and Sweet (1963-1965) tested a 15-foot-diameter rotor in the Langley Research Center's full-scale wind tunnel to investigate the performance of a rotor at high collectives [11] and at high advance ratios [12].

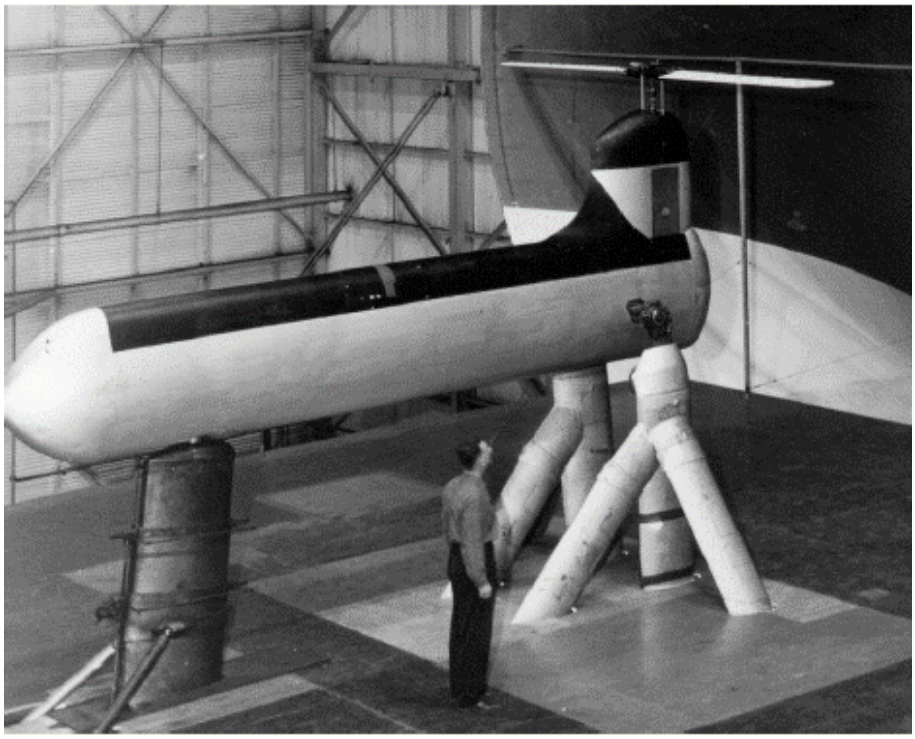

Figure 1.6: Jenkins and Sweet wind tunnel tested a 15 ft diameter teetering rotor at advance ratios up to 1.45 at the Langley Research Center [12].

The two-blade, teetering rotor shown in Fig. 1.6 utilized an untwisted, untapered NACA 0012 airfoil to explore rotor performance at advance ratios from 0.65 to 1.45 and measured rotor forces, rotor controls, and flapping motion. Additional results were obtained by varying longitudinal shaft tilt to affect rotor lift-to-drag ratio. The blade structural and inertial properties were not provided. Jenkins et

al. obtained the first experimental evidence of rotor thrust reversal, noting that the slope of thrust versus collective angle became negative for advance ratios around 1.0.

McCloud, Biggers, and Stroub (1968) tested five full-scale rotors at advance ratios of 0.3 to 1.05 in the NASA Ames 40 ft x 80 ft wind tunnel [13]. Four of the five rotors had NACA 0012 airfoil geometries; four of the rotors had no taper, while the fifth included linear chordwise taper plus added camber to the outer 20% radius of the blades. The set of wind tunnel tests varied blade twist, blade tip shape, and rotor articulation to obtain rotor hub forces and moments, shaft torque, rotor flap angles, and control settings at high advance ratios. Two 56 ft diameter, fully articulated rotors, one with twist and one without, were tested along with two teetering rotors, one with a 24 ft blade radius and another with a 17 ft radius, up to advance ratios of 1.05 and advancing tip Mach numbers up to 1.00. The fifth teetering rotor was 48 ft in diameter and incorporated linear taper as well as a NACA 21006 airfoil section at the blade tip. While the average flap inertia and the geometric properties of the blades are given, the individual blade stiffnesses and masses are not provided. Each test adjusted the tunnel speed and rotor RPM to achieve a set advance ratio and advancing tip Mach number, trimmed the rotor to zero first harmonic flapping, and then conducted a collective pitch sweep at each test condition. The recorded performance measurements were meant to validate the existing analysis of the time, and the authors concluded that predictions of drag were inadequate and needed improvement.

Charles and Tanner (1969) from Bell Helicopter carried out a joint Army/NASA/Bell

Helicopter investigation using the full-scale, two bladed, 34 ft diameter teetering rotor tested previously by McCloud et al. at the NASA Ames 40 ft by 80 ft wind tunnel [14]. The 34 ft rotor was tested up to $\mu = 1.1$. A 44 ft diameter rotor with low twist and a tapered tip was also tested, reaching a range of advance ratios from 0.31 - 0.52 and advancing tip Mach numbers from 0.51 - 0.94. The rotor geometry is provided, but again there is no mention of blade stiffness or mass. In testing at the higher advance ratios, the wind tunnel speed was set at its maximum and rotor RPM was varied to achieve the desired conditions. At each condition, the rotor was trimmed to zero first harmonic flapping with respect to the rotor shaft, and rotor hub loads, shaft torque, and rotor and control positioning data were recorded. The authors observed an increasing sensitivity to control inputs with advance ratio, and noted that at $\mu = 1.1$, the rotor became significantly less stable: at low collective, the rotor demonstrated a long transient response before achieving steady state; at the highest collective, the flapping response never stabilized and further testing was deemed unsafe. They noted that above $\mu = 0.5$, theory overpredicted rotor drag and correlations between predictions and the measured data began to break down. This investigation was intended to demonstrate the state-of-the-art of performance calculations of the time, and is further discussed in Section 1.2.2.

Fairchild Corporation's Ewans and Krauss (1973) designed, built, and tested a fully articulated, one-seventh scale rotor system in 1972 under contract from the Naval Air Systems Command [15]. Their reverse velocity rotor (RVR) concept, intended to validate predictions made in previous studies, utilized an elliptical airfoil shape to generate lift in reverse flow. The 8 ft, 4-bladed rotor model was tested in the

12 ft pressurized wind tunnel at NASA Ames, reaching advance ratios from 0.3 to 2.46 and tunnel speeds up to 350 knots, and obtained data at the highest advance ratio in publicly available literature. The rotor shaft angle was varied from $-5$ degrees forward to 12.5 degrees aft, and the rotor was trimmed to zero longitudinal flap and zero roll moment before data was collected for each setting. Two-per-rev swashplate control was used to provide higher harmonic inputs around the azimuth. The inertial and geometric properties of the blades were detailed in the report, though the stiffness distribution was omitted. The data collected included six-

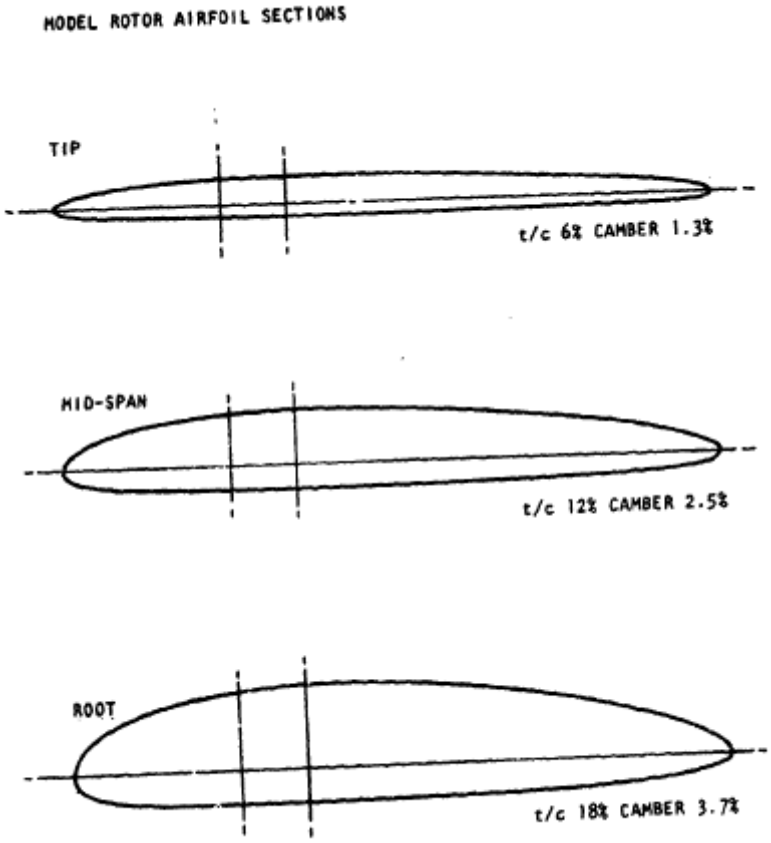


Figure 1.7: Ewans and Krauss studied the performance of a rotor with an elliptical airfoil up to $\mu = 2.46$.

component hub balance measurements, rotor flap and lag motion, control settings, blade bending moments, and lag damping moments.

Unlike previous tests prior to Ewans and Krauss, the rotor was successfully trimmed at each flight condition and experienced no dynamic instabilities throughout its operation. In addition, three different airfoil sections corresponding to the root, mid-span, and tip of the rotor (Fig. 1.7) underwent two-dimensional wind tunnel testing using pressure distributions and wake survey tests to characterize the airfoil sections in both forward and reverse flow. The data collected was used to predict the rotor performance at full-scale Reynolds numbers, and the authors observed that by using this data, a significant improvement in the predicted lift-to-drag ratio was obtained.

Norman et al. (2011) performed a full scale UH-60A rotor test at the NASA Ames 40 ft by 80 ft large scale wind tunnel [16] using the same UH-60A rotor used for previous flight tests, conducted by NASA and the Army and referred to as the UH-60A Airloads program [17]. The experiment was intended to both replicate the previous flight test data in a controlled setting as well as to collect additional data at high advance ratios. The authors hoped that a high-quality dataset could potentially be used to identify the sources of discrepancies in analytical models. The rotor was mounted on the Large Rotor Test Apparatus shown in Fig. 1.8 and incorporated two heavily instrumented blades: one blade was instrumented with 235 pressure transducers to measure rotor airloads, while the opposite blade was instrumented with multiple strain gauges and accelerometers to measure structural blade loads. The recorded data included rotor forces and moments, oscillatory hub

loads, blade deformations, control settings, and rotor wake measurements using Particle Imaging Velocimetry and deflection measurements using a retro-reflective background oriented schlieren scheme.

Figure 1.8: UH-60A rotor atop the Large Rotor Test Apparatus (LRTA) at Ames.

The last phase of the set of experiments was high advance ratio slowed rotor testing, which obtained data at advance ratios up to 1.0 and is well documented in a subsequent paper by Datta et al. [18]. This experiment was the first to test a production rotor at high $\mu$; it also provided a complete set of measurements, including performance, blade motions, structural loads, airload pressure distributions, and hub loads measurements. Parametric sweeps through advancing tip Mach number were conducted using three rotor RPMs (40%NR at M=0.26, 65%NR at M=0.42, and 100%NR at M=0.65, where NR refers to nominal rotor speed) and a maximum

tunnel speed of 182 knots. Longitudinal shaft tilt was varied from 0° to 4° aft, and collective pitch sweeps were performed at each flight condition. At each collective test point, the rotor was manually trimmed to zero first harmonic flapping before data was recorded.

For tracking purposes, the blade tip positions were located using a camera at 240° to track the rotor to within 0.5 blade tip thickness by making adjustments to the pitch links. The authors noted that thrust reversal was observed at high advance ratios between $\mu = 0.9$ to 1.0, and that rearward longitudinal shaft tilt improved the rotor lift-to-drag ratio as expected (Fig. 1.10). Reverse chord dynamic stall was clearly evidenced by the pressure measurements on the suction side of the blade in the reverse flow region, despite sensor failure in many of the spanwise stations in

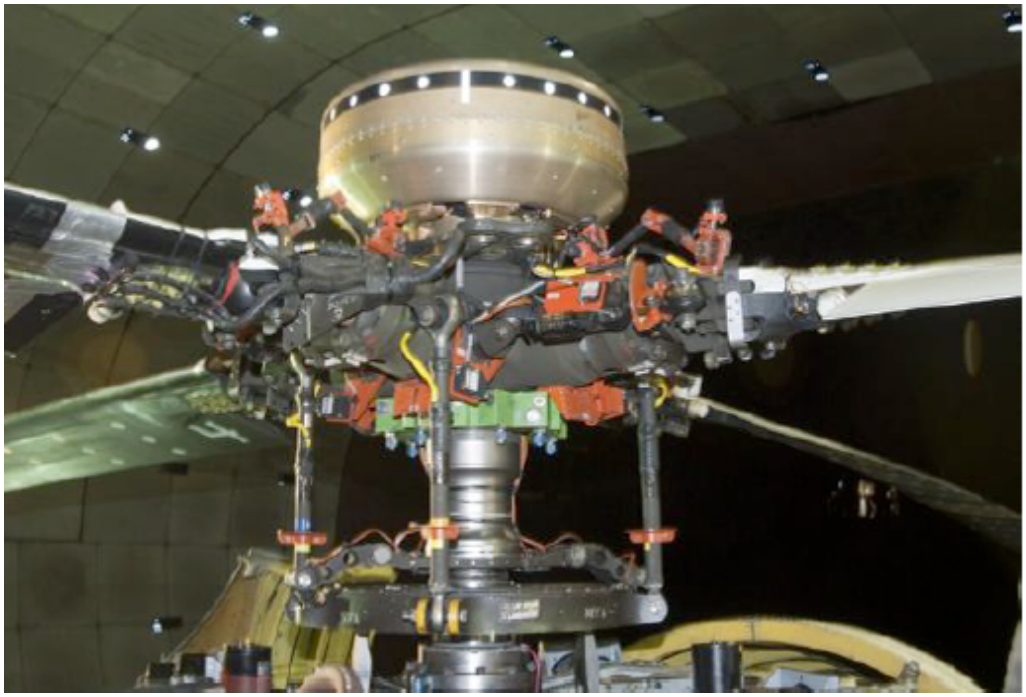

Figure 1.9: The articulated UH-60A hub outfitted with data acquisition components.

the reverse flow region. Dynamic loads at and above $\mu = 0.8$ on the slowed rotor were equal to or greater than the nominal rotor RPM at $\mu = 0.3 - 0.4$, which was thought to be a result of significant differences in airloads along the span of the rotor on the advancing side. The 4/rev vibratory loads were comparatively mild, reaching only half the amplitude of the 4/rev vibratory loads at the nominal rotor speed in spite of very high structural blade loads. This was attributed by the authors to a wide rotor frequency gap between the second flap and first torsion blade modes at 40%NR.

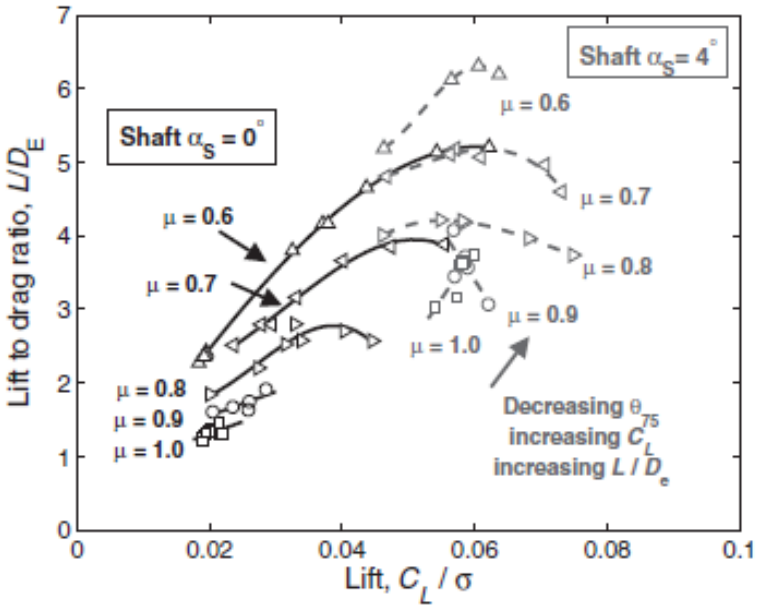


Figure 1.10: Rotor performance decreased with advance ratio, but this effect was lessened with 4° aft shaft tilt.

Berry and Chopra (2011-2015) conducted five slowed rotor tests on fully articulated, 4-bladed hub in the Glenn L. Martin Wind Tunnel (GLMWT) at the University of Maryland, achieving advance ratios up to $\mu = 1.61$ [19–24]. The first wind tunnel entry in 2009 investigated a 6 ft diameter rotor with constant-chord

SC1095 blades and $-12°$ twist up to an advance ratio of 0.66 [19]. In 2011, this test was expanded to an advance ratio of 1.2 [20]. The third experiment in 2012 tested a rotor that had untwisted NACA 0012 blades, each with a 2.78 ft radius and 3.15 in. chord, to $\mu = 1.0$ [21]. Results from these first three tests showed that thrust reversal occurred between advance ratios of 0.8 and 0.9 regardless of the blade camber, airfoil section, or twist, and that 4/rev vibratory loads demonstrated no correlation to mean thrust or advancing tip Mach number.

One year later, a fourth wind tunnel test incorporated 24 pressure sensors at 49% span into one blade and 6 strain gauges at various spanwise locations into the opposing blade. The other two blades were left non-instrumented. Strain gauges were bonded to two of the pitch links to obtain pitch link loads, and the wind tunnel test envelope was also expanded to test the rotor at advance ratios up to 1.4 [22]. The test stand in the GLMWT is shown in Fig. 1.11. However, because of dissimilarity between the instrumented and non-instrumented pair of blades, satisfactory trim at the higher advance ratios could not be achieved, and failure of more than half of the integrated pressure sensors prevented the airloads from being accurately determined. 4/rev hub loads were shown to increase with advance ratio, but it was unclear whether this was due to high rotor loads or an insufficiently trimmed rotor.

The fifth and final test in 2014 [23, 24] was operated between 40%NR to 20%NR, with most of the data taken at 30%NR. The maximum advance ratio achieved was 1.61 at $0°$ collective pitch and 20% nominal RPM. Large collective sweeps were performed at several advance ratios above 1.0, and lessons learned from the previous tests kept blade instrumentation from failing during testing. Measured

data included six-component hub loads, shaft torque, root flapping angles, pitch link loads, structural loads, and airloads at 30% span. Rotor blade geometry, inertial distribution, and stiffnesses were reported, and the author noted difficulties in tracking and trimming the rotor were experienced at the highest $\mu$. Performance and vibratory loads, rotor flap and and control angles, airloads, and structural loads were presented; the authors observed collective-thrust reversal at higher advance ra-

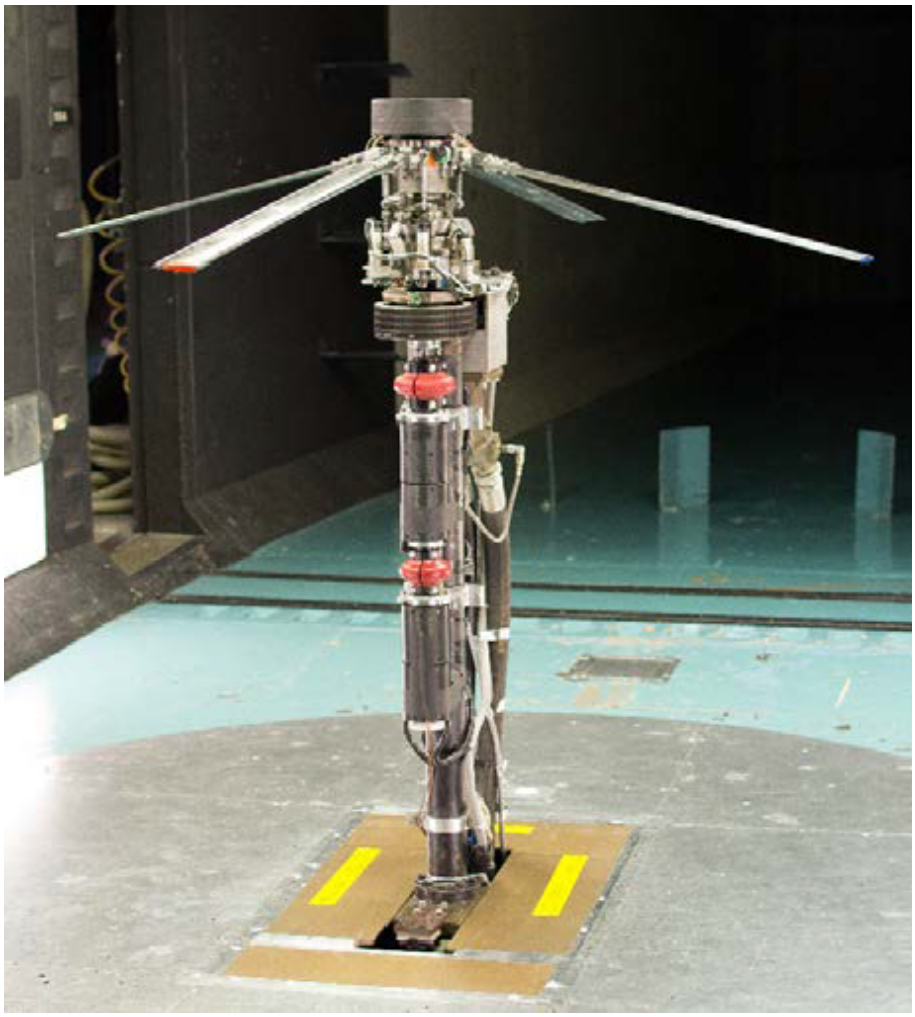

Figure 1.11: The 4-bladed, fully articulated rotor tested by Berry at the University of Maryland.

tios than previously observed in the literature, evidence of reverse chord dynamic stall in the blade torsion and pitch link loads, and an increase in performance and vibratory loads with increased advance ratio.

Wang, Saxena, and Chopra (2016) utilized the same 4-bladed, articulated test stand as Berry at al. for additional wind tunnel testing [25]. The rotor had a NACA 0012 airfoil with no twist or taper, and was operated at 900 RPM (40%NR) for most of the tests to avoid resonance between the slowed rotor and blade frequencies. Of the two pairs of blades, one pair was outfitted with embedded pressure sensors; for the second pair, only one blade was instrumented with strain gauges while the second blade was left non-instrumented. Difficulties in trimming and tracking the rotor at higher advance ratio were attributed to this dissimilarity in the blade set, and performing a test with uniform blades was recommended for future work. The tests performed collective sweeps from $-4$ to 12 degrees for most flight conditions and ranged between advance ratios of 0.3 to 0.8. An additional advance ratio sweep to $\mu = 1.15$ was conducted for fixed $4^\circ$ collective, though the results were not reported. Measured data included six-component hub loads (the yaw moment was not used), shaft torque, rotor RPM, blade root flapping angles, pitch link loads, airloads at 30% span, and structural blade loads. Reverse flow dynamic stall was evidenced by the pressure sensors on two of the blades. The declining sensitivity of rotor thrust to collective at increasing advance ratios was observed in the collective sweeps up to $\mu = 0.8$, with negative thrust at the single points above $\mu = 1.0$; this occurred even when dynamic stall pressure peaks were not evident and was therefore concluded to be unrelated to dynamic stall.

The data was analyzed using the University of Maryland's comprehensive rotorcraft code, UMARC, to correlate the experimental results with predictive models. The authors concluded that rotor thrust, drag, torque, and lift-to-drag ratio were all well-predicted, though the correlations tended to deteriorate at high advance ratios. The control angles were well matched, meaning this analysis could be utilized to achieve trim faster in future tests. The predicted vibratory loads captured the trends, though the experimental results were underpredicted at lower advance ratios and overpredicted at higher advance ratios. The authors attributed this to either modeling inaccuracies or blade dissimilarity. Overall, the comparisons showed that though the data trends were well captured, the analysis tended to under-predict the magnitudes at high advance ratios.

### 1.2.2 Numerical Studies

In 2008, Frank Harris [26] evaluated five state-of-the-art computational methods against three sets of isolated rotor experiments to demonstrate the improved capability – and persistent inability – to predict loads, control settings, and performance at high advance ratios. The five methods evaluated in this study included autogiro theory from 1934, CAMRAD II and RCAS comprehensive code with lifting line aerodynamics, the lifting surface aerodynamics in CHARM, and a CFD-CSD analysis incorporating OVERFLOW-2 with CAMRAD II. The full-scale isolated rotor tests used were from Wheatley's PCA-2 experiments [10], the H-34 tests conducted by McCloud, Biggers, and Straub [13], and the Charles and Tanner [14]

UH-1D rotor tests.

The predictions from the modern codes demonstrated much more accurate lift-to-drag ratios, between 7 and 9, which was in sharp contrast to previous predictions of up to 15 from 1934 autogiro rotor theory. All of the analyses modeled the decreasing sensitivity of thrust to collective, demonstrating collective-thrust reversal at advance ratios near 1.0. The CFD analysis could not accurately model reverse flow and the resultant effects on the rotor, and the comprehensive codes failed to predict the lateral cyclics required for trim. All of the codes failed to predict rotor H-force and shaft power, which the author attributes to inaccurately accounting for shank drag as well as a faulty understanding of reverse flow modeling. Harris concluded that although significant progress in predictive capability was evident from the comparison of modern to 1934 theory, none of the codes could accurately predict the H-34 controls or shaft angle required for a given lift condition for advance ratios higher than 0.62. Additionally, the experimental data above $\mu = 1.05$ was considered unreliable for use in correlations between theory and test, at least in part because of difficulties achieving a constant trim state.

Floros and Johnson [27] performed analysis of a slowed rotor compound aircraft up to $\mu = 1.45$ in 2009 using the experimental results obtained by Jenkins [12] to validate the methodology. With the exception of a notable offset between test data and analysis, good correlation with thrust was generally achieved; however, predictions degraded with shaft tilt (Fig. 1.12). Thrust reversal was modeled between advance ratios of 0.9 and 1.0, and shaft torque trends were well modeled, despite differences in the actual magnitudes and slopes. The authors conclude that

performance trends were well predicted by CAMRAD II analyses at high advance ratio using a rigid blade model.

Bowen-Davies and Chopra (2014-2015) used the University of Maryland's comprehensive rotorcraft code, UMARC, to correlate predictions with the slowed-rotor UH-60A experimental dataset [28] and later with experiments performed by Berry and Chopra [29] (see Section1.2.1) at the University of Maryland Glenn L. Martin Wind Tunnel.

For the UH-60A rotor analysis, rotor thrust and trim controls correlation degraded at advance ratios above $\mu = 0.7$, while drag predictions were shown to significantly improve by including a root shank drag correction and the effects of a faired fuselage, modeled with an upwash factor. Because lateral cyclic counters the effects of upwash on the front of the rotor in trim, the predicted thrust increased only slightly by including fuselage upwash. Lift-to-drag ratio was very well predicted for all advance ratios, and the inclusion of yawed flow corrections improved thrust correlations by delaying reverse flow dynamic stall. Oscillatory and vibratory loads predictions were well-captured for all advance ratios, and airloads correlations were significantly improved by adding a second trailing vortex at the blade root.

The modified UMARC code was also used to analyze the Mach-scale articulated rotor experiments carried out by Berry and Chopra in 2014, as reported in [23, 24]. Rotor thrust was well predicted up to an advance ratio of 0.825, but only predicts thrust reversal near $\mu = 0.9$ for collective angles with magnitudes of three degrees or less. When the retreating side blade pitch exceeds the stall angle, the lift in the reverse flow region dropped off and the thrust was dominated by the

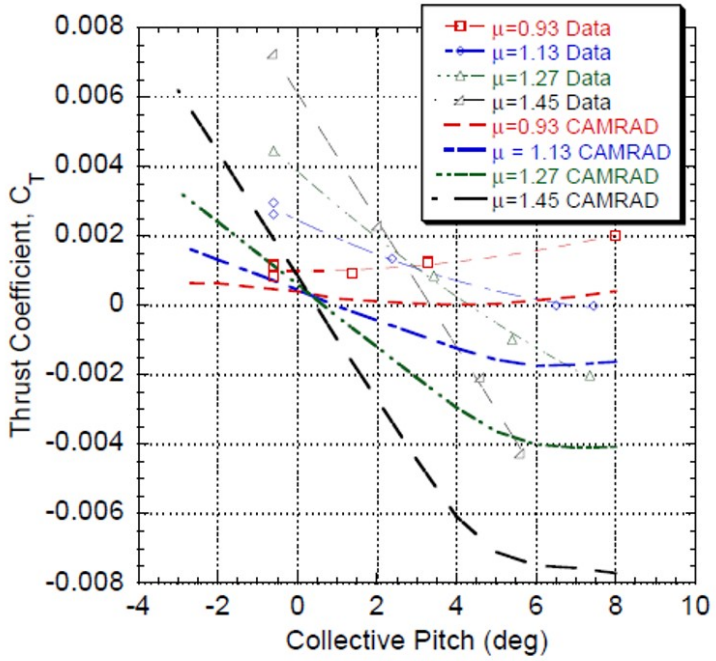


a)

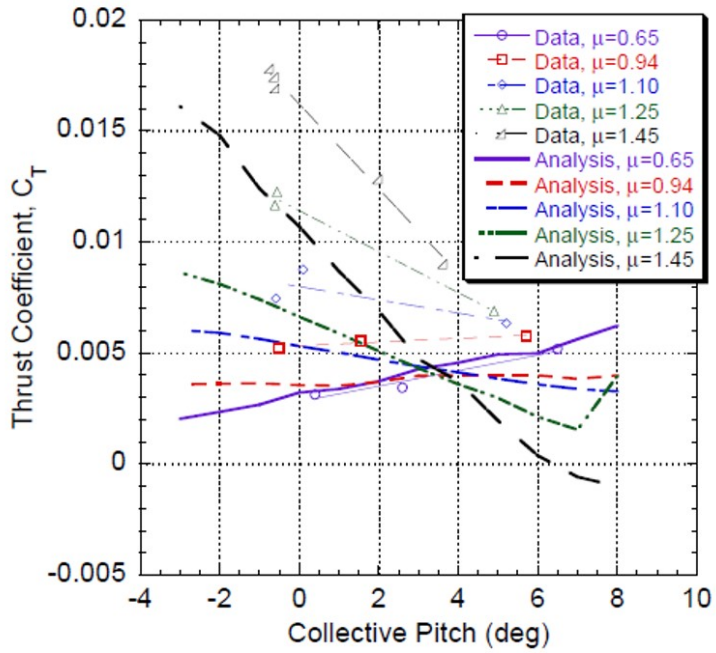


b)

Figure 1.12: Rotor thrust versus collective for high advance ratio at a) shaft angle of 0.5 degrees aft and b) shaft angle of 5.5 degrees aft.

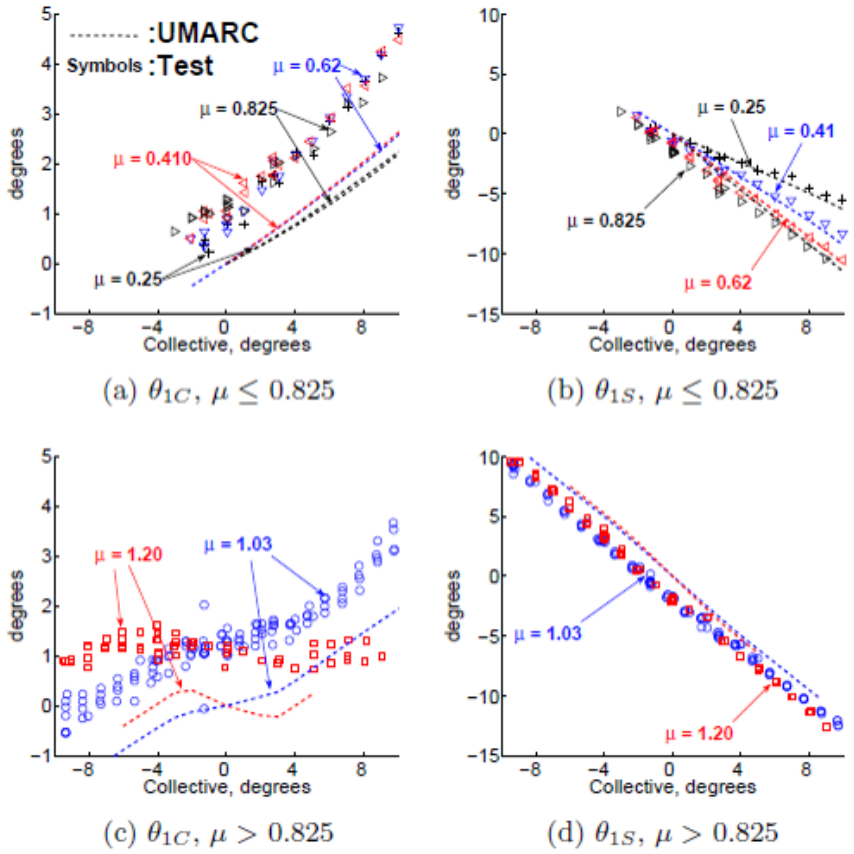


Figure 1.13: Validation of lateral ($\theta_{1C}$) and longitudinal ($\theta_{1S}$) cyclics, showing only a small 1° to 2° offset.

front and rear portions of the rotor disk. This causes the predicted thrust reversal to drop off, instead of continuing to decrease thrust levels with increased collective angle. Thrust reversal was shown to be sensitive to reverse flow stall angles, root cut-out, nose-down blade twist, and yawed flow corrections. Rotor trim cyclics were well-matched; both the lateral and longitudinal cyclics displayed a small offset of only one to two degrees and showed evidence of thrust reversal at small collectives (Fig. 1.13). Rotor H-force and shaft torque predictions deteriorated at high advance ratios due to the under-prediction of reverse flow drag after the retreating side blade

reached stall, but agreed well at low $\mu$. The measured drag force on the rotor at low advance ratios was smaller than the measured error, indicating uncertainty in the experimental data that does not reflect on the analysis. 4/rev vibratory hub loads increased significantly with advance ratio due to resonance between the second flap frequency and the 4/rev loads, and poor correlation of the in-plane vibratory loads suggests that the measurements may have been impacted by the resonance effects.

Potsdam, Datta, and Jayaraman (2016) performed coupled CFD-CSD analysis on the UH-60A experimental dataset previouly obtained in the large-scale wind tunnel at NASA Ames Research Center [18]. The analysis used coupled computational fluid dynamics (CFD) predictions from Helios and comprensive structural dynamics (CSD) modeling from RCAS, a comprehensive rotorcraft code. The objective of the analysis was two-fold: first, to validate the methodology using detailed experimental measurements, and second, to use the validated analysis to explore the physics of a slowed-rotor in high advance ratio regimes.

RPM sweeps from 100% to 40% nominal rotor speed (NR) and advance ratio ($\mu$) sweeps from 0.4 to 1.0 were performed with varied collective pitch angles. The authors concluded that throughout the range of tested advance ratios, differential loading was observed on the advancing side airloads, structural deformations, and trim settings. Correlated airloads, rotor control angles, and normal force matched well (Fig.1.14), but pitching moment predictions agreed poorly with experimental data, underpredicting negative pitching moment impulses on the advancing side and overpredicting positive impulses on the retreating side. The strength of reverse flow dynamic stall vortices captured by flow visualization techniques and pressure sensors

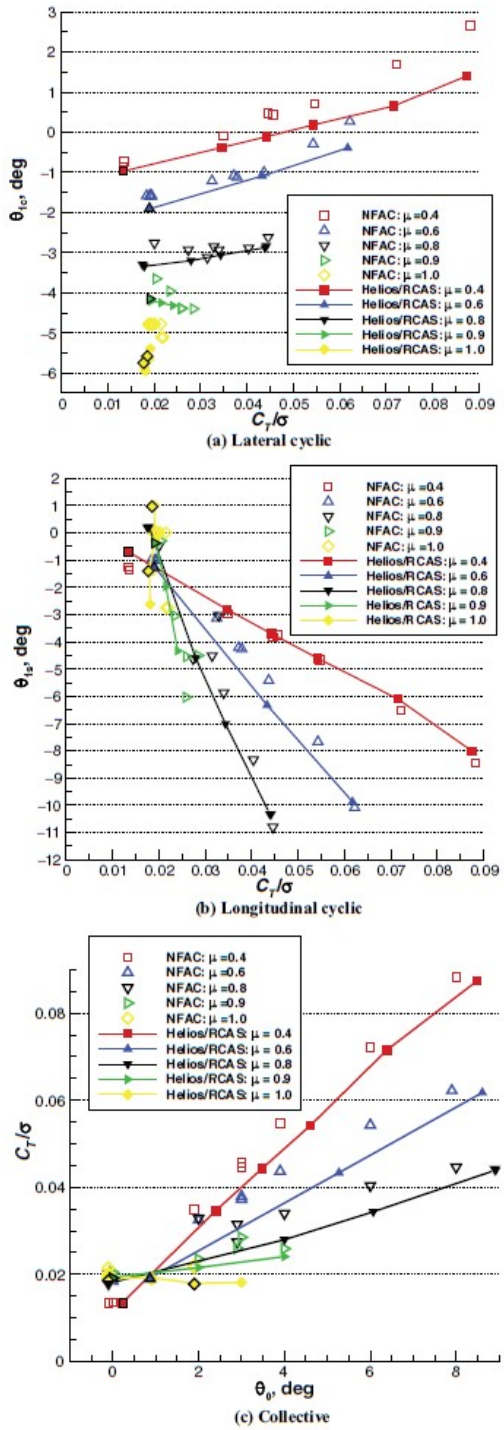


Figure 1.14: Potsdam et al. compare predictions (solid markers with lines) of rotor thrust and trim cyclics to test data (markers with no fill and no lines).

on the blade was underpredicted by CFD analysis, and wake visualization showed highly complex flow fields dominated by root and tip vortices, reverse flow effects, and blade-vortex interactions. Performance correlations were favorable, accurately capturing rotor drag and torque trends, and suggested improvements to shank drag was needed to further improve predictions.

### 1.2.3 Summary of Previous Work

Based on the available literature on the aeromechanics of slowed rotors at high advance ratios, there are some general conclusions that can be drawn:

1. Rotor performance has been previously measured in experiments involving high advance ratios, and despite errors in some aspects such as rotor tracking, predictive analyses are generally capable of modeling rotor performance sufficiently well. Rotor thrust and shaft torque are predicted sufficiently well for design purposes; however, rotor drag is not well predicted, and is often only correctly modeled after ad-hoc experimental correction factors are incorporated into the analysis. A common source of error is blade root (shank) drag, which dominates at high advance ratios and must be properly accounted for to avoid underestimating the drag prediction at high $\mu$. Despite errors in predicted drag, relatively good predictions in lift and shaft power result in a sufficiently good correlation of rotor lift-to-drag ratio.

2. Vibratory loads have been less widely measured in high advance ratio experiments, and have only been provided for two scale rotors [22, 24] and the UH-

60A full scale tests [18,30]. More vibratory loads measurements are needed to provide a comprehensive and reliable dataset for validating predictive models.

3. Rotor blade similarity is critical to improve rotor track and trim and to model rotor behavior accurately at high $\mu$. Very few prior research efforts on slowed rotors at high advance ratios, with the notable exceptions of the UH-60A Airloads program [17] and Berry et al. [31], have provided a complete set of rotor blade structural and inertial properties. Many authors [25, 31, 32] have attributed difficulties tracking and trimming the rotor at high $\mu$ to dissimilarities within the set of blades, which is primarily the result of incorporating instrumentation and sensors into the blade structure.

This work will help to address this gap by investigating the aeromechanics of a slowed rotor with highly similar blades up to an advance ratio of 0.9. Measured data includes rotor performance – thrust, drag, and shaft torque – in addition to vibratory hub loads, and the control settings and rotor flapping motion are also measured to provide a data set for validating predictive models.

## 1.3 Scope of Present Research

There are two main objectives of the present research: 1) experimental observations and data collection of a slowed rotor with highly similar blades at high advance ratios, and 2) validation of the comprehensive analysis tool, UMARC, using the experimental measurements to build upon the existing understanding of the aeromechanics of a slowed rotor in the high advance ratio flight regime. This

work investigated a 4-bladed, fully articulated Mach-scale rotor with uniform, non-instrumented blades, which was tested in a wind tunnel up to $\mu = 0.9$. The rotor was 5.6 ft in diameter, with a Lock number ($\gamma$) of 4.96 and a solidity ($\sigma$) of 0.12. The blades were untwisted and untapered, and utilize a NACA 0012 airfoil in order to provide a useful data set for the validation of analytical models. Special care was taken to build a set of highly similar blades possessing less than 5% variance in their structural and inertial characteristics.

The measured data included steady and vibratory hub forces and moments, shaft torque, blade root flap and pitch motion, and control settings (collective and cyclic angles). Collective sweeps were performed at each advance ratio, all of which were achieved by first setting the rotor RPM and subsequently adjusting the wind tunnel speed. At each new flight condition, the rotor was tracked and trimmed to zero first harmonic flapping.

Three rotor speeds (700 RPM, 900 RPM, and 1200 RPM) were tested, corresponding to 30%, 40%, and 50% of nominal rotor speed. While the vast majority of tests were performed with a simplified fuselage, limited tests were conducted without the fuselage to determine the effects at low and high advance ratio. Root collective pitch sweeps ranged from $-2$ to 12 degrees, and longitudinal shaft tilt from $-4$ to 4 degrees was applied at high $\mu$.

This data set will be used to further validate the UMARC comprehensive rotorcraft analysis code at the University of Maryland. The measurements were compared to results from UMARC analysis, revealing significant improvements in the correlation between measured and predicted rotor drag. Improvements in rotor

track and trim were also observed, demonstrating the value of blade similarity. The correlations between the experimental measurements and the UMARC predictions as well as the effect of increased blade similarity are the focus of this thesis.

## 1.4 Contributions of Present Research

The present research provided important refinements to scale-rotor wind tunnel testing and benchmark validation of comprehensive analysis using the same measured data. Key contributions include:

1. A uniform, non-instrumented blade set was constructed and structurally tested to ensure similarity between all four blades within 2.5% variance.

2. Higher blade similarity reduced difficulties in achieving rotor track and trim targets for advance ratios up to 0.7.

3. Direct sensing of blade root pitch provided better measurement accuracy than in prior work and therefore a higher quality data set.

4. To compliment prior work, which carried out tests at 700 RPM (30%NR), the majority of testing was completed at 900 RPM (40%NR) and 1200 RPM (50%NR) and achieved more realistic advancing tip Mach numbers up to 0.53.

5. An expanded shaft tilt envelope of $-4$ degrees to $+4$ degrees (positive aft) at $\mu = 0.5$, 0.7, and 0.8 demonstrated the benefits of positive longitudinal shaft tilt on lift-to-drag at high advance ratios.

6. A limited study on the effects of rotor-fuselage interactions at low ($\mu = 0.3$) and high ($\mu = 0.7$) advance ratios indicates that the fuselage has negligible effects on rotor performance, but does demonstrate a potential influence on lateral trim cyclic for this rotor-fuselage combination.

7. Validation of UMARC predictions using measured data shows good agreement of rotor performance, including improved drag correlations from prior work.

8. UMARC correlations in vibratory hub loads show similar trends, despite under-predictions in magnitude.

# Chapter 2: Fabrication and Testing of Composite Rotor Blades

## 2.1 Overview

Reducing rotor blade dissimilarity is essential to obtaining accurate and reliable baseline performance and vibratory loads data. Dissimilarities in the blades cause differences in blade motion and large 1P (one per rotor revolution) forcing, particularly at high advance ratios. While it is possible to build highly similar composite blades that track well, this has traditionally been achieved in industry by specialized, highly skilled personnel and at great expense [33].

The blades described in this work are of a legacy design that has been used by graduate students and research staff for many years at the University of Maryland [31, 34]. The rectangular rotor blade is 28 in. long with a 3.15 in. chord, and has no twist, taper, or sweep to maintain simplicity for validation of computational analyses. The 4-blade articulated rotor has a hinge offset of 6.4% and a root cutout of 16.4%, and the symmetric NACA 0012 blade design utilizes a well understood and widely-used airfoil to obtain baseline performance data and to provide useful datasets for computational validation. Inspired by the UH-60A rotor, the model rotor used in this research operates at a nominal rotational velocity of 2300 RPM in hover with an advancing blade tip Mach number of 0.60. The rotor properties are

summarized in Table 2.1.

The incorporation of sensors into the blade structure inherently affects the internal characteristics of the blade, and has been shown to introduce up to 5% variance in the structural and inertial properties of the University of Maryland rotor blades [25]. To ensure a highly similar blade set for this work, a number of non-instrumented rotor blades were constructed and put through extensive structural testing to quantify the inertial, dynamic, and geometric properties. The four blades used in testing were selected to minimize discrepancies in the demonstrated structural and dynamic characteristics.

Table 2.1: UMD Mach-scale rotor properties

| Parameter | Value |
|---|---|
| No. of blades | 4 |
| Blade profile | NACA 0012 |
| Blade radius, in. (m) | 33.4 (0.843) |
| Blade chord, in. (m) | 3.15 (0.080) |
| Rotor solidity | 0.120 |
| Nominal RPM | 2300 |
| Lock no. | 4.96 |
| Tip Mach no. | 0.60 |
| Tip Reynolds no. | $1.1 \times 10^6$ |
| Hinge offset | 6.4% |
| Root cutout | 16.4% |

Figure 2.1 outlines the model blades used in this research, which consist of a dense foam core for structural support, a flat composite spar for bending and torsional stiffness, ±45 degree carbon fiber skin to maintain a smooth airfoil profile and provide torsional stiffness, and leading edge weights for proper CG (center of gravity) placement.

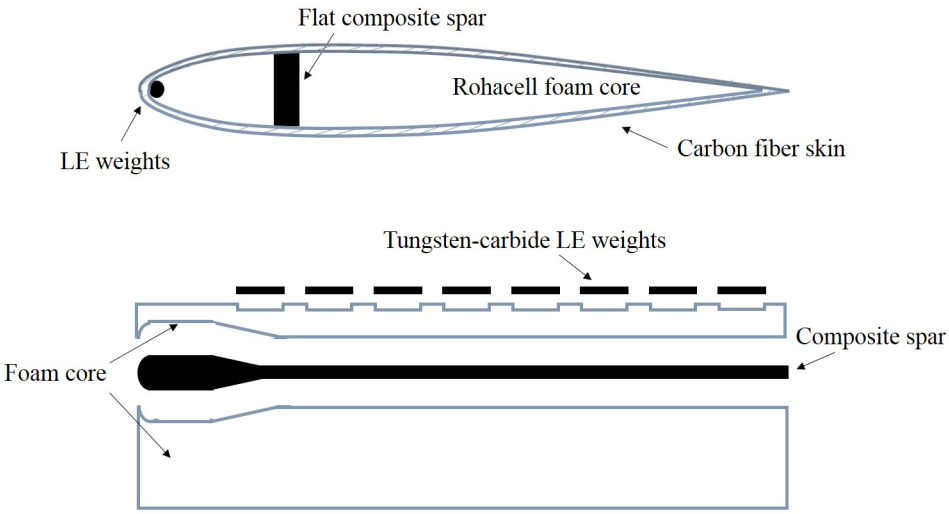


Figure 2.1: Structural components of the UMD model rotor blade.

## 2.2 Equipment and Materials

The blades used in this research were fabricated in-house at the University of Maryland Rotorcraft Center. As shown in Fig. 2.2, the blades were constructed using Rohacell 31 foam, IM8 unidirectional graphite-epoxy fiber, 3K-70-CSW ±45 degree graphite-epoxy composite plies, Cytec FM 300 adhesive film, 6061 aluminum, and tungsten-carbide weights. The blade components were milled out and oven-cured in a two-piece aluminum mold, then sanded and finished by hand.

## 2.3 Construction Procedures

A set of procedures developed over many years of testing at the University of Maryland Rotorcraft Center has been refined and improved to ensure repeatability in blade construction. This is significantly more difficult to achieve with instrumented blades, as the introduction of sensors into the structure can affect the stiffness and

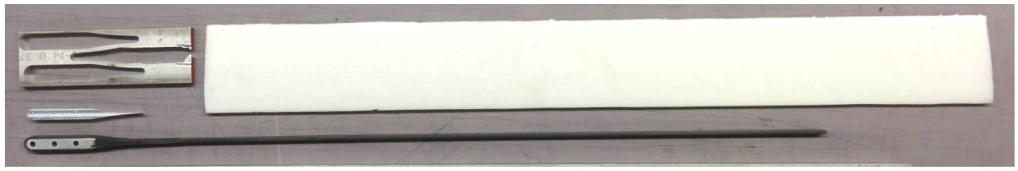

a) Inner blade components: CNC-milled aluminum root insert, cured composite spar made from unidirectional graphite-epoxy, and Rohacell 31 foam core

b) Opened aluminum blade mold

c) Oven with blade mold

Figure 2.2: Materials used in the fabrication of the UMD model rotor blade.

inertial distribution of the blades. Therefore, the blades used in this work were not outfitted with pressure sensors or strain gauges in an effort to preserve uniformity during blade construction. In each step of the blade manufacturing process, multiples of each component were formed, weighed, and checked for uniformity before moving on to the next step in the construction procedures. This allowed imperfections or abnormalities to be identified at the source of the dissimilarity, and the problematic subcomponent was fixed or replaced before advancing to the next step in the fabrication process. Thus, each set of subcomponents was determined to be sufficiently similar at every phase of construction.

### 2.3.1 Composite Spar

The composite spar consists of cured unidirectional carbon fiber wrapped around an aluminum root insert, which transfers the blade loads to the hub and serves as the connection point for the blade grip. A CNC (computer numerical control) mill was used to drill the three holes forming the blade grip attachment with maximum precision. The root insert, which possesses a shape resembling an elongated teardrop, was milled out of a 0.32 in. thick block of 6061 aluminum. Next, the root insert was wrapped in a layer of film adhesive in preparation for bonding to the rest of the spar.

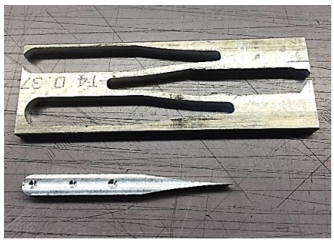

a) CNC-milled aluminum blade root insert

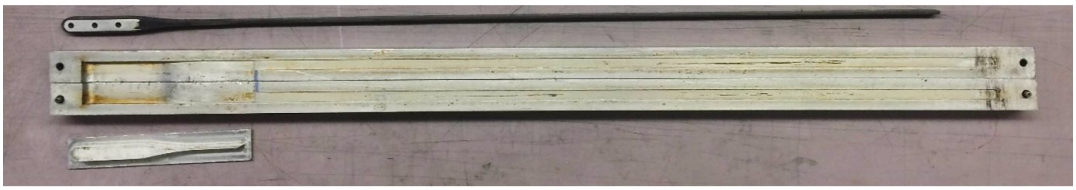

b) Cured composite spar next to aluminum mold

Figure 2.3: Unidirectional carbon fiber strips wrap around an aluminum root insert to form the spar.

To form the composite spar, eight 0.32 in. by 58 in. strips of the graphite-epoxy unidirectional prepreg were laid into a 0.32 in. aluminum mold (Fig. 2.2(b))

and wrapped around the aluminum root insert (Fig. 2.3(a)). The excess strip lengths were trimmed to allow the mold to close, then the mold was fully clamped and placed into the oven to cure at 350°F (177°C) for 150 minutes, in accordance with the curing cycle of the adhesive. After curing, the spar was sanded and trimmed to size (28 in. long by 0.32 in. wide) and a square 1.5 in. strip of unidirectional graphite-epoxy was wrapped perpendicularly around the spar at the tapered edge of the root insert before repeating the cure cycle once again. This last step provided additional strength and prevented delamination at the tip of the root insert. The cured spar is shown in Figure 2.3 along with the blade root insert.

### 2.3.2 Foam Core

Next, the 0.375 in. thick foam core sheet was cut to the size of the aluminum blade mold (28 in. long by 3.15 in. wide), placed within the mold and tightened in a star-pattern sequence to ensure even compression, and heated in the oven at 350°F for 90 minutes. This process allowed the heated foam to expand to fill the mold, forming the desired aerodynamic profile and maintaining the geometric shape of the airfoil after cooling. The cooled foam was removed from the mold and trimmed to a 3 in. chord length, then a 1/8 in. end mill was used to cut the foam at 1/4 of the finished blade chord (0.787 in. from the leading edge). This cut allows the spar to fit seamlessly between the two foam pieces, which form the leading and trailing edges of the blade, with no gaps.

Once the two foam pieces and the spar fit together satisfactorily, the foam

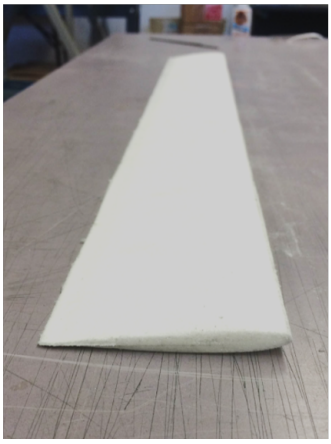

a) Foam core compressed into NACA 0012 profile

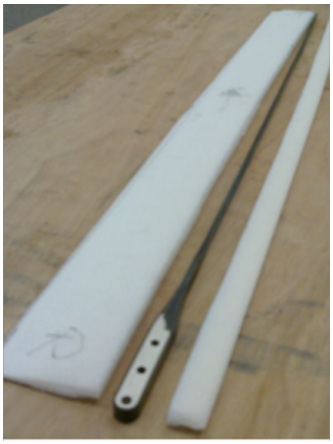

b) Foam cut into LE and TE pieces

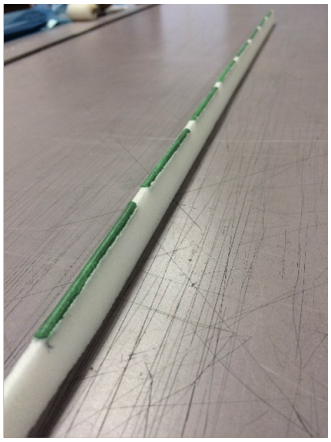

c) Weights installed along leading edge

Figure 2.4: The foam core is molded into shape and cut at quarter chord, then discrete tungsten-carbide weights are wrapped in film adhesive and installed along the leading edge.

piece forming the leading edge was precisely milled using the CNC machine and a ball end mill to cut eight slots in the leading edge of the foram. Within each slot, eight tungsten-carbide 9/64 in. diameter rods, each 2.5 in. long and wrapped in a layer of film adhesive, were placed into the foam core such that the rods were flush with the leading edge. The weights were evenly distributed along the entirety of the blade span to move the center of gravity of the blade forward of the quarter chord. Then the two foam pieces and the spar were wrapped in the film adhesive and pressed together to form the inner structure of the blade.

### 2.3.3 Graphite-Epoxy Carbon Fiber Skin

Finally, an oversized section of $\pm 45$ graphite-epoxy carbon fiber was cut and laid over an equally-sized piece of release film, as shown in Fig. 2.5. The leading edge of the inner structure of the blade was centered within the carbon fiber skin, and the

a) Bare blade components sanded to fit together

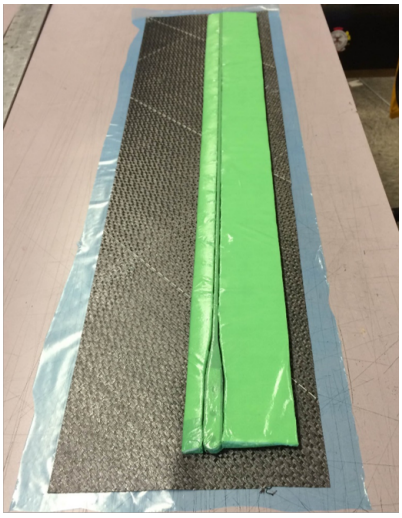

b) Adhesive-wrapped components

Figure 2.5: The inner structure is wrapped in a film adhesive and overlaid with a carbon fiber sheet. Blue release film is used to protect the carbon fiber from debris and ensure easy removal from the mold after cure.

skin was folded over and smoothed to eliminate any wrinkles or air bubbles. The excess carbon fiber and release film was trimmed to fit snugly within the aluminum mold, which was tightened and placed into the oven to cure at 350°F for a final 150 minutes. The finished blade was removed and trimmed to exactly a 28 in radius and a 3.15 in. chord, and the three holes for the blade grip were re-drilled, using

Table 2.2: Blade component weights

| Component Mass (g) | % Total | Blade 1 | Blade 2 | Blade 3 | Blade 4 |
|---|---|---|---|---|---|
| Root insert | – | 14.6 | 14.5 | 14.6 | 14.7 |
| Complete spar | 21% | 43.2 | 42.0 | 41.7 | 40.9 |
| Foam core | 11% | 22.2 | 22.4 | 22.3 | 22.4 |
| LE weights | 39% | 76.1 | 76.1 | 76.1 | 76.1 |
| Film adhesive | 13% | 24.3 | 25.3 | 25.7 | 26.4 |
| Carbon fiber skin | 16% | 31.6 | 31.7 | 31.6 | 31.5 |
| Final blade | 100% | 197.4 | 197.5 | 197.4 | 197.3 |

the holes in the root insert as guides. Any imperfections in the outer surface of the blade were filled with epoxy and sanded to a smooth finish. The weights of each component as well as the final blade weights are listed in Table 2.2.

## 2.4 Structural Testing

Structural testing of the blades is vital to understanding the structural and inertial characteristics of the blades and accurately modeling the behavior of the rotor, particularly at high advance ratios. The structural properties of these blades are described in detail in the following subsections and a summary is provided in Table 2.3. More blades were manufactured to achieve a set of four blades with a high degree of similarity, and finally the four blades with the most similar structural and inertial characteristics were used for wind tunnel testing.

Table 2.3: Measured blade structural properties

| Parameter | | Blade 1 | Blade 2 | Blade 3 | Blade 4 | % Variance |
|---|---|---|---|---|---|---|
| Mass, kg | $m$ | 0.1974 | 0.1975 | 0.1974 | 0.1973 | 0.05 |
| Natural frequency, Hz | $f_n$ | 13.5 | 13.4 | 13.0 | 13.0 | 2.08 |
| Flap inertia, kg-m$^2$ | $I_b$ | 0.0578 | 0.0592 | 0.0587 | 0.0592 | 0.84 |
| EI$_{flap}$, Nm$^2$ | $EI$ | 29.3 | 30.8 | 30.8 | 29.4 | 2.53 |
| GJ, Nm$^2$/rad | $GJ$ | 23.3 | 23.7 | 23.5 | 23.8 | 0.95 |

### 2.4.1 Mass and Inertia Matching

Great care was taken during blade construction to ensure the masses of inner components were consistent. The final blade set demonstrated a 0.05% variance

in mass with an average of 0.1974 kg per blade, emphasizing the consistency and uniformity of the blade manufacturing process. The flapwise inertia about the flap hinge was measured for each rotor blade, which is an important parameter in the blade flap equation for a rotor in flight and can be calculated from Eq. (2.1) using the total mass $m$, the center of mass location $x$, and the period of oscillation $T$.

$$T = 2\pi\sqrt{\frac{I}{mgx}} \tag{2.1}$$

The center of mass of the blade and blade grip was calculated using calipers and a digital scale, and a pendulum-type experiment was conducted to measure the blade inertia. Each blade was hung vertically from a bar and allowed to swing freely, and the resulting oscillations were measured using a Hall effect sensor and recorded in LabVIEW. Because the flap and lag hinges on the rotor hub are coincident, the flap inertia is approximately equal to the lead-lag inertia. This allows the blade to swing in the lead-lag direction, reducing the aerodynamic damping that would be incurred by swinging in the flapwise direction. Fig. 2.6 shows the experimental setup: the blade and model blade grip were hung from a smooth rod resting between two rigid metal supports, and a bearing in the blade grip reduced the effects of friction during oscillation.

The 3D-printed blade grip was used as a placeholder for the hub's aluminum flap hinge for structural testing of the blade, though the lengths and masses of the metal components of the blade grip were used to calculate the total inertia of the blade assembly. To record the angular position of the swinging blade, a small

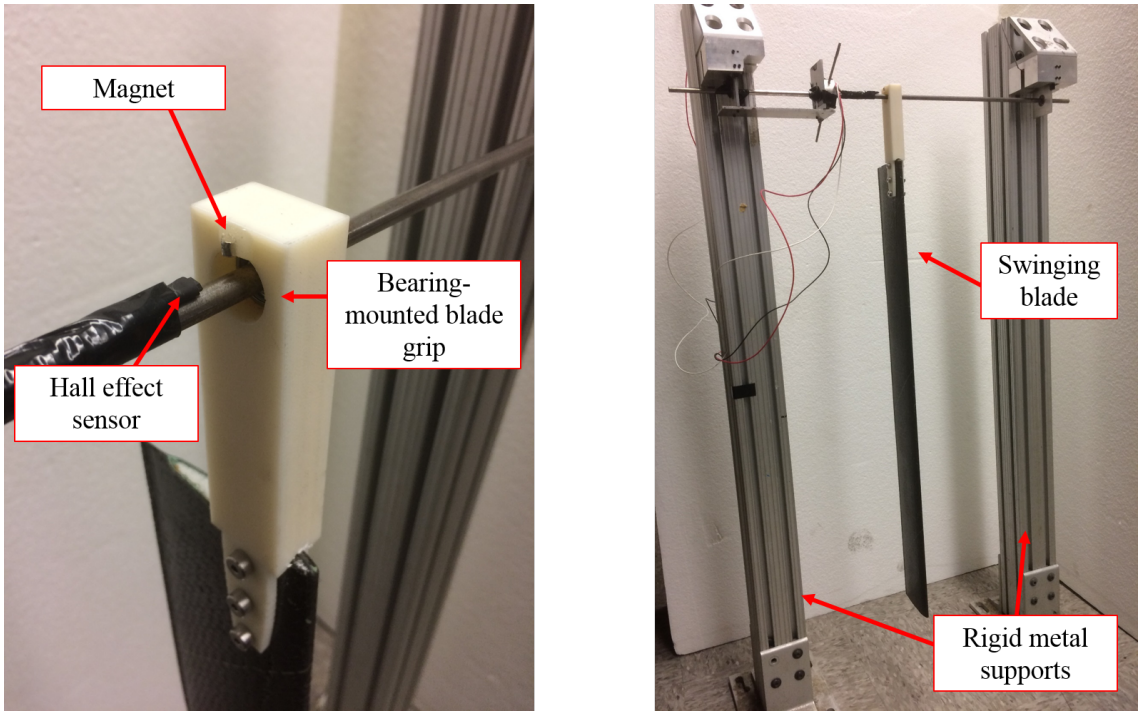


Figure 2.6: The blade hinge swings from a frictionless bearing while a Hall effect sensor records the angular displacement caused by the oscillations.

magnet was epoxied to the blade grip within range of a Hall effect sensor mounted to the rod. The voltage peaks represent the point in time when the blade is perfectly vertical; thus, a full oscillation occurs between every other peak. For the first trial shown in Fig. 2.7, each oscillation is indicated by the black circular markers.

### 2.4.2 Frequency Response

The rotating flapping frequency of the rotor system, $\nu_\beta$, is a key index of its dynamic characteristics. Most articulated rotor hubs have flap frequencies between 1.0/rev (no hinge offset) and 1.05/rev. The UH-60A rotor has a first flap frequency

of 1.035/rev [34], while the model rotor used in this research was determined to have a first flap frequency of 1.047/rev.

The vibratory characteristics of the nonrotating blades were determined for both forced and unforced conditions. The cantilevered blades were hung vertically while an electro-mechanical shaker with a magnetic tip in combination with a 25 mm short-range laser were used to precisely measure the blade oscillations. A small magnet was placed on the blade in line with the magnet-tipped shaker to allow for non-contact forcing. The phase offset of the magnetic forcing was considered to be negligible after comparing results to the unforced response. A rap test was performed to determine the unforced natural frequency of each blade, then the electric shaker was used to run through a frequency sweep to determine additional modal frequencies. The experimental setup is illustrated in Fig. 2.8, and a sample of the data collected is shown in Fig. 2.9. The final four blades demonstrated a

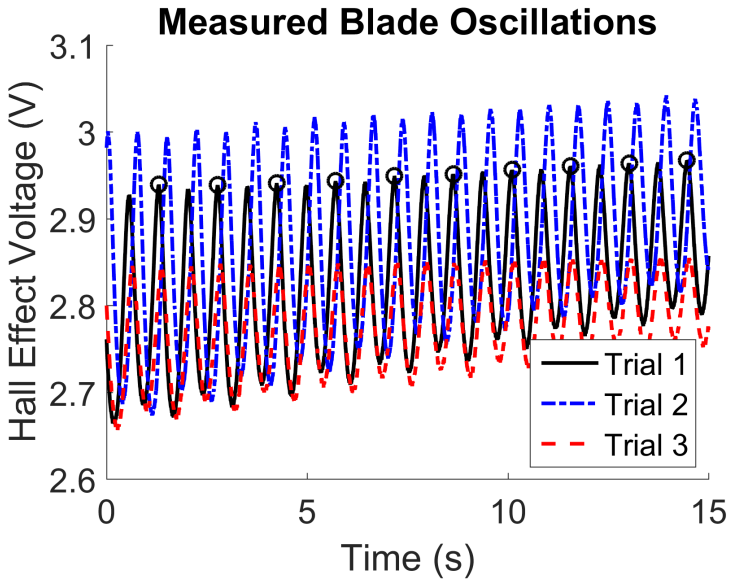


Figure 2.7: Multiple trials provided an average period of oscillation for each blade.

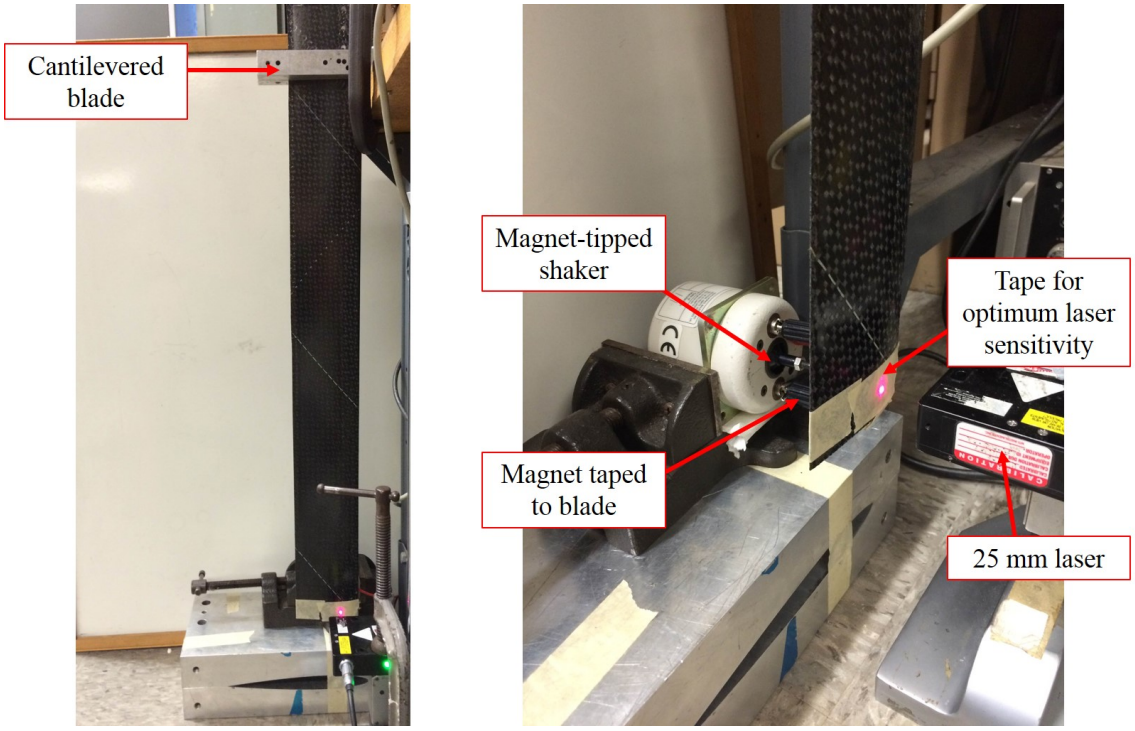


Figure 2.8: Experimental setup for forced frequency response tests.

2.08% variance in natural frequency, as shown in Table 2.3.

### 2.4.3 Bending and Torsional Stiffness Tests

The composite spar is the main structural element of the rotor blade, carrying the centrifugal forces and providing the bending and torsional stiffness of the blade. First, the spar must be capable of withstanding the high centrifugal loads achieved during normal operation. Tensile testing of the spar during the initial blade design demonstrated the ability of the spar to withstand centrifugal loads well above those encountered during hover and wind tunnel testing [34]. Second, the spar provides the bending and torsional stiffnesses of the blade, which must be quantified and compared to those of the other rotor blades to be used in testing.

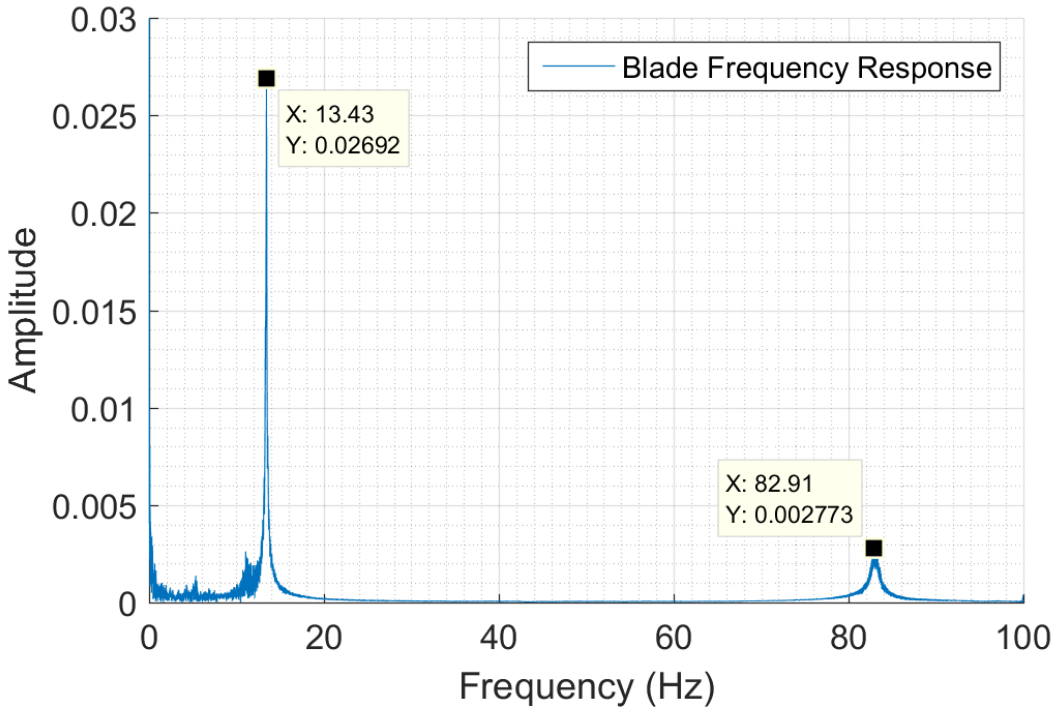


Figure 2.9: Sample of the natural frequency data collected for each blade.

Each rotor blade underwent testing to determine its bending and torsional stiffness and was analyzed as shown in Eqs. (2.2), (2.3), and 2.4. The high aspect ratio rotor blade is modeled as a one dimensional Euler-Bernoulli beam with its elastic axis along the quarter-chord. The blade was considered to have uniform stiffness and uniform distributed blade mass per unit span, and the flap-wise bending stiffness was measured via a gravity loading technique as shown in Fig. 2.10.

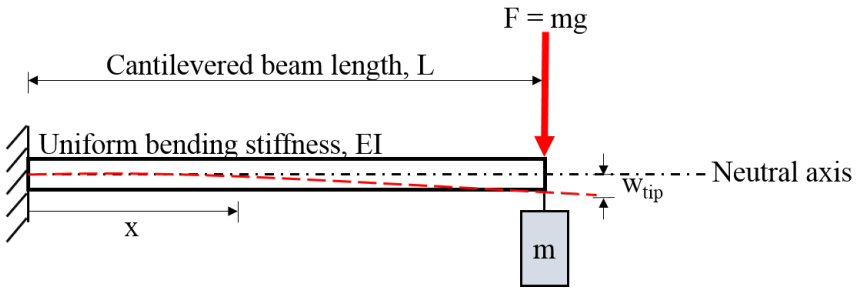


Figure 2.10: A blade modeled as an Euler-Bernoulli beam in bending.

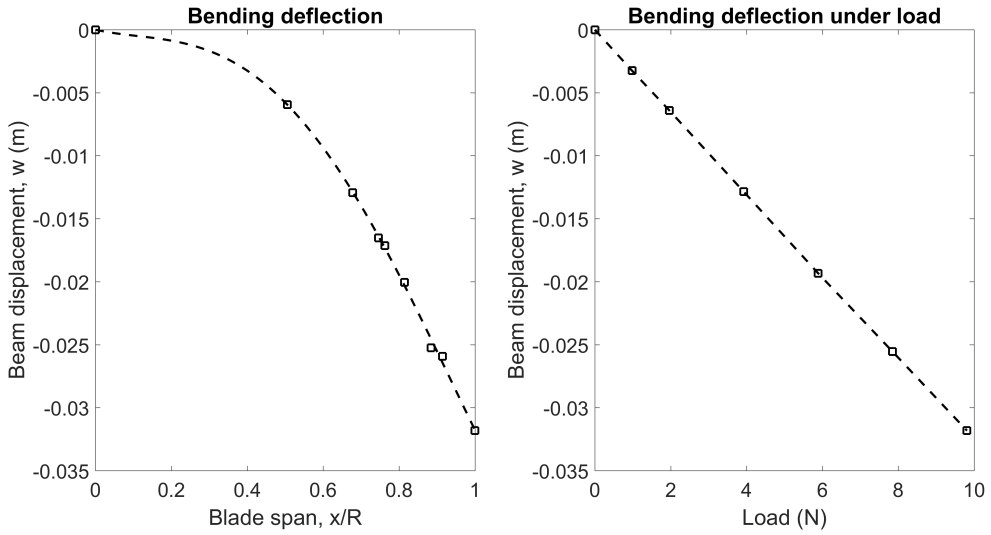


Figure 2.11: Beam deflection across the blade span and under varying loads.

$$\frac{d^2w}{dx^2} = \frac{M}{EI} \tag{2.2}$$

$$\frac{dw}{dx} = \int_0^L \frac{-mg(L-x)}{EI} dx \tag{2.3}$$

$$EI = \frac{mgL}{2(dw/dx)} \tag{2.4}$$

By measuring the blade deflection for a given loading across multiple span-wise locations, the outboard bending slope was measured and the flapwise bending

stiffness was calculated. This is shown in Fig. 2.11, which also shows the beam displacement was measured for a range of loads. After a second integration of the Euler-Bernoulli equation, these displacements were used to calculate the stiffness for each loading. An average of these points was taken and showed the two methods were similar; however, each integration introduces some error, and therefore the first method was used to determine the stiffness of each of the blades. The flapwise bending stiffness of the final four blades selected for testing differed by 2.5%, half the variance of previous tests.

The same technique was used to measure the blade torsion stiffness, GJ, according to the analysis shown in Eqs. (2.5), (2.6), and (2.7). The same gravity loading technique, as shown in Fig. 2.12 and 2.13, was also used.

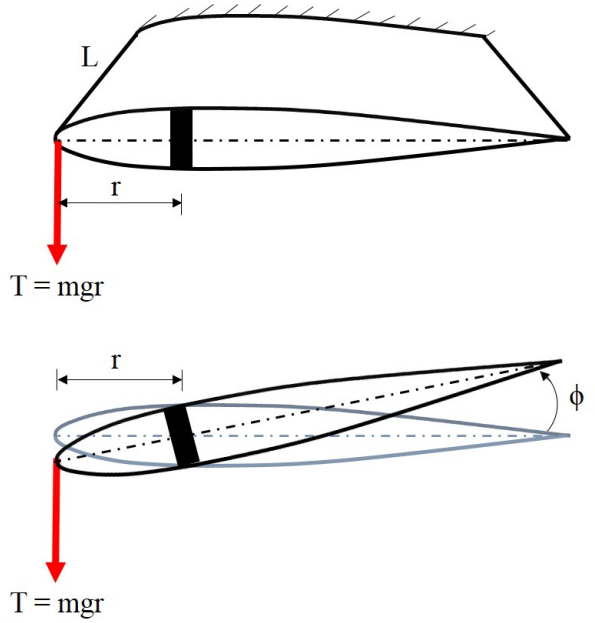


Figure 2.12: A blade modeled as an Euler-Bernoulli beam in torsion.

$$\frac{d\phi}{dx} = \frac{T}{GJ} \tag{2.5}$$

$$\phi = \int_0^L \frac{T}{GJ} dx \tag{2.6}$$

$$GJ = \frac{mgrL}{\phi} \tag{2.7}$$

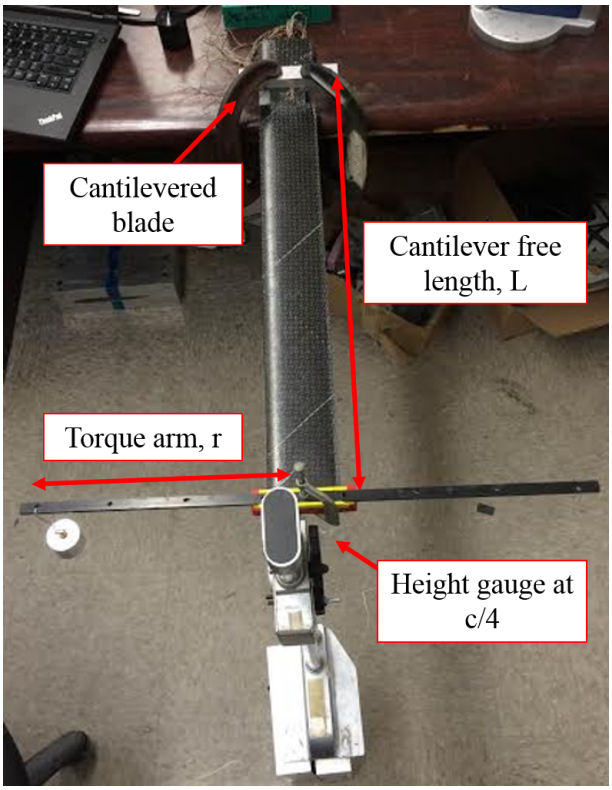


Figure 2.13: Experimental setup for torsion and stiffness tests.

The torsion angle was measured for both leading edge and trailing edge loads (Fig. 2.14) and the resulting stiffnesses were averaged to obtain the final value used for comparison. The final set of blades selected for wind tunnel testing demonstrated a 1% variance in torsional stiffness.

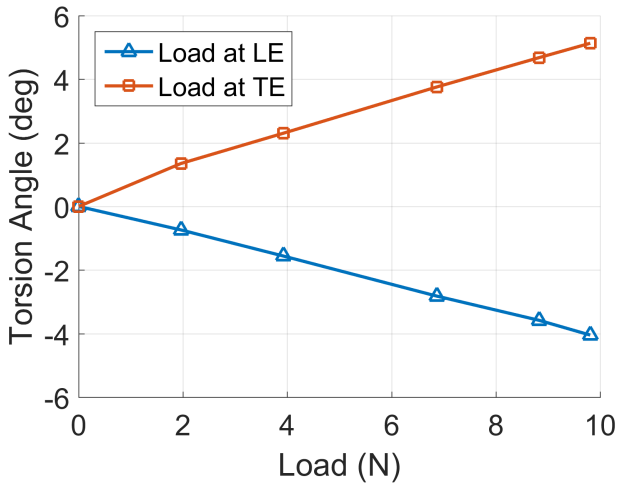


Figure 2.14: Blade torsion angle at various weights.

### 2.4.4 Blade Balancing

The blades should be balanced such that the center of rotation of the rotor is also at the center of the hub.If the center of rotation about the hub is misaligned, the resulting imbalance can cause a variation in the centrifugal loading azimuthal history and a large 1/rev in-plane vibratory forcing. To avoid this and to reduce vibration, the blades should be both statically and dynamically balanced. Before dynamically balancing ("tracking") the spinning rotor on the test rig, the blades must be checked for static spanwise and chordwise balance. The chordwise center of gravity (CG) of the blades must be at or ahead of the aerodynamic center, which is located at the quarter-chord of the blade, to avoid aeroelastic pitching instabilities during wind tunnel testing. This is particularly important for the blades used in this research, since the flat spar utilized in this blade design reduces torsional stiffness.

Figure 2.15 illustrates this process; each blade was balanced on a smooth metal bar to find the chordwise CG location, and the balance point was measured with calipers to ±0.001 in. precision. The blades were then balanced on a needle-edged

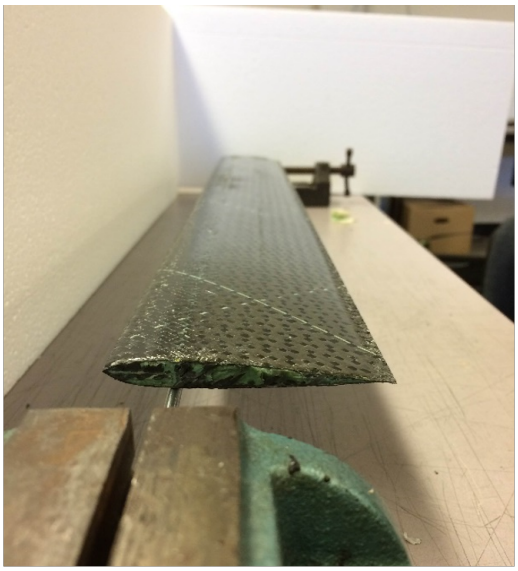

a) Chordwise blade balancing

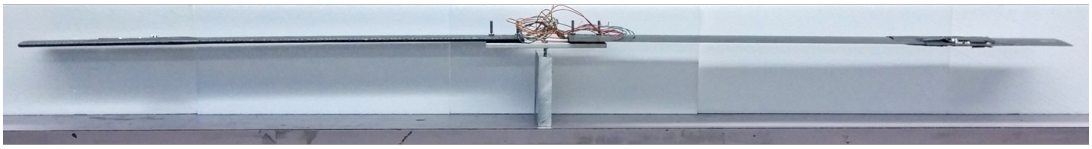

b) Spanwise balancing of the blades on a needle-edged point

Figure 2.15: Chordwise and spanwise balancing of the blade.

point to check the spanwise weight distribution and resulting moment balance of each pair of blades. Using small strips of aluminum tape, weight was added to the tip of the blade until balance was achieved. The balanced blade pairs were noted and subsequently installed on the rotor hub for hover and wind tunnel testing.

# Chapter 3: Experimental Test Setup

## 3.1 Testing Methodology

The research described in this work utilized the facilities and equipment housed within the Alfred Gessow Rotorcraft Center (AGRC) laboratories, including an articulated rotor test stand, hover tower, and data acquisition system as well as the University's Glenn L. Martin Wind Tunnel (GLMWT). These are further described in the following sections. This research expanded the envelope of previous tests, investigating the effects of a fuselage, larger shaft tilt and collective angles, and higher rotor RPM.

## 3.2 Rotor Test Stand

The AGRC rotor test stand is a mobile test bed for the University of Maryland's scale rotor models that can be mounted atop the AGRC hover tower or installed in the GLMWT for investigations involving forward flight.

The rotor stand is compatible with multiple hub types, and for this research a fully articulated, four-bladed rotor hub was installed on the rotor stand (Fig. 3.2). The articulated hub consists of overlapping flap and lead-lag hinges, and

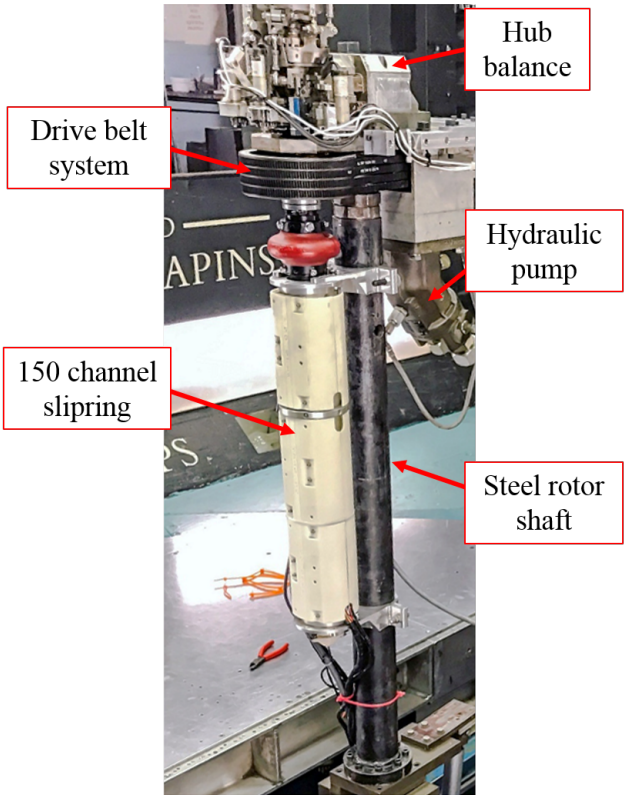


Figure 3.1: The AGRC test stand is operated by a 75 hp electric motor that drives a hydraulic pump to power the rotor's belt-driven pulley system.

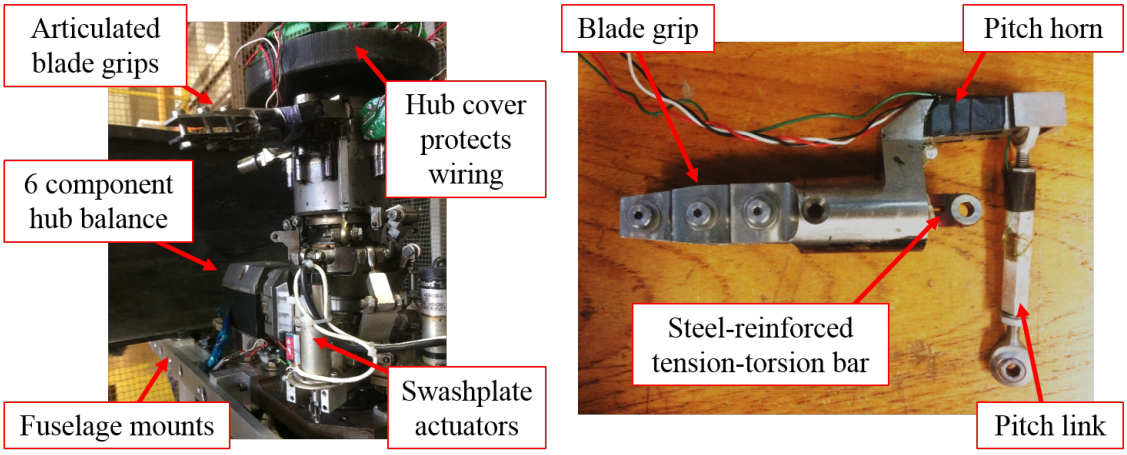


Figure 3.2: Fully articulated rotor hub (left) and blade grip assembly (right).

a steel-strengthened elastomeric tension-torsion bar in each blade grip assembly allows for blade feathering. A steel platform supports a floating six-component hub balance and has mounts to accommodate a custom-built 3-D printed nylon fuselage. Three linear variable displacement transducers (LVDTs) measure the swashplate displacement to calculate the control angles, recording the collective, lateral cyclic, and longitudinal cyclic angles of the rotor.

Mounted on the rotor shaft, a 150 channel slipring transfers rotating frame signals from hub and blade sensors into the fixed frame. The rotor is powered by a 56 kW (75 hp) electric-driven hydraulic pump capable of operating the drive belt system at a maximum of 2500 RPM.

### 3.2.1 Hub Force and Moment Measurements

A six-component balance mounted to the hub measures static and dynamic forces and moments in all three axes, while an additional torque cell affixed to the rotor shaft measures the required shaft torque. The torque cell was calibrated and was determined to have an estimated measurement uncertainty of 1.5% [34].

Shaft encoders record the rotor RPM at 1/rev and 60/rev and were used in conjunction with a rotary Hall effect sensor to track the rotor azimuth. A 150 channel slipring custom-built by Fabricast and connected via a flex coupling to the rotor shaft converts the rotating frame signals into the fixed frame.

A three-axis ±16 g accelerometer captures the fixed frame vibratory motion of the rotor test stand, and a static calibration performed of the balance [31,34] was

used to determine the estimated error and uncertainty in the hub loads measurements, as shown in Table 3.1.

Table 3.1: Hub balance error estimates

| | Axial $F_X$ (lb) | Side $F_Y$ (lb) | Normal $F_Z$ (lb) | Roll $M_X$ (in-lb) | Pitch $M_Y$ (in-lb) | Yaw $M_Z$ (in-lb) |
|---|---|---|---|---|---|---|
| Cal Range | 100 | 100 | 120 | 650 | 650 | - |
| Max Error | 0.39 | 0.41 | 0.73 | 4.08 | 4.16 | - |
| Min Error | -1.89 | -0.91 | -0.67 | -5.84 | -11.09 | - |
| 95% Confidence | 0.47 | 0.30 | 0.51 | 3.04 | 2.99 | - |

### 3.2.2 Blade Pitch and Flap Measurements

As shown in Fig. 3.3, the rotor hub is instrumented such that the root pitch and flap angles of each blade is known. Strain gauges bonded to two of the four pitch links provide pitch link loads for opposing rotor pairs, and Hall effect sensors on each blade grip directly measure the individual blade pitch and flap angles in the rotating frame. The pitch and flap sensor calibrations were performed using a digital inclinometer ($\pm 0.5^\circ$) to correlate the sensor output voltage to the full range of blade positions.

In addition to the direct pitch measurement at the blade root, three fixed frame LVDT sensors monitor the three swashplate actuators that control rotor collective, lateral cyclic, and longitudinal cyclic and provide additional blade pitch information. Due to some play in the hub components, the direct blade measurements from the Hall effect sensors were found to give better correlation during testing (Fig. 3.4), shown by the variation of shaft torque for increasing collective in hover.

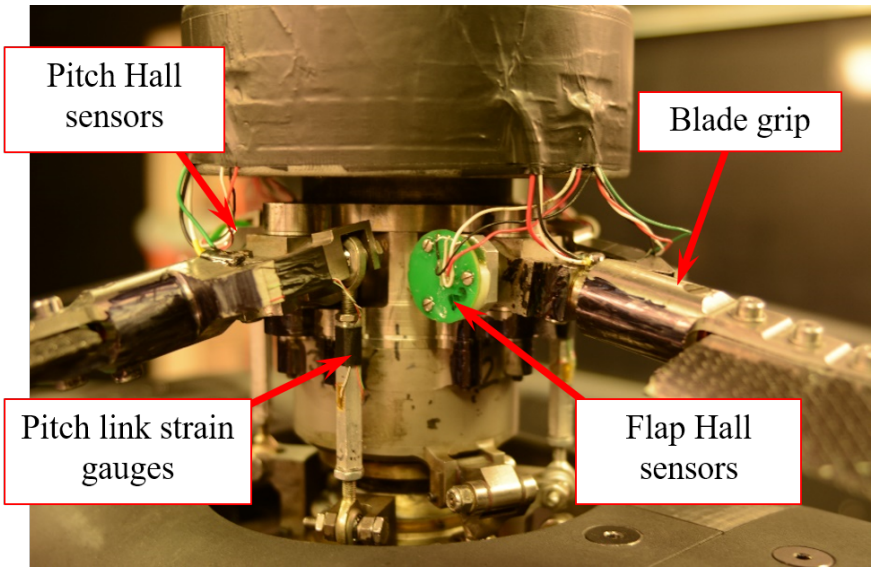


Figure 3.3: The fully articulated hub was instrumented to measure pitch link loads and the pitch and flap motion of each blade.

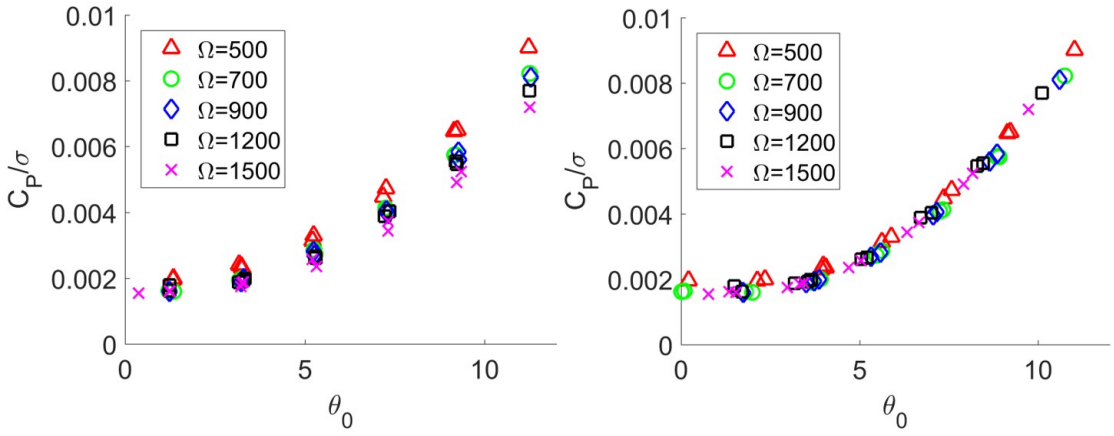


Figure 3.4: Direct pitch measurement from the rotating frame provides higher quality data correlation.

## 3.3 Hover Tower Tests

The University of Maryland hover tower, shown in Fig. 3.5, is a prominent fixture within the AGRC that is primarily used to investigate the aeromechanics of a rotor in hover. It is also useful for testing the reliability of hub and blade sensors, rotor stand instrumentation, and the data acquisition system in the highly loaded environment of a spinning rotor before adding the additional complexity of forward flight testing in the wind tunnel.


Figure 3.5: The AGRC hover tower at the University of Maryland.

The hover tower stands 6 ft tall such that when the rotor test stand is mounted atop the tower, the plane of the rotor disk is 12 ft from the ground. The 2.78 ft radius rotor is slightly more than two rotor diameters from both the ground and the

ceiling, respectively enabling out-of-ground-effect in hover and unrestricted inflow.

The rotor was tested on the hover tower to ensure all equipment, sensors, and instruments were performing reliably and to collect performance data for a range of rotor RPMs (500, 700, 900, 1200, and 1500 RPM) and collective angles ($-2$ to $12°$). During its conception, the legacy blade design had been previously strength-tested to ensure survival at the nominal rotor RPM in hover. To reduce the likelihood of failure with this blade set, the current blade set underwent an additional proof test: the rotor blades were spun up to 1800 RPM on the hover tower, 1.5 times the maximum rotor RPM to be reached during wind tunnel testing, to ensure safe operation.

## 3.4 Wind Tunnel Tests

The GLMWT is a low speed closed-circuit wind tunnel on the University of Maryland campus, which has been in operation since 1949. After hover tower testing, the rotor stand was transferred to the wind tunnel for forward flight testing.

### 3.4.1 Wind Tunnel Description

The test section of the GLMWT is 7.75 ft tall and 11.04 ft wide with rounded corners, for a total cross sectional area of 85.04 square feet. It is capable of a maximum airspeed of 230 mph (or equivalently, a Mach number of 0.3) and has a measured turbulence intensity of 0.21% [35]. The rotor test rig used in this research was mounted directly to the floor of the test section, resulting in a calculated wind

tunnel blockage of 2.3%. A shaft angle correction for helicopters, originally adapted for rotors by Langer, Peterson, and Maier [36] and re-derived by Schmaus [37] was calculated to account for the effects of the wind tunnel walls and is given by Eqn 3.1.

$$\Delta\alpha_s = \frac{2\delta_w C_T A_{rotor}}{\mu^2 A_{tunnel}} \tag{3.1}$$

In this equation, $\Delta\alpha_s$ depends on $\delta_w$, which corresponds to the boundary layer effects of the tunnel test section area ($A_{tunnel}$), the flight conditions $\mu$ and $C_T$, and the area of the rotor disk ($A_{rotor}$). For the GLMWT test section, $\delta_w = 0.12$ [38], and the ratio of rotor area to test section area is equal to 0.29. The wind tunnel force balance under the test section floor was locked into place for the duration of rotor testing, and a load cell on the rotor stand measured all fixed frame forces and moments on the hub. The dimensions are shown in Fig. 3.6.

### 3.4.2 Installation Procedure

A complete set of installation procedures were developed for the UMD rotor stand by Saxena [34]. The rotor stand is lifted into the wind tunnel and bolted to the wind tunnel balance beneath the floor of the wind tunnel test section. The rotor stand bolts into a shaft tilt mechanism under the floor such that the bottom of the stand is flush with the test section floor; this is shown in Fig. 3.7 and Fig. 3.8.

The hydraulic lines, power cables, and sensor wires are funneled through the test section floor, as shown in Fig. 3.8. The electrical connections pass beneath the wind tunnel and into the floor of the control room, where the data acquisition

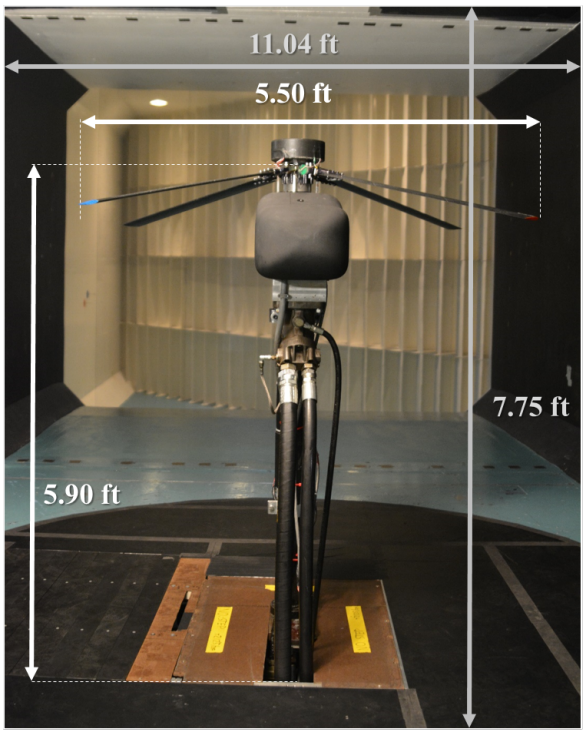


Figure 3.6: Dimensions of rotor rig in GLMWT test section.

system is set up. Once the rotor stand is fully installed, the blades can be bolted onto the hub and the rotor stand sensors must be statically calibrated. Finally, the electric motor and hydraulic pump must be inspected for safety and checked for adequate airflow and hydraulic fluid levels before testing can begin.

### 3.4.3 Data Acquisition

All results were recorded at a 5 kHz sampling rate using a National Instruments 15-bit ADC (model USB-6255) data acquisition system (DAQ) and LabVIEW virtual instrument panel interface as shown in Fig. 3.9 and 3.10. Voltage signals from the test stand instrumentation were passed through the DAQ and processed using SCXI-1102C modules, and all signals were recorded for 5 seconds at each

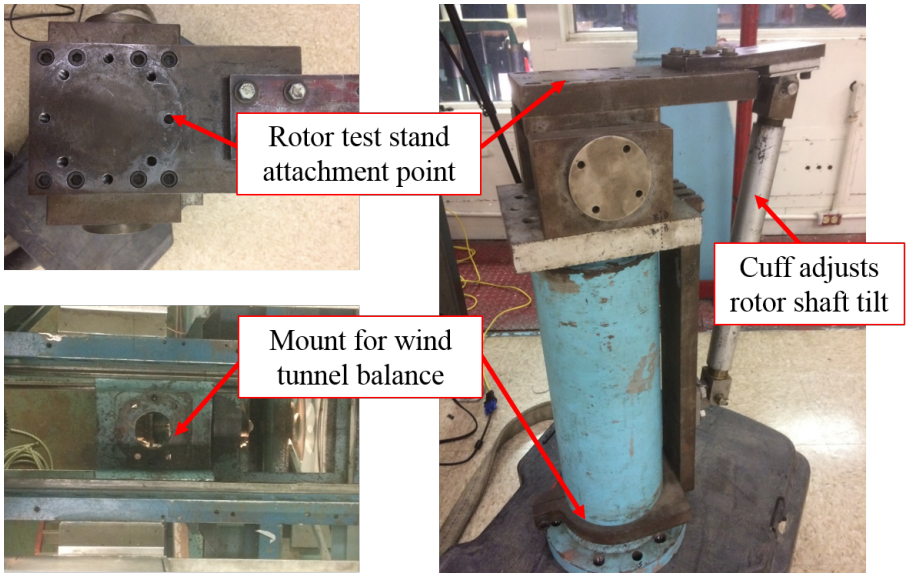


Figure 3.7: The rotor shaft is mounted to a shaft tilt mechanism that bolts onto the GLMWT balance.

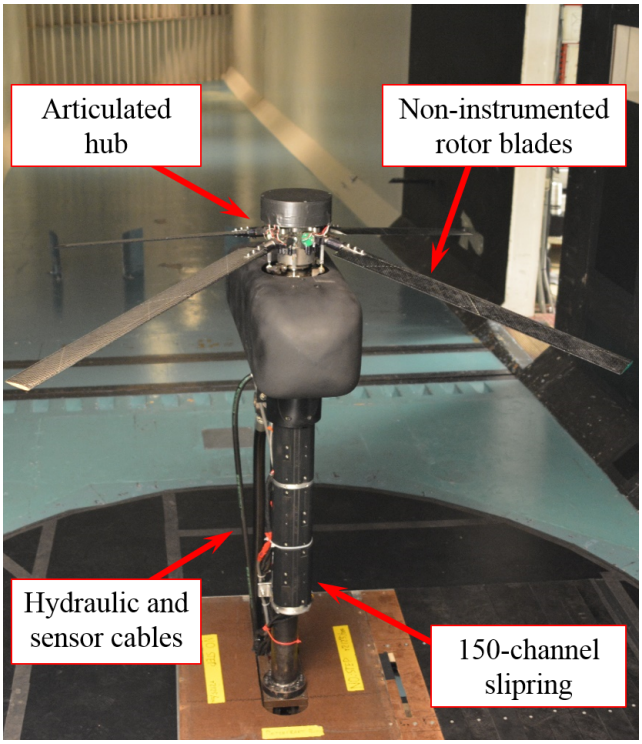


Figure 3.8: A front view of the test stand fully installed in the GLMWT.

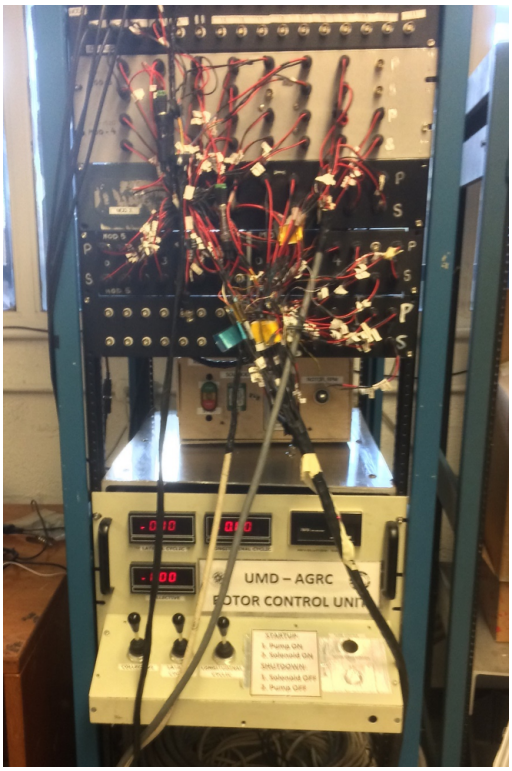


Figure 3.9: Data acquisition tower with breakout BNC connectors.

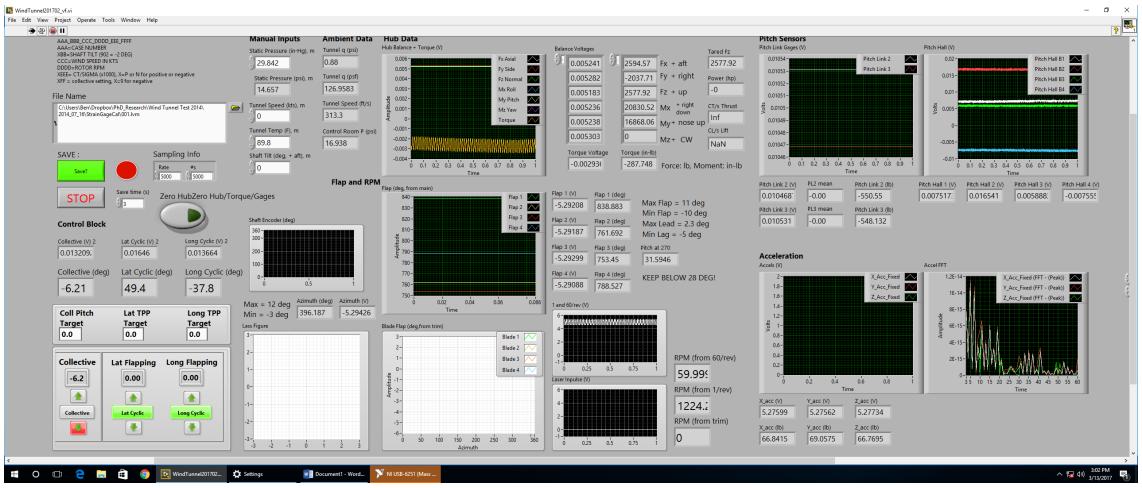


Figure 3.10: LabVIEW virtual instrument panel readout.

flight condition in LabVIEW. The LabVIEW interface showed swashplate controls angles, flap and pitch angles for each blade, wind tunnel velocity, hub loads, rotor RPM, an FFT of accelerometer loads, and rotor lateral and longitudinal cyclics with negligible time delay. This allowed sensor health and rotor and blade flap angles to be monitored closely in real time while also enabling quantitative feedback vital to trimming the rotor at each flight condition.

### 3.4.4 Tare Cases

For each flight condition in forward flight, the recorded signals had to be tared to isolate the hub loads and moments from the rotor. This was done by subtracting out the loads and moments of the test stand at the same flight conditions but without the rotor blades, as shown in Fig. 3.11. Blade shanks were used to properly account for the drag caused by the entire blade grip assembly.

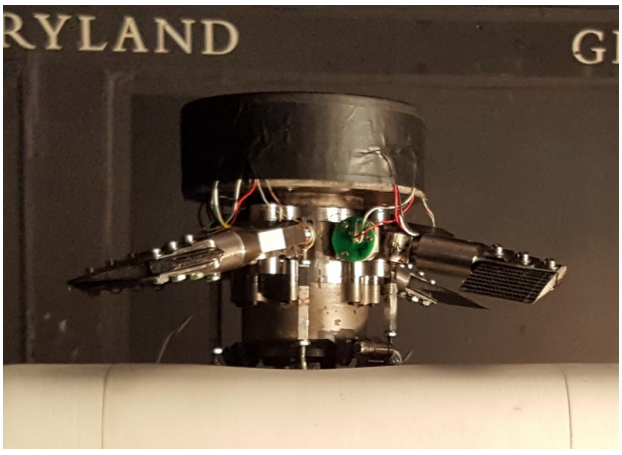


Figure 3.11: Tare cases were run for each flight condition using shank blades to accurately capture hub drag.

### 3.4.5 Rotor Track and Trim

Though the rotor blades were statically tested to ensure inertial similarity and spanwise balance, the aerodynamic characteristics must also be matched. Tracking a rotor is a method of aerodynamically matching the blades by balancing the hinge moments caused by aerodynamic, inertial, and centrifugal forces to align the tips of each blade into the same tip path plane (TPP). Rotor tracking was achieved in this research by manipulating the pitch link rods to alter the root pitch of each blade individually. This affects the flapping response of the rotor and aligns the tip path plane by addressing any aerodynamic dissimilarities in the set of blades.


Figure 3.12: Blade tracking was recorded using strobe lights set to the blade passage frequency to highlight reflective tape on each blade tip.

To examine the rotor tip path plane, differently-colored reflective tape was fixed onto the tip of each rotor blade. The rotor was operated at the desired flight condition, then strobe lights set to the blade passage frequency were shone into the wind tunnel test section at approximately 225° and 315° rotor azimuth. Maximum

flapping response for articulated rotors lags maximum forcing on the advancing side by approximately 90°, and therefore 225° azimuth is an optimal azimuth for TPP tracking. By comparison, tracking at 315° was more easily accomplished. The light was reflected by the tape, highlighting the position of the rotating blade tips (Fig. 3.12). The four blade tips were vertically separated by some distance due to differences in flapping response, and the pitch link rods were adjusted between runs to alter the blade flap response until tracking was achieved. The rotor was considered to be tracked when all four blade tips were vertically aligned within one-half blade-tip-thickness; however, due to limits in the pitch link adjustments, tracking could not always be achieved and tended to worsen at high advance ratios.

At every test point and flight condition, the rotor was first trimmed to zero flap angle such that the normal force was perpendicular to the shaft and the magnitude of the first harmonic of the blade flap angle was approximately equal to zero. This state, known as wind tunnel trim, cancels out the lateral and longitudinal flap response of the rotor and leaves only the steady coning component of flap motion. This was accomplished by manipulating the cyclic control settings until the first harmonic of the averaged blade flapping amplitude was approximately zero. As advance ratio increased and differences in the blades were exaggerated, the rotor became less responsive to control inputs and became more difficult to trim.

### 3.4.6 Test Plan

The maximum achievable speed in the wind tunnel test section was 200 knots; therefore, tests to advance ratios of 0.9 were performed by slowing the rotor RPM 40% (900 RPM) to 50% (1200 RPM) of nominal. Most tests were conducted at a 0° shaft angle, with a few cases ($\mu$ = 0.5, 0.7, 0.8 at 900 RPM and $\mu$ = 0.5, 0.6, 0.7 at 1200 RPM) tested at shaft tilt angles of 4° fore and aft.

A 3-D printed fuselage was designed and mounted on the rotor stand for the majority of the tests described in this work, with the intention of providing a structural base for investigating aspects of compound configurations in future experiments. A limited number of tests were conducted without the fuselage to provide a basis for comparison with this setup, while previous results from similar tests performed in 2016 [25] were also used for comparison. The test envelope is given in Table 3.2.

Table 3.2: Wind tunnel test envelope

| Parameter | 700 RPM | 900 RPM | 1200 RPM |
|---|---|---|---|
| Collective, $\theta_0$ (deg) | -2 to 12 | -2 to 12 | -2 to 10 |
| Shaft tilt, $\alpha_s$ (deg) | 0 | -4, 0, 4 | -4, 0, 4 |
| Advance ratio, $\mu$ | 0.3 | 0.3, 0.5-0.9 | 0.3, 0.5-0.7 |
| Fuselage included | Yes | Yes and No | Yes and No |

# Chapter 4: Results and Validation of High Advance Ratio Testing

This chapter will detail the results of the experimental data and the correlations with the predictions from UMARC analysis. This test involved parameter sweeps of collective pitch angle, advance ratio, and shaft tilt for rotor speeds of 900 RPM and 1200 RPM. The rotor RPM was set, the wind tunnel was brought up to the desired speed, and the rotor was tracked and trimmed at 4° collective pitch before performing a collective sweep from $-2$ to 12 degrees for each flight condition. A discussion of each result is provided in the following sections.

## 4.1 UMARC Modeling

The University of Maryland Advanced Rotorcraft Code, UMARC, is a comprehensive analysis that is used to model the aeromechanics of this rotor in high advance ratio environments. The correlations to the experimental results of this investigation are intended to provide a baseline analytical comparison for a rotor with 'clean' (non-instrumented), highly similar blades.

UMARC is based on finite element discretization in both space and time, and uses a lifting-line approach with NACA 0012 airfoil table look-ups. The model used in this research incorporates 12 temporal elements and 20 spatial elements in

its calculations; to simplify the solution process, each finite element in space uses modal reduction with 15 degrees of freedom. Derived from Hamilton's principles, the analysis includes coupled elastic flap, lag, twist, and axial deformations to second order precision [39]. UMARC also utilizes the Weissinger-L trailed wake model for predicting nearwake up to 30° after each blade and predicts far wake using the Bhagwat-Leishman free wake model [40]. The Leishman-Beddoes attached unsteady [41] and dynamic stall [42] models are used to predict the unsteady flow in the shed wake.

The specific version of UMARC used in this investigation (summarized in Table 4.1) is described in further detail by Bowen-Davies [29,32]. The analysis used here models an untwisted, constant-chord blade with a NACA 0012 profile. It does not account for a fuselage, corrections to root or shank drag (which was tared out during wind tunnel tests), or a wake trailer at the blade root. All cases have a trim target of zero first harmonic flapping for fixed collective angles.

Table 4.1: UMARC parameters used to model the 2017 wind tunnel tests

| Parameter | Description |
|---|---|
| No. time elements | 12 |
| No. spatial elements | 20 |
| No. blade modes | 10 |
| Nearwake | Weissinger-L model trailing 30° after the blade |
| Far wake | Bhagwat-Leishman model |
| Tip trailers | Single trailer |
| Root trailer | For vibratory predictions only |
| Blade shank correction | None |
| Fuselage model | None |

## 4.2 Rotor Performance

Rotor performance involves the measurement of steady hub loads: rotor thrust, drag, and side forces, pitching and rolling moments, and shaft power. Slowed rotors have the potential to significantly decrease the power required in forward flight by decreasing both the required shaft torque and by lowering the advancing tip Mach number and decreasing the profile drag on each blade.

### 4.2.1 Hover Performance

In hover, the flow has no forward velocity component and is symmetric to the axis normal to the rotor disk. Before wind tunnel testing, the rotor was mounted to the hover stand and tested for a range of rotor speeds from 500 to 1500 RPM.

Figure 4.1 shows how the thrust and shaft power vary with collective. The closeness of the data collected at different RPMs shows excellent precision and repeatability in the measured power and thrust values. The power required to operate is directly related to the rotor thrust.

From modified momentum theory [43], Eqn 4.1 provides a simple relation between the rotor thrust and power coefficients.

$$C_P = \frac{\kappa C_T^{3/2}}{\sqrt{2}} + \frac{\sigma C_{d0}}{8} \tag{4.1}$$

Because power only varies with thrust, the power and thrust for several different rotor RPMs collapse to the same line. This is shown in Fig. 4.2 along with

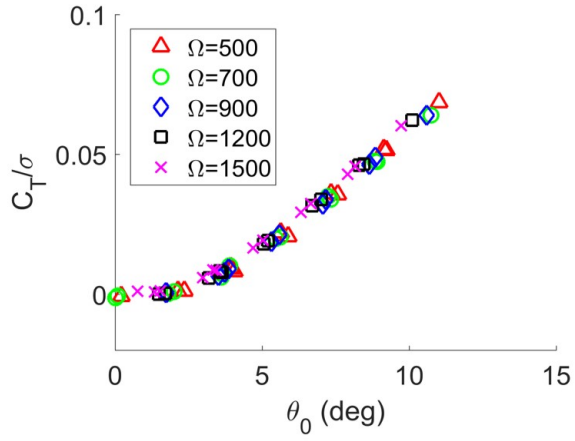


a) Rotor thrust versus collective pitch

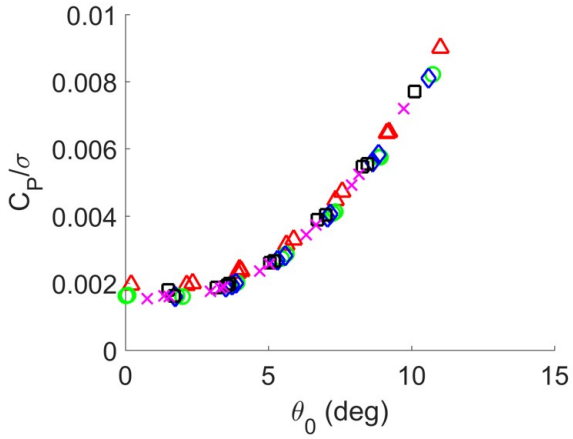


b) Shaft power versus collective pitch

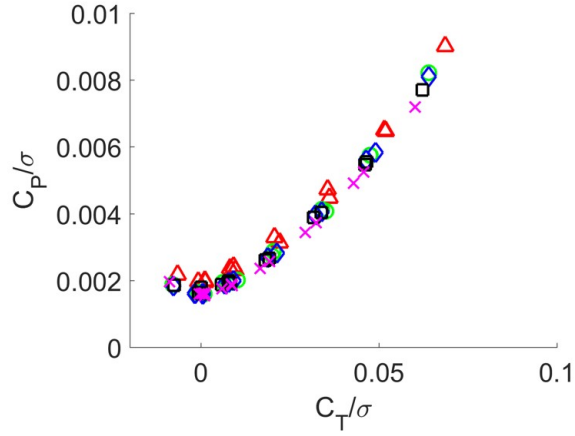


c) Shaft power versus rotor thrust

Figure 4.1: Rotor thrust and shaft power in hover for various rotor RPMs.

predictions using modified momentum theory.

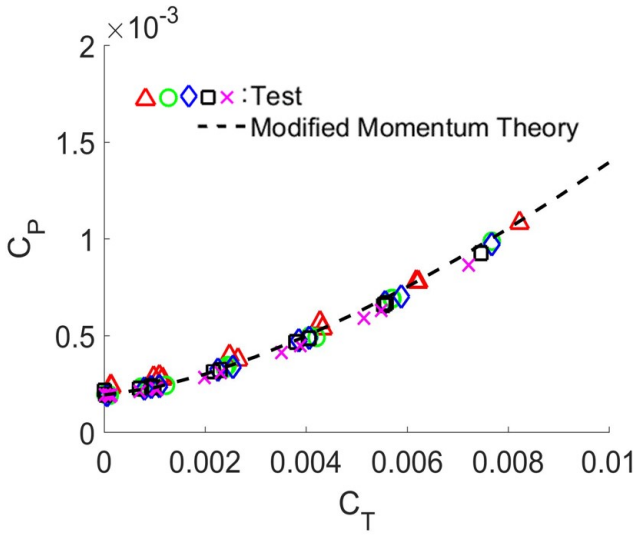


Figure 4.2: Simplified approximation of power to thrust in hover: experimentally-derived variables are $C_{P0} = .0002$, $C_{d0} = 0.0128$, and $\kappa = 1.7$ for this rotor.

### 4.2.2 Rotor Lift and Thrust Reversal

The lift of a rotor in forward flight is given by $L = Tcos(\alpha_s)$ - $Hsin(\alpha_s)$, where $\alpha_s$ is the shaft tilt angle and $T$ and $H$ are the rotor thrust and propulsive force, respectively. When there is no shaft tilt ($\alpha_s = 0$), the lift and thrust are equal.

Figure 4.3 shows the validation of lift versus collective pitch angle for advance ratios from 0.3 to 0.9. All cases were trimmed to zero first harmonic flapping of the reference blade, Blade 1, within a tolerance of 1°. Despite instabilities at the highest advance ratios and collective angles (e.g. $\mu = 0.9$ and $\theta_0 = 10°$), the rotor maintained the target trim well within 1.5°.

The trends are very well captured for all advance ratios; however, the slight difference between predictions and test data near $\theta_0 = 10°$ is an indicator of the

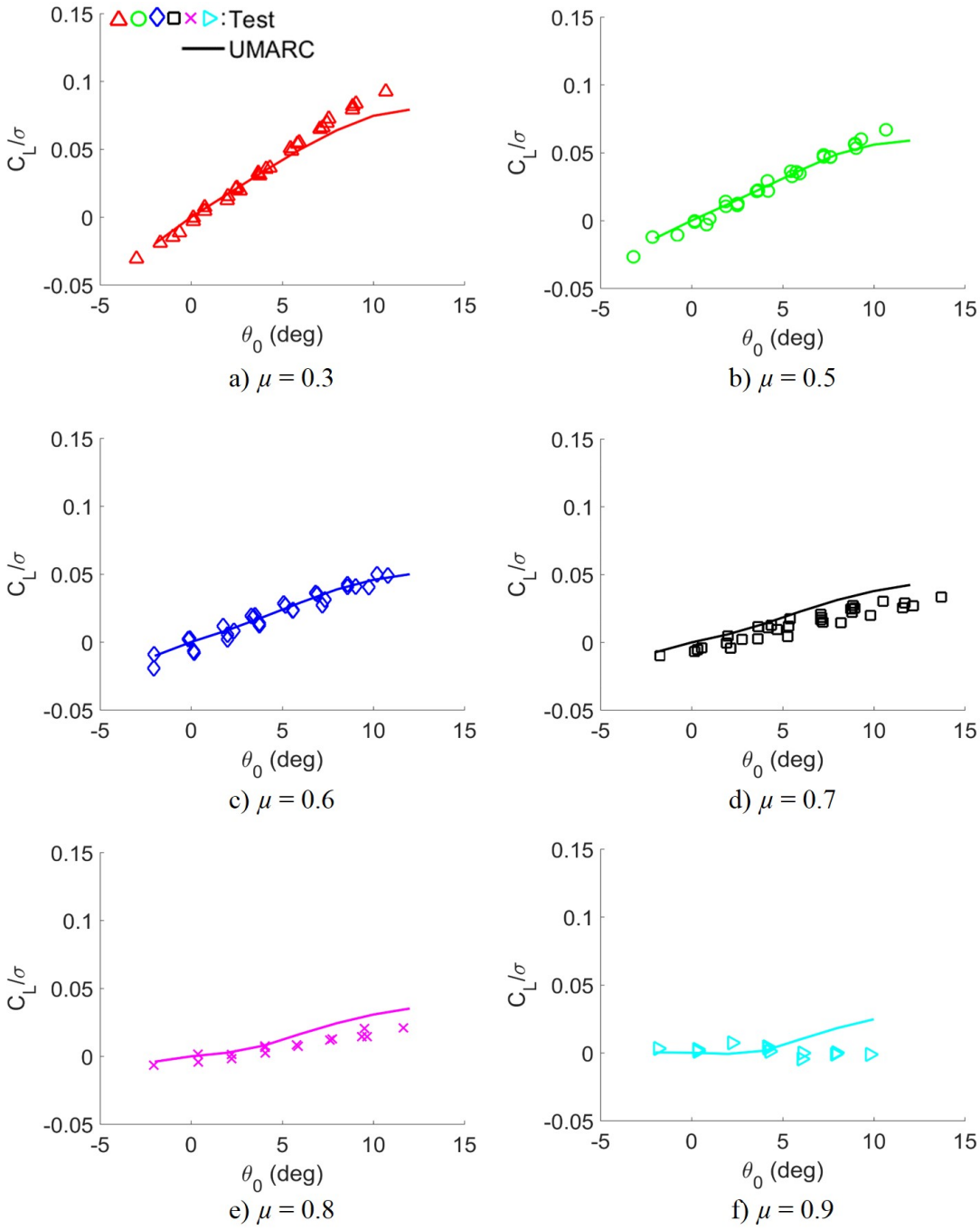


Figure 4.3: Non-dimensional rotor lift coefficient versus collective pitch at 900 and 1200 RPM; shaft tilt $\alpha_s = 0°$.

premature onset of stall in the model. For higher advance ratios ($\mu = 0.7$ or greater), the lift is slightly over-predicted for collective pitch angles greater than 5°. At $\mu = 0.9$, the slope agrees very well only for small pitch angles less than 5°. Overall, the slope of lift to collective angle in each case are well captured, demonstrating the decreasing thrust sensitivity to collective as advance ratio increases.

The slope, $dC_L/d\theta_0$, decreases with advance ratio because the dynamic pressure on the retreating-side blade is lower than that on the advancing side, which creates an asymmetry in lift. To counter the lift imbalance, the pitch on the retreating side is increased while the pitch on the advancing side is decreased using longitudinal cyclic. As advance ratio increases, the region of reverse flow on the retreating side of the rotor increases as well. An airfoil section in reverse flow experiences negative aerodynamic thrust when positive collective pitch is applied; therefore, increasing the pitch angle causes a decrease in thrust. This must be balanced out by decreasing the lift (and thus, the pitch) on the advancing side, resulting in a lower net lift being produced by the rotor.

At $\mu = 0.9$, the rotor thrust is no longer increased by changes in collective pitch and instead begins to decrease with higher $\theta_0$. This phenomenon, called thrust reversal, occurs when the negative lift on the retreating side becomes too large to be balanced out by the advancing side, and the rotor is only trimmed by producing net negative lift. Thrust reversal has been observed and discussed in several experimental investigations and analyses [12, 15, 16, 18, 26, 31, 32].

Collective-thrust reversal is shown in Fig. 4.4. The UMARC analysis, which calculates the slope using only small collectives near 0°, shows very good agreement

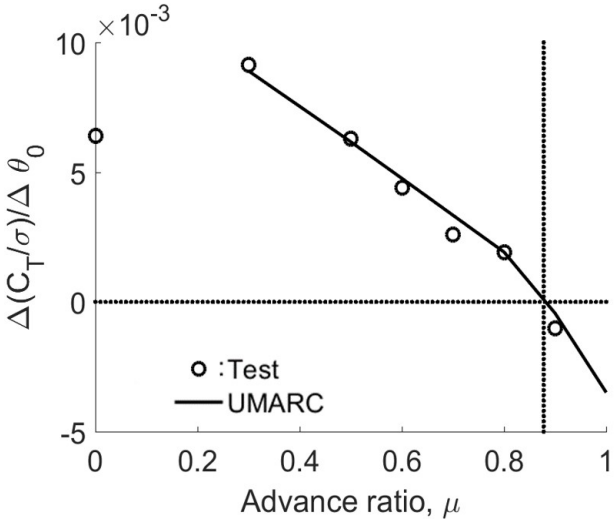


Figure 4.4: Decreasing thrust sensitivity to collective pitch for $\alpha_s = 0°$. Collective-thrust reversal occurs just before $\mu = 0.9$.

over the range of advance ratios. Thrust reversal occurs for this rotor at $\mu = 0.88$.

### 4.2.3 Shaft Power and Rotor Drag

The shaft torque coefficient of the rotor, which is measured using a torque cell on the shaft, is equivalent to the power coefficient of the rotor ($C_Q = C_P$). Figure 4.5 shows the correlation of rotor power coefficient to collective pitch for advance ratios up to 0.9. Only the 900 RPM cases are shown for clarity, but the 1200 RPM cases demonstrate the same trends with slightly higher magnitudes.

The predictions agree with the test data very well, especially for moderate collectives ($\theta_0 < 7°$). The power is slightly under-predicted for higher collectives at $\mu \leq 0.6$. At $\mu = 0.9$, when the majority of the retreating-side blade is in reverse flow, the shaft power is no longer affected by changes in collective. Required shaft

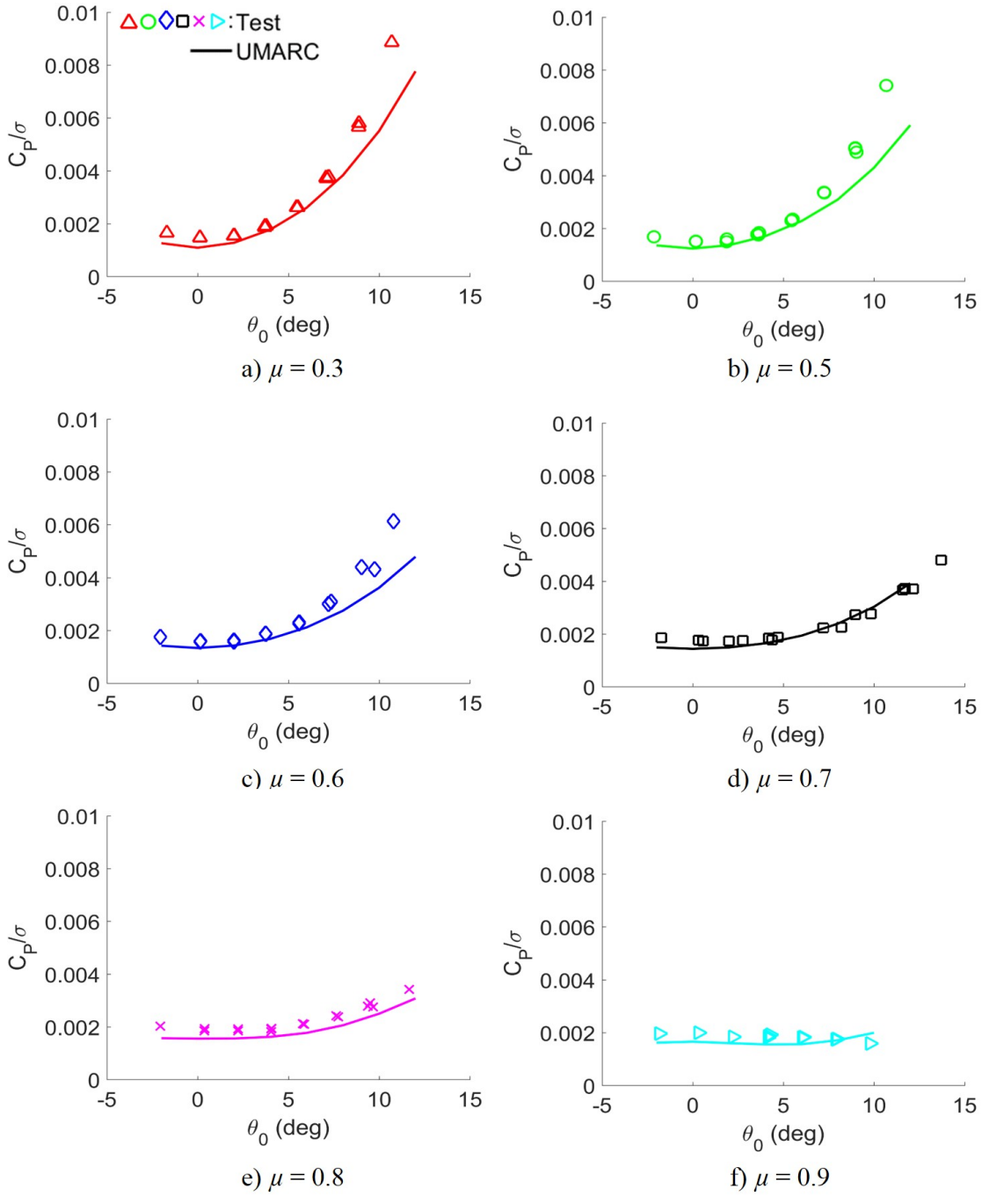


Figure 4.5: Non-dimensional shaft power coefficient versus collective pitch for 900 RPM; shaft tilt $\alpha_s = 0°$. The 1200 RPM cases (not shown for clarity) demonstrate the same trends with slightly greater magnitudes at low collectives.

power decreases slightly with increasing advance ratio because of the increasing drag on the blade in reverse flow, which serves to accelerate the rotor.

The drag of a rotor in forward flight is given by $D = Hcos(\alpha_s) + Tsin(\alpha_s)$, and is therefore equal to the H-force of the rotor when there is no shaft tilt. The drag of the rotor is isolated by subtracting out the drag due to the test stand and hub (see Section 3.4.4). The correlations shown in Fig. 4.6 are very good at advance ratios above 0.6, and the analysis captures the overall magnitudes as well as the increase in drag with higher collectives. At lower advance ratios, the predictions underestimate the drag at higher collectives and overestimate the drag at lower collectives. At the lowest advance ratio of $\mu = 0.3$, the prediction precisely captures the trend, especially for collectives less than 3°. The low level of scatter in the test data points, which represent the drag recorded at both 900 RPM and 1200 RPM, emphasizes the precision of the experimental data. In general, the drag approaches a small number near 0° collective, and subsequently increases with positive collective angles. There does not appear to be any significant change in damping with advance ratio. At $\mu = 0.9$, the freestream velocity is high enough that the drag at negative collectives begins to increase again, as expected.

A key measure of the performance of a rotor is its lift-to-drag ratio, which is defined by rotor lift, $L$, and equivalent drag, $(D_e)$, and given in Eqn 4.2.

$$\frac{L}{D_e} = \frac{C_L}{C_D + C_P/\mu} \tag{4.2}$$

The variation of lift-to-drag ratio with collective angle is presented in Fig. 4.7,

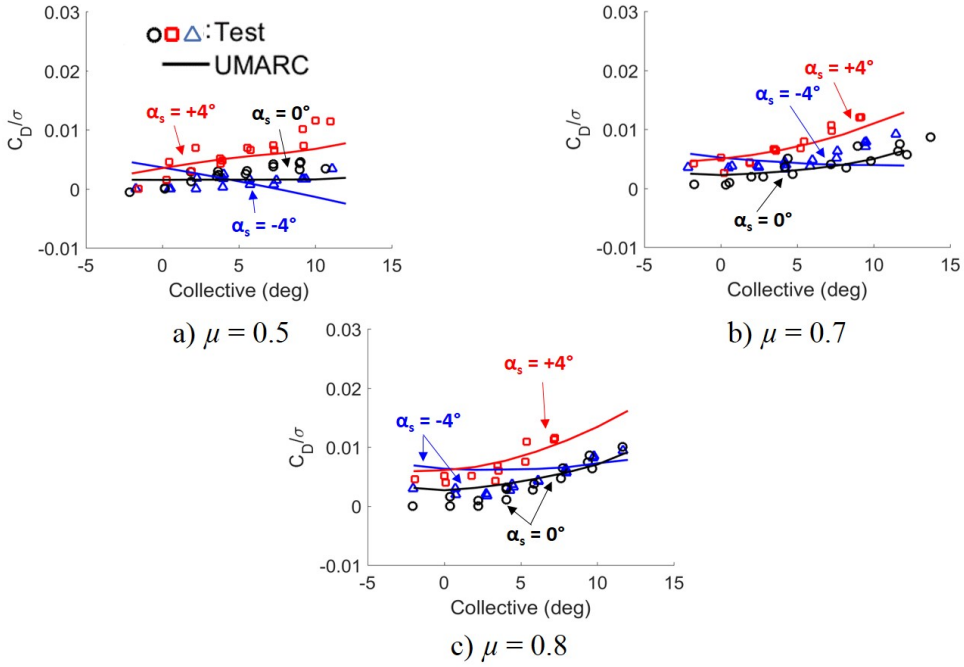


Figure 4.6: Nondimensional drag coefficient versus collective pitch at 900 and 1200 RPM; shaft angle $\alpha_s = 0°$.

and it shows very good correlation with UMARC predictions. Good agreement in rotor lift and power, both of which are of larger magnitudes, outweighs the poorer agreement of drag, which is of a much smaller magnitude, especially at low advance ratios. At higher advance ratios, where the agreement with the experimental drag data is much better, slight over-predictions in lift and under-predictions in power result in a small offset from the measured lift-to-drag. The trends are well captured, and the lift-to-drag ratio becomes less sensitive to changes in collective as the advance ratio increases. At $\mu = 0.9$, there is no longer any change with pitch angle. Overall, the lift-to-drag ratios are well predicted for the full range of advance ratios.

Figure 4.8 shows the validation of lift-to-drag ratio versus rotor thrust, which

again demonstrates a slight over-prediction of the maximum $L/D_e$. The overall trends are very well predicted, and show the net loss of lift due to reverse flow and retreating blade stall as the advance ratio is increased. For these cases at $\alpha_s = 0°$, the rotor performance steadily degrades with increasing advance ratio. Positive (aft) shaft tilt, however, is known to increase rotor performance at high $\mu$, and is discussed in Section 4.4.3.

### 4.2.4 Trim Cyclics

At each flight condition, the rotor was trimmed to zero first harmonic flapping amplitude by manipulating the lateral and longitudinal cyclic controls, as discussed in Section 3.4.5. Figure 4.9 shows the trends for lateral and longitudinal cyclics for advance ratios from 0.3 to 0.9. Longitudinal cyclic shows a clear trend, demonstrating an increasingly negative slope as advance ratio increases. The predictions capture the trends well, with a small offset of one to two degrees. As the advance ratio approaches 0.9, the change in the slope is of a smaller magnitude. The predictions for lateral cyclic show less agreement; this could be due in part to unsteadiness in the flow from the hub, which decreases the lift in the rear portion of the rotor disk. The offset in the predicted slope, however, is a feature that was not seen in previous comparisons [25,32] and may be the result of interference from the fuselage decreasing the lift at the forward portion of the rotor disk.

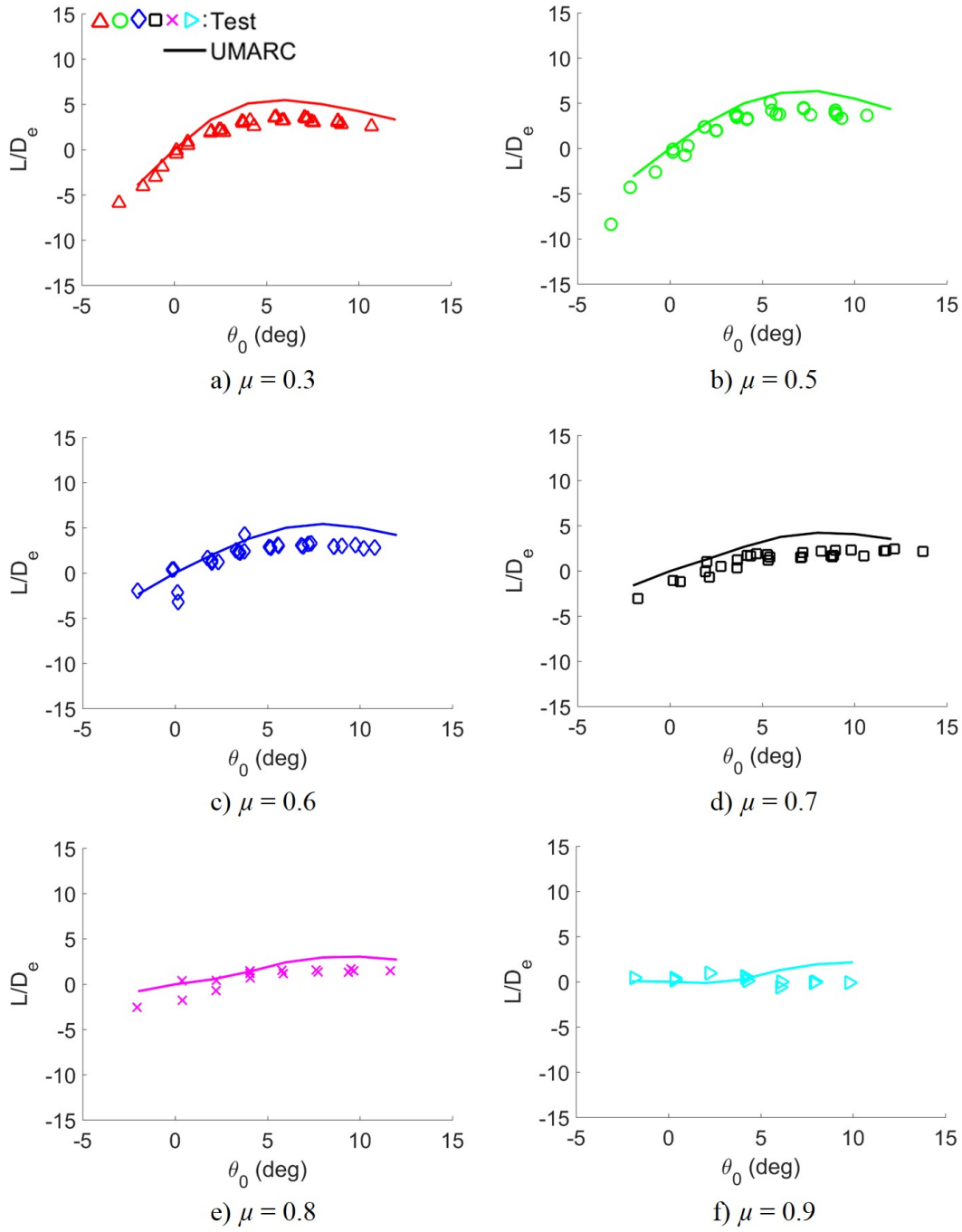


Figure 4.7: Lift-to-drag ratio versus collective pitch at 900 and 1200 RPM; $\alpha_s = 0°$.

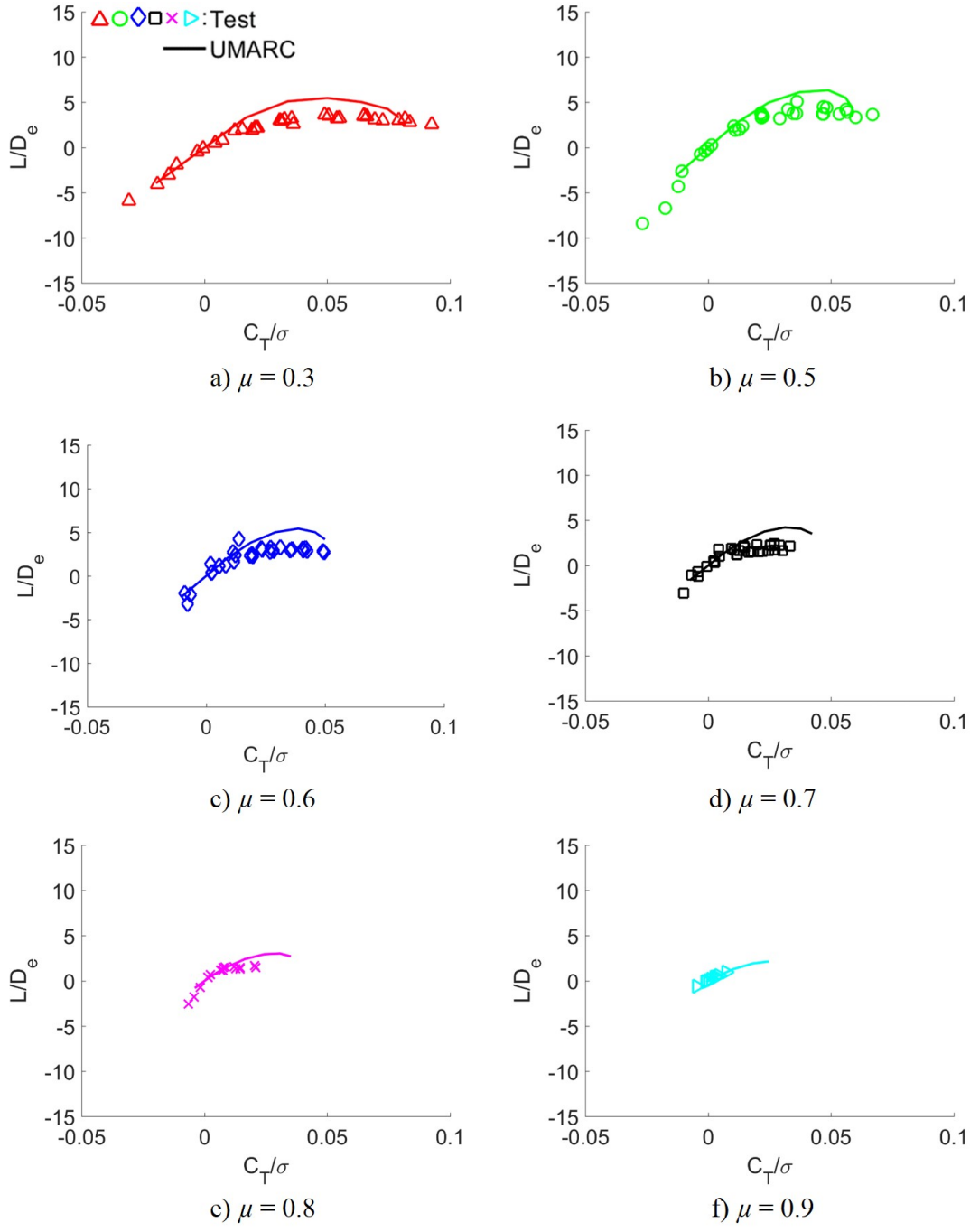


Figure 4.8: Lift-to-drag ratio versus lift coefficient at 900 and 1200 RPM; $\alpha_s = 0°$.

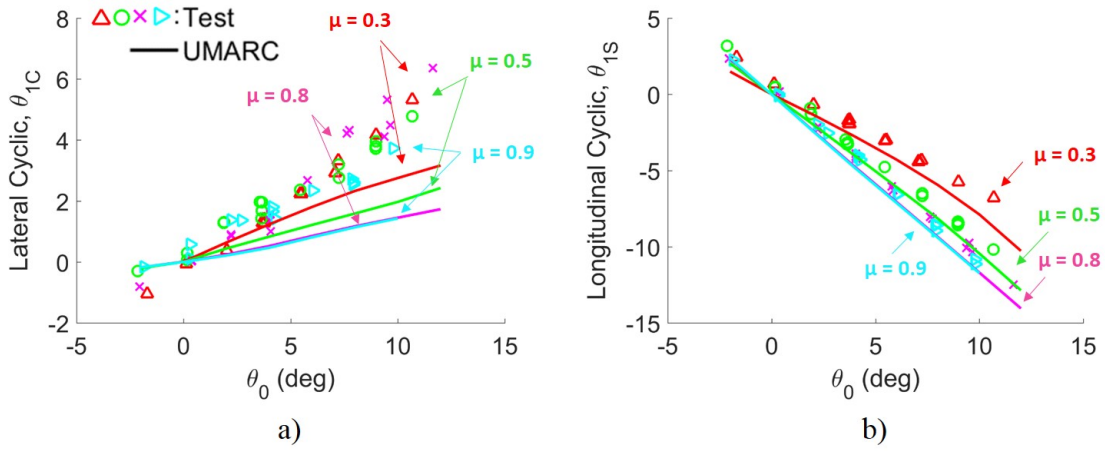


Figure 4.9: a) Lateral and b) longitudinal cyclics for select advance ratios at 900 RPM. The cyclics for 1200 RPM show the same trends with a slightly larger offset.

## 4.3 Vibratory Loads

The magnitudes of vibratory loads in a helicopter are an indicator of passenger comfort and can potentially impact the long-term health of mechanical components. Therefore, it is essential to understand the sources of vibration and be able to accurately predict them in analyses. The main rotor is the primary source of vibration in a helicopter, and care should be taken to avoid operation at a rotor RPM that would resonate with rotor harmonics. This would be especially important for future helicopters utilizing slowed rotors to achieve high speeds, since the rotor must operate at a range of RPMs while minimizing resonance effects.

A single rotor experiences periodic forcing which occurs at frequencies that are integer multiples of the number of blades (n/rev where n = 4, 8, 12... for a 4-bladed rotor). The loads that contribute to the frequencies that are integer multiples of

the number of blades are called vibratory loads, and all remaining harmonics are called oscillatory loads. The other vibratory harmonics (besides the blade passage frequency) are caused by dissimilarity in the blades, resulting in significant 1/rev loads in the fixed frame. The blade loads in the rotating frame are summed over the four blades to get the total fixed frame hub loads, which are measured by the hub balance on the rotor test stand.

Because of some level of dissimilarity between manufactured blades, experiments will not exactly reproduce the harmonics predicted by analyses that use perfectly identical blades. Large in-plane forces in experimental results (H-force and Y-force) indicate a mass imbalance such that the center of mass of the rotor is not exactly at the center of the shaft. This is exaggerated by centrifugal loading, and therefore is magnified by higher rotor RPMs. Rolling and pitching moments indicate a dissimilarity in the aerodynamic balancing or in the root pitch angle of the blades. Tracking the rotor is done to aerodynamically balance the blades; however, small moments in a rotor with very stiff blades will not always manifest as visible variations in the tip path plane and may not be balanced out.

The vibratory loads are calculated using harmonic decomposition to pick out the frequencies that make up the time history of the recorded data. A Fast Fourier Transform (FFT) performs this decompostion, identifying the vibratory loads in terms of rotor harmonics. This section presents the measured vibratory hub loads from wind tunnel tests.

A fanplot for this rotor was calculated using UMARC and is presented in Fig. 4.10. At the main operational rotor speed of 900 RPM, the third flap bending

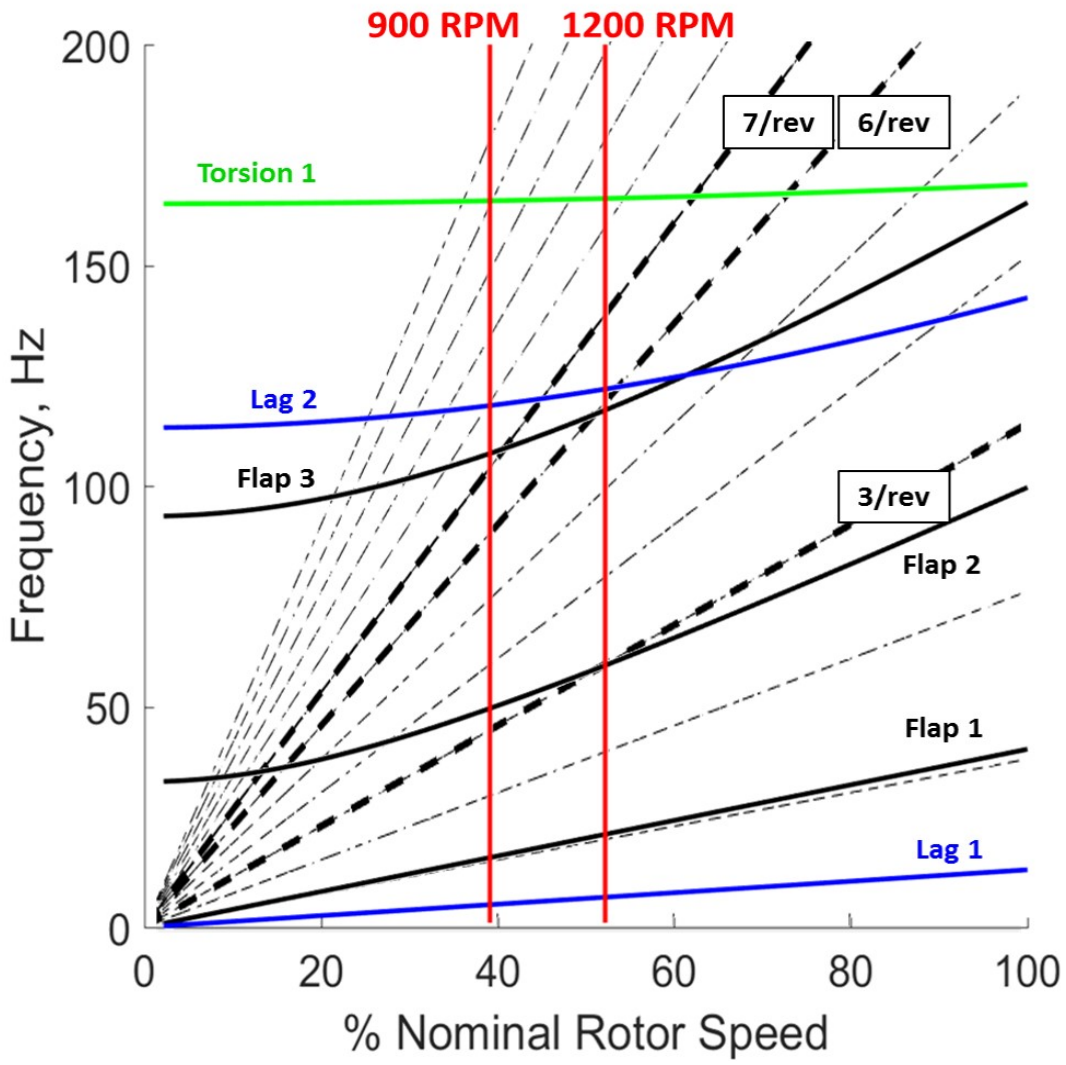


Figure 4.10: Calculated fanplot of this rotor at multiple rotor speeds, with the operational RPMs for this investigation marked in red.

mode approaches 7/rev, and the torsion mode is near 11/rev. At 1200 RPM, the second flap bending mode interacts with the 3/rev frequency of the rotor, the third flap mode approaches 6/rev, and the torsion mode is near the 8/rev harmonic.

The experimental hub loads shown in Figs. 4.11 show a dominant 4P and a small 8P component, which would be expected from a 4-bladed rotor. A large 1P component is also present in the vertical and in-plane forces, which is indicative of

an imbalance in the hub and rotor. The in-plane 1P components are not changed with increased advance ratio, while the vertical 1P component does increase with advance ratio. Because the in-plane forces are unaffected by aerodynamic changes, this implies the presence of a mass imbalance in the rotor hub; however because the amplitudes of the vertical force do increase with advance ratio, the presence of an aerodynamic imbalance is also likely. As advance ratio increases, the 4/rev vertical force increases as well. The 4/rev in-plane forces also increase with advance ratio, though at $\mu = 0.8$ and 0.9 the in-plane forces are significantly lower.

The test stand accelerations were also measured, and are shown in Fig. 4.12. A 3-axis $\pm 16$ g accelerometer mounted to the test stand measured the vertical and in-plane vibrations of the test stand, and verifies that the 4P harmonic dominates the vertical forcing, while the 1P and 4P harmonics dominate the in-plane forces.

The 4P component of the vertical force is shown in Fig. 4.13, and clearly increases in both slope and magnitude as advance ratio increases. At low $\mu$, the 4/rev component of $F_z$ is less affected by changes in collective, but at higher $\mu$ it tends to increase with collective. Experimental results for $\mu = 0.7$ show the minimum value of 4/rev vertical forcing occurs at $0^\circ$ collective, as theory suggests; however, at other high $\mu$ cases this point appears to fall within $\pm 2^\circ$ in the measured data. Other authors [32] have attributed this offset to an inability to accurately predict the lateral cyclic, which may be related to the disturbances in the flow past the hub. The UMARC predictions capture the trends very well compared to the measurements, demonstrating an overall increase in the slope of the 4/rev components with increasing advance ratio. The magnitudes are very well predicted

at low $\mu$ without the use of a dynamic stall model, while at high $\mu$ predictions improve with the use of a dynamic stall model as well as inboard trailers. Noticeable discrepancies appear in the moderately high range of advance ratios near 0.6, where the prediction under-estimates the magnitude of the 4/rev response.

## 4.4 High Advance Ratio Studies

Three studies were carried out in the high advance ratio flight regime using this rotor and test stand. First, an attempt was made to benchmark the effect of utilizing highly similar, non-instrumented rotor blades. The effect of adding a faired fuselage to the test stand was investigated, the results were compared to previous tests using the same rotor without a fuselage. Finally, the effect of longitudinal shaft tilt angle on rotor performance was investigated. The results and discussion for each of the three studies are provided below.

### 4.4.1 Effect of Blade Similarity

The root flap and pitch angles of each of the four blades were recorded using Hall effect sensors mounted to the blade root grip. Flapping angles are affected by differences in blade structural, inertial, and aerodynamic properties; as advance ratio increases, the differences in the characteristics of each blade are exaggerated and are reflected in the flap angle time histories. The azimuthal histories were converted to the frequency domain, and the harmonics of the rotor speed were extracted. The trim target for each flight condition was zero 1/rev (1P) flapping; therefore the 1/rev

flap angles, $\beta_{1C}$ and $\beta_{1S}$, of Blade 1 were minimized to achieve trim. All other blades were tracked (see Section 3.4.5) to match the tip path plane of Blade 1, which was used as the reference blade during testing.

The flapping amplitudes shown in Fig. 4.14 indicate the trim state of the rotor for each advance ratio tested. The rotor is considered to be ideally trimmed if the flapping amplitude falls within a tolerance of 1°. The 1P amplitude remains within the target trim value until an advance ratio of 0.7, when the 1P flapping of two blades increases to just above 1° and the rotor no longer achieves ideal trim. It should be noted that in trimming the rotor, only the 1/rev flap of the reference blade, Blade 1, is minimized. However, the 1/rev amplitudes of the other three blades are less than 1° with respect to the reference blade. Because the swashplate controls are only capable of steady and 1P inputs, even the trimmed rotor could be affected by higher harmonics. The 2P flapping amplitudes of all the blades increase steadily with advance ratio, which may affect the rotor trim state. Fig. 4.15 shows the flapping amplitudes of each blade for the first eight harmonics, which demonstrate an overall increase in amplitude with increasing advance ratio. While the 1P and 2P components dominate the flap response, a 3P and a 4P component are also present.

The blade flapping motion over the rotor azimuth is shown in Fig. 4.16 for a collective angle of 4°. Dashed vertical lines at 225° and 315° indicate the points along the rotor azimuth where the blades were tracked using the strobe light procedure described in Section 3.4.5. At each flight condition, the rotor was tracked at 4° collective before a collective sweep was carried out. The tracking process ensures the blades follow the same tip path plane (TPP), and this is reflected in the recorded

flap motion for the individual blades. Maximum forcing on a rotor generally occurs at the region of maximum dynamic pressure, which is between 45° and 135° azimuth. Because this is an articulated rotor, maximum flapping due to this forcing occurs between 135° and 225°. The measured data shows maximum peak-to-peak flapping generally occurs at 225°, approximately 90° after the region of maximum forcing on the advancing side.

Figure 4.16 shows that at the relatively low collective pitch of 4°, the blades are well tracked for advance ratios less than 0.7. The maximum peak-to-peak flapping of the tracked rotor ($\mu$ = 0.3 - 0.6) is less than 1.5°, which is nearly one-third of the peak-to-peak flapping observed in the same rotor with instrumented blades at the same flight condition and rotor RPM [25]. At higher advance ratios, tracking becomes more difficult to achieve because the blades no longer follow the same path around the rotor azimuth. This is the result of structural, inertial, or aerodynamic dissimilarities in the blades and hub that get exaggerated at these more extreme flight regimes. A set of non-instrumented blades were structurally tested to ensure no more than 2.5% variance in mass, inertia, natural frequency, and bending and torsional stiffness, and this higher level of similarity enabled improved rotor track and trim up to an advance ratio of 0.7. The results show that the process of instrumenting rotor blades for wind tunnel testing inherently affects the characteristics of the blades: external sensors and wiring may significantly affect blade aerodynamic properties, while embedded instrumentation can affect the inertial matching or structural response of the blades. Improvements in blade fabrication and incorporation of instrumentation are necessary to achieve track and trim at high advance

ratio and to accurately model a rotor in this flight regime.

### 4.4.2 Effect of Fuselage

A limited study on the effects of a fuselage (Fig.4.17) was carried out for both low and high advance ratios. First, a test was carried out with the rotor used in the present research at $\mu = 0.3$ and for 700, 900, and 1200 RPM with and without a fuselage. The measured data from this first study (not pictured) shows no appreciable differences between rotor performance or controls with or without the fuselage. Due to limited time in the wind tunnel, a follow-up study at a higher advance ratio was not performed; therefore, to evaluate the effects of a fuselage at higher speeds, a previous test with a similar rotor was used to provide a comparison.

This second rotor, which was operated without a fuselage, was tested in a previous wind tunnel entry in late 2016 [44]. In addition to testing without a fuselage, the second rotor also utilized instrumented blades that were slightly heavier than the blades used in the present work. First, a collective sweep was carried out at a low advance ratio of 0.3 at a rotor speed of 900 RPM; the results are shown in Fig. 4.18. The two rotors demonstrate the same thrust, power, and drag, but differ in the slope of the lateral and longitudinal cyclic versus collective. Next, the measurements from the two rotors at $\mu = 0.7$ and 900 RPM were compared (Fig. 4.19). Rotor thrust, drag, and lift-to-drag are approximately the same, but required shaft torque is slightly higher for the heavier, instrumented blades of the second rotor. Once again, the change of lateral and longitudinal cyclics versus

collective differed between the two rotors; the rotor tested with a fuselage shows a shallower, less positive slope for lateral cyclic controls ($\theta_{1C}$) versus collective as the advance ratio is increased. For the same rotor-fuselage setup, the longitudinal cyclic controls ($\theta_{1S}$) also demonstrate a steeper, more negative slope than the rotor without a fuselage. These trends remain true as the advance ratio increases to $\mu$ = 0.9. This effect is likely a result of the flow over the front of the fuselage, which adds an effective upwash to the fore portion of the rotor disk. Therefore, greater positive inputs of lateral cyclic are required to trim the rotor over the entire range of advance ratios.

### 4.4.3 Effect of Shaft Tilt Angle

Longitudinal shaft tilt angles of positive (aft) and negative (forward) 4° were investigated at 40% and 50% nominal rotor speed to expand the test envelope of previous work at the University of Maryland [25, 31]. Collective sweeps were performed and rotor performance data was measured for advance ratios of 0.5, 0.7, and 0.8. Figures 4.20 through 4.24 describe the effects of shaft tilt on rotor lift, torque, drag, and lift-to-drag ratio. The effects of shaft tilt on thrust sensitivity to collective are shown in Fig. 4.20, and indicate that shaft tilt does not significantly impact the point of thrust reversal. The measurements presented in Fig. 4.21 show that rotor lift increases significantly with positive shaft tilt for the full range of collective angles; similarly, negative shaft tilt reduces rotor lift for all collectives. The prediction of lift agrees very well with the measured data at lower collective angles, and

captures the trend for higher advance ratios of 0.7 and 0.8. At $\mu = 0.5$, the effects of premature stall can be seen in the analysis in the 0° and +4° cases. Overall, the lift prediction correlates very well to experimental data.

Shaft tilt has a much less pronounced effect on torque (Fig. 4.22), notably decreasing the power required at low collectives for both fore and aft shaft tilt. Above 5° collective at $\mu = 0.5$, positive shaft tilt requires slightly more power than when $\alpha_s = 0°$. This reversal point occurs at higher collectives as advance ratio increases. The analysis also shows this reversal point, at which aft shaft tilt begins to draw more power than both fore and zero shaft tilt. By comparison, negative shaft tilt draws less power until a sufficiently high collective is reached, at which point negative shaft tilt approaches the same required power as zero shaft tilt. UMARC analysis captures these trends very well, though the magnitudes are slightly under-predicted across all collective angles.

Drag increases for both fore and aft shaft tilt, though aft shaft tilt demonstrates higher drag for all positive collectives (Fig. 4.23). At higher advance ratios, the drag produced by forward shaft tilt is approximately equal to that of zero shaft tilt. The predicted drag agrees well with experimental results for zero and aft shaft tilt, demonstrating the appropriate magnitudes and slopes for most of the collectives tested. Agreement with negative shaft tilt data, however, is poor; drag is under-predicted at lower collectives and over-predicted at higher collectives.

These errors are present in the predictions of lift-to-drag ratio (Fig. 4.24), but because the magnitude of the drag component is small compared to lift and torque, the effects of poor drag correlation are minimal. The lift-to-drag predictions

agree with the measured results very well, though the analysis tends to overestimate lift-to-drag at low advance ratio and at higher collective angles; this is primarily a result of the under-predicted power combined with the over-predicted lift. The experimental trends are very well represented in the analysis, which clearly shows the performance benefits of rearward shaft tilt at lower collectives and high advance ratio up to 0.9. This level of predictive capability would therefore be useful for rotor design studies.

## 4.5 Support for Other Tests

In 2017, Lind et al. [45] conducted an investigation into the high advance ratio flow environment of the same non-instrumented rotor used in this work. The present research and the investigations by Lind et al. were conducted simultaneously in the GLMWT, in which Lind et al. performed PIV on a subset ($\mu \leq 0.9$, $\alpha_s = 0$, 900 RPM, advancing tip Mach number of 0.45) of the overall wind tunnel test envelope of this work. Rotor track and trim was performed in support of this investigation, and involved careful planning to construct an environment in the wind tunnel test section that would be conducive to the use of PIV. To highlight the particles used to seed the wind tunnel, all ambient light was blocked from infiltrating the test section. This was accomplished by placing light-absorbing sheets of black tape on the inner walls of the test section, which limited the maximum wind tunnel speed that could be safely tested to a corresponding advance ratio of $\mu = 0.9$ at 900 RPM and $\mu = 0.7$ at 1200 RPM.

Time-resolved and phase-averaged PIV was used to experimentally characterize the unsteady flow at 40% span, well within the reverse flow region, at advance ratios up to $\mu = 0.9$. Evidence of a reverse flow dynamic stall vortex, believed to be the main source of unsteadiness in the reverse flow region of a rotor, was observed between advance ratios of 0.6 and 0.9, and is presented in Fig. 4.25. A classical dynamic stall vortex, traveling from geometric trailing edge to the geometric leading edge because of reverse flow, is evidenced by the wake convected downstream of the geometric leading edge of the retreating-side blade. A blade-vortex interaction is captured at $\mu = 0.7$, and a tip vortex is observed to travel through the rotor wake. At the time of this writing a detailed discussion of this interrogation of the reverse flow region of this rotor is not yet published, but future analysis of these results will provide a deeper understanding of the effects of vortex dynamics of rotor lift and moment stall.

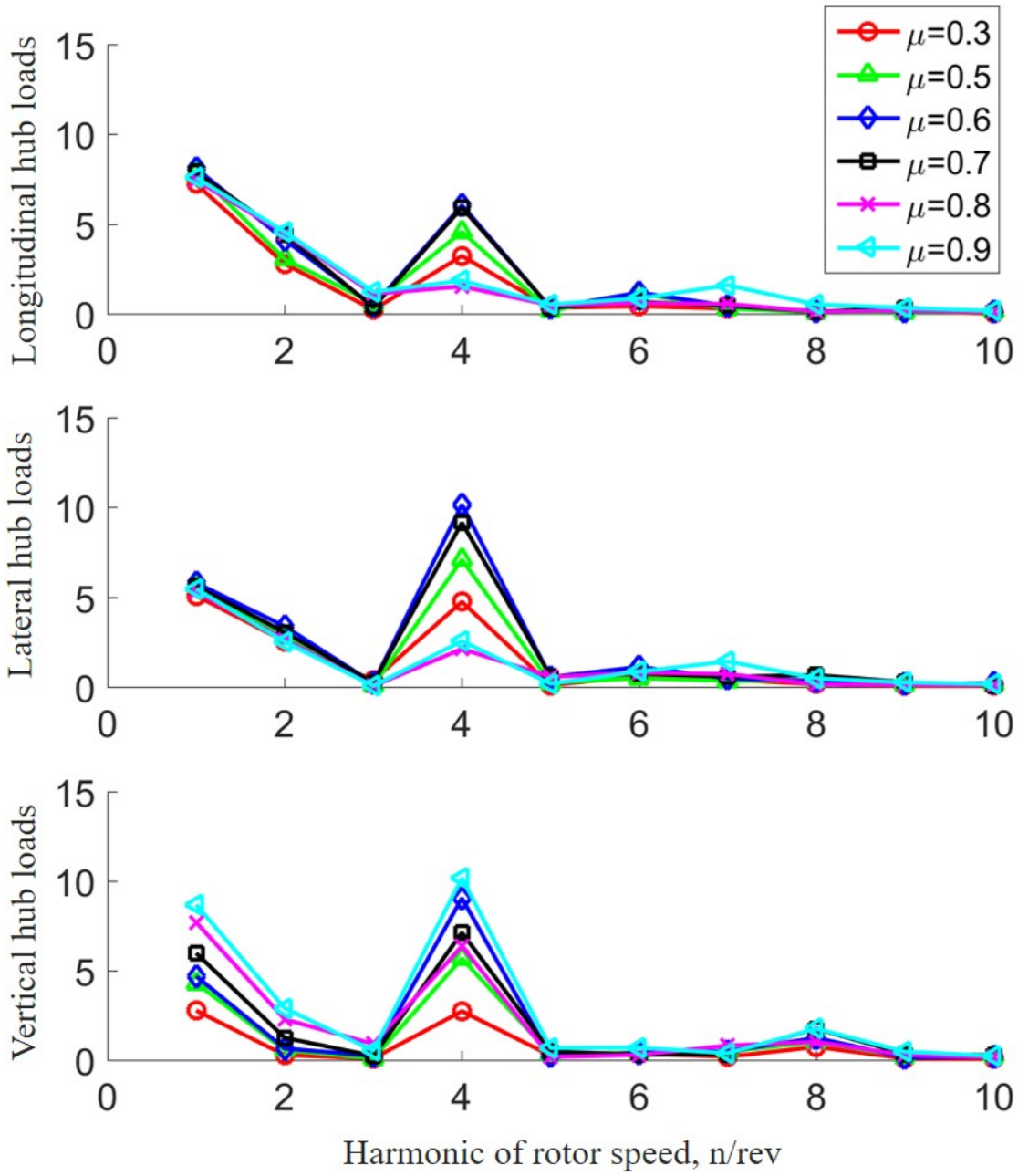


Figure 4.11: Amplitudes of oscillatory hub loads for in-plane forces ($F_x$ and $F_y$) and normal out-of-plane force ($F_z$). Results shown were observed at 900 RPM and trimmed at 4° collective.

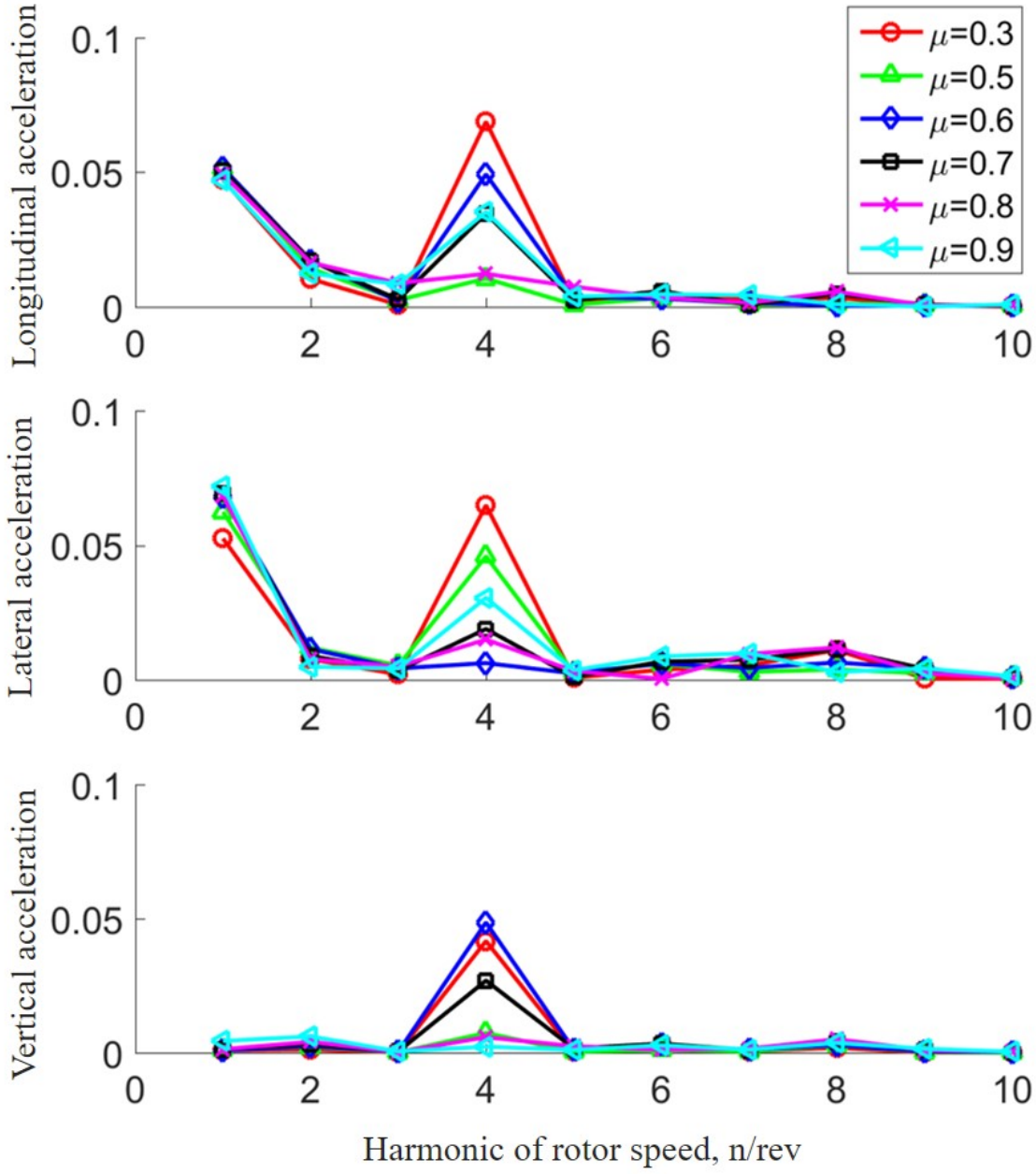


Figure 4.12: Amplitudes of test stand accelerations for in-plane accelerations ($a_x$ and $a_y$) and normal out-of-plane acceleration ($a_z$). Results shown were observed at 900 RPM and trimmed at 4° collective.

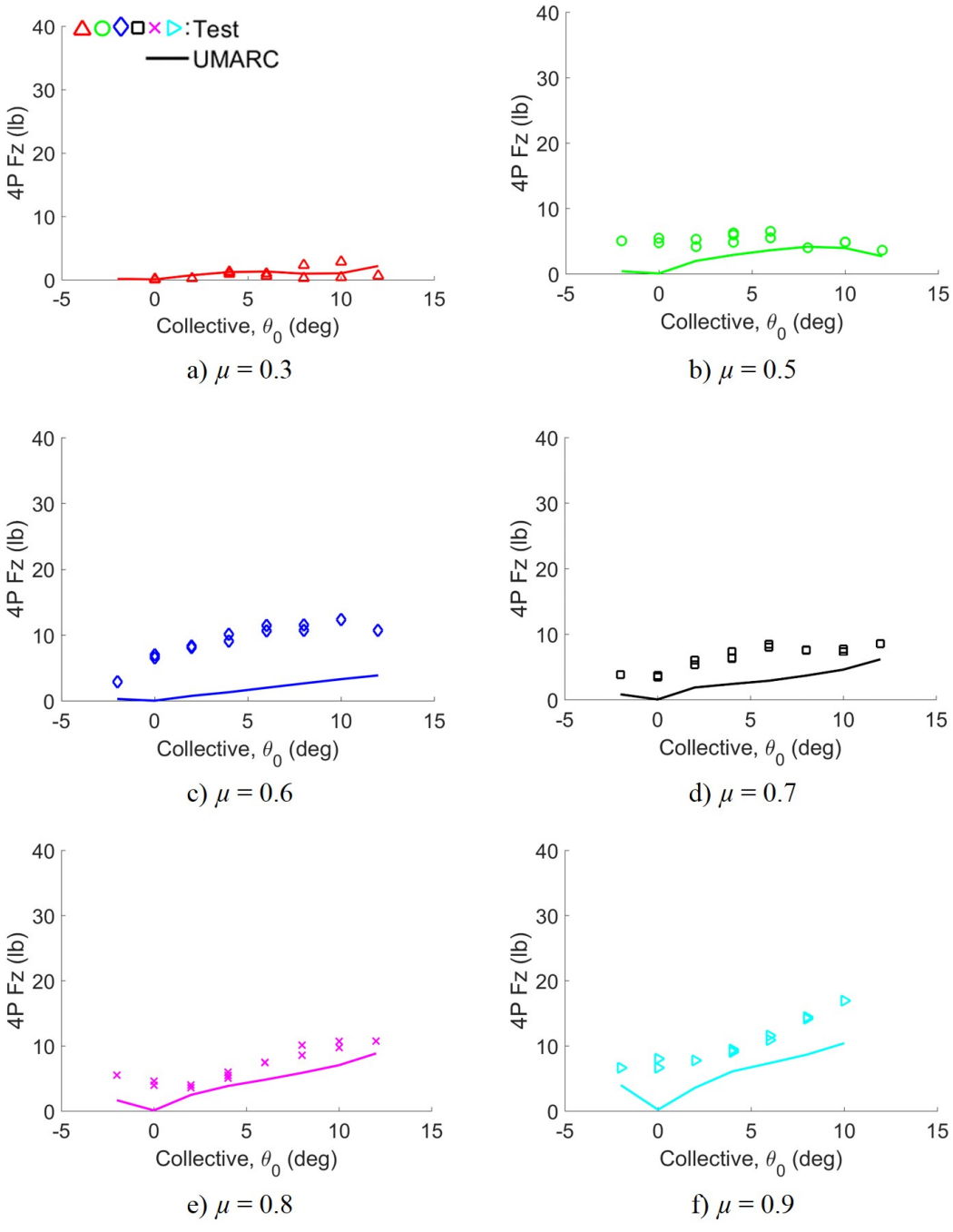


Figure 4.13: 4/rev component of the vertical force ($F_z$) plotted with increasing advance ratio at 900 RPM; shaft tilt $\alpha_s = 0°$.

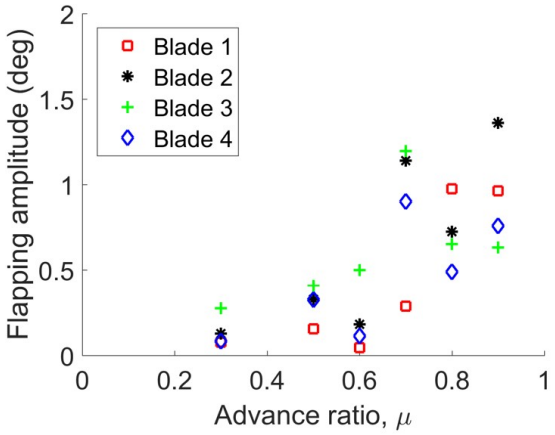


a) 1/rev blade flapping amplitude versus μ

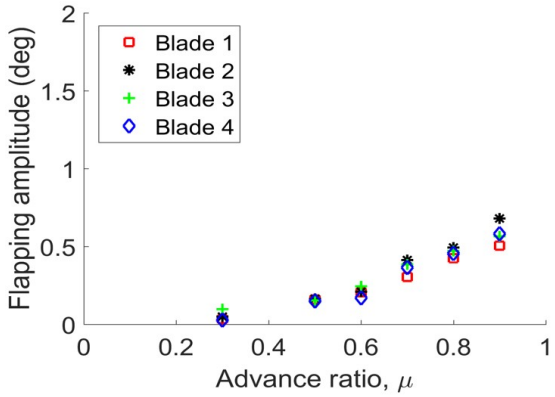


b) 2/rev blade flapping amplitude versus μ

Figure 4.14: Flapping amplitudes of the four blades for the range of tested advance ratios. The rotor was trimmed to zero 1/rev flap of the reference blade 1. All data shown is at 4° collective.

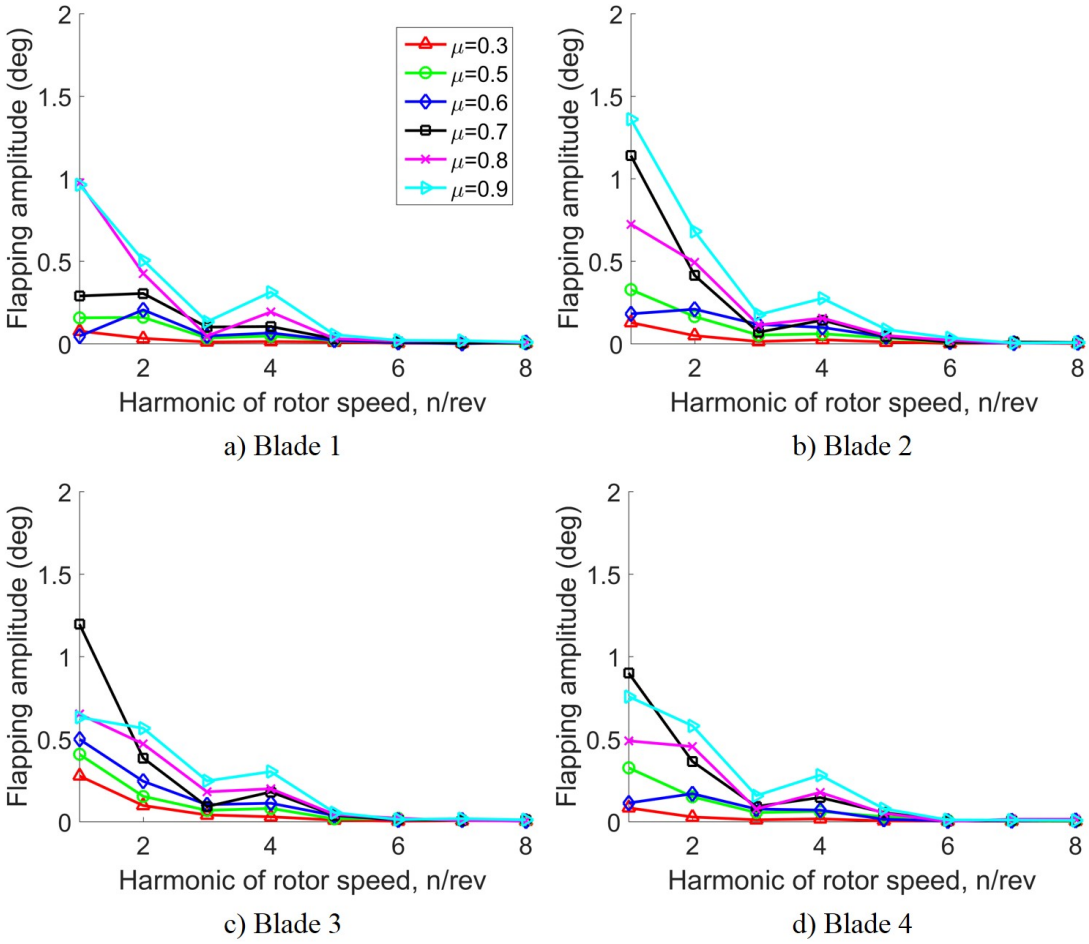


Figure 4.15: Flapping amplitudes of each blade for harmonics from 1P to 8P. All data shown is at 4° collective, 900 RPM, and $\alpha_s = 0°$.

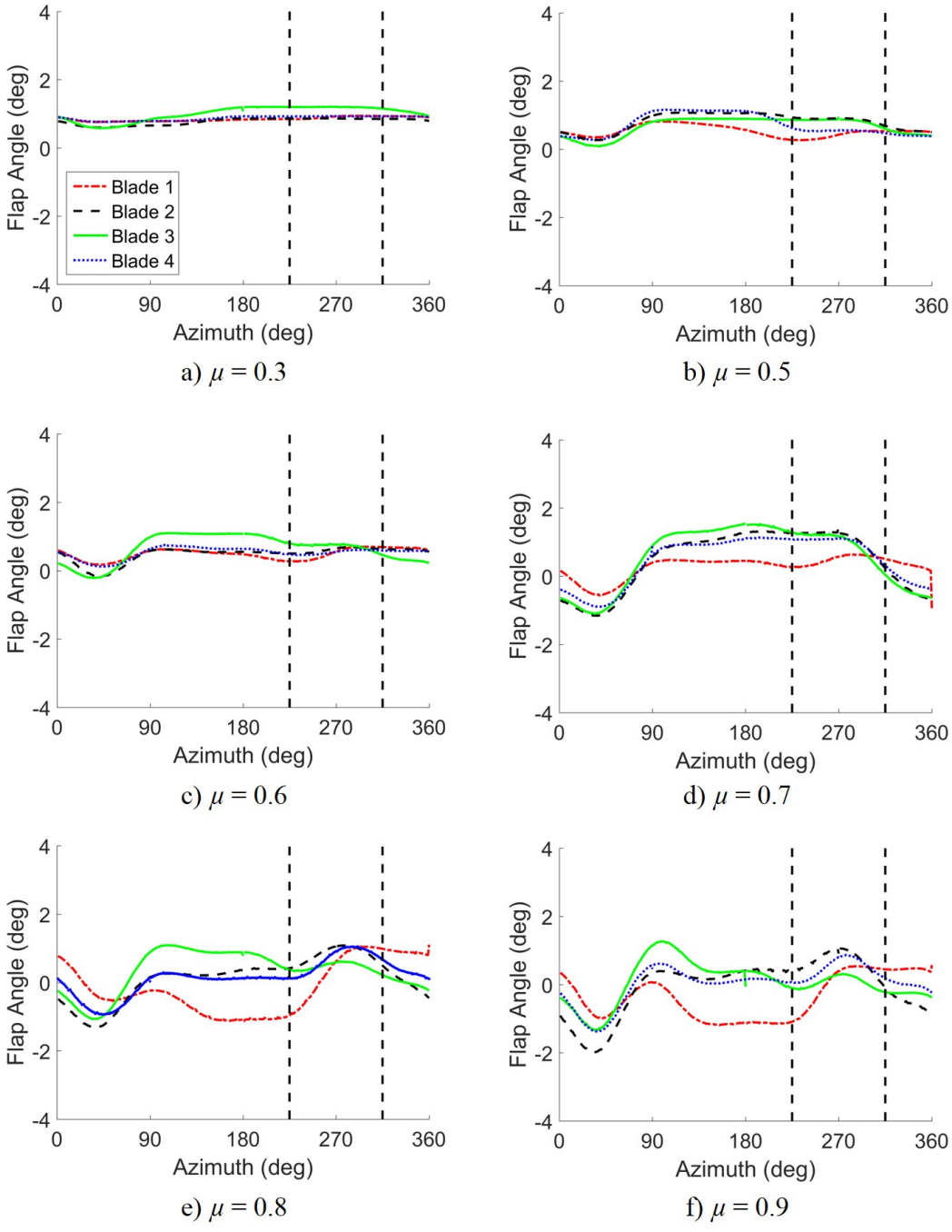


Figure 4.16: Phase-averaged flapping amplitudes versus azimuth for each blade. Vertical lines indicate azimuths where blades were tracked using the strobe light setup. All data shown is at 4° collective, 900 RPM, and $\alpha_s = 0°$.

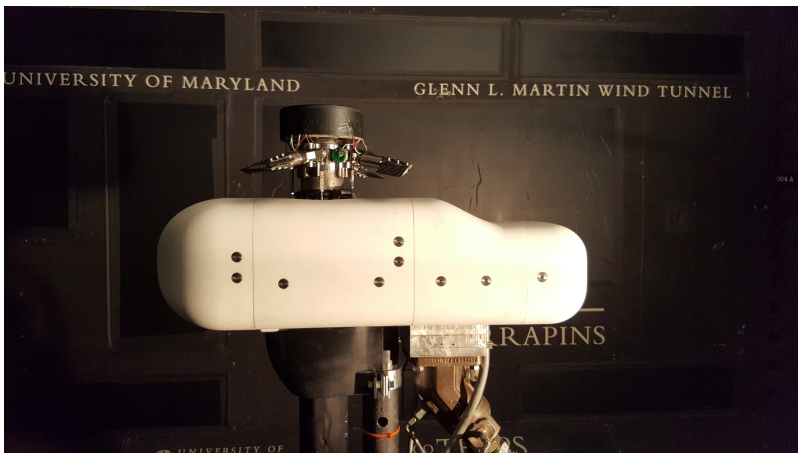


Figure 4.17: A 3-D printed nylon fuselage was mounted to the rotor stand for the majority of tests.

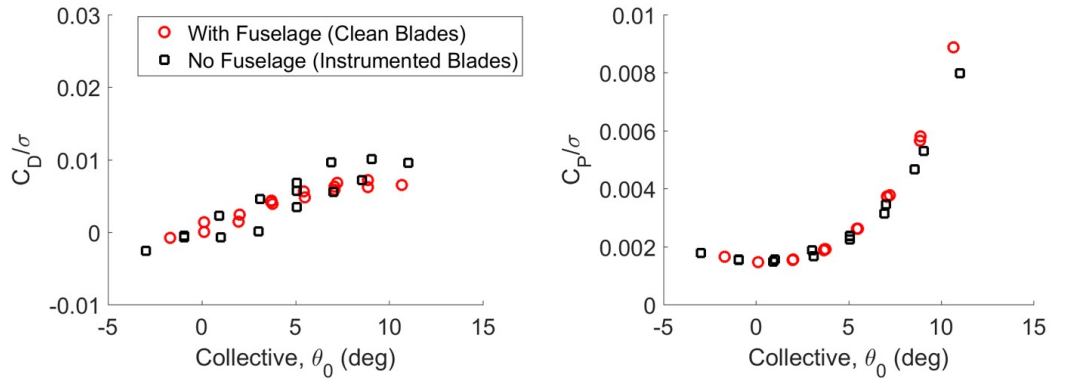


a) Drag versus collective




b) Shaft power versus collective

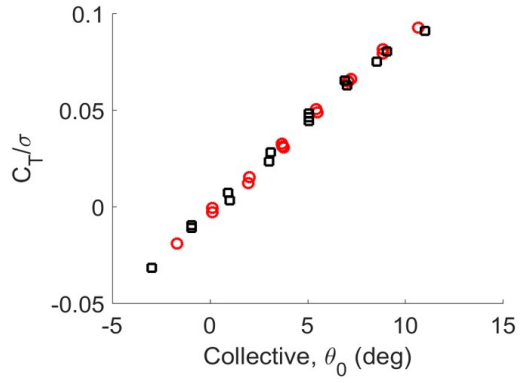


c) Thrust versus collective

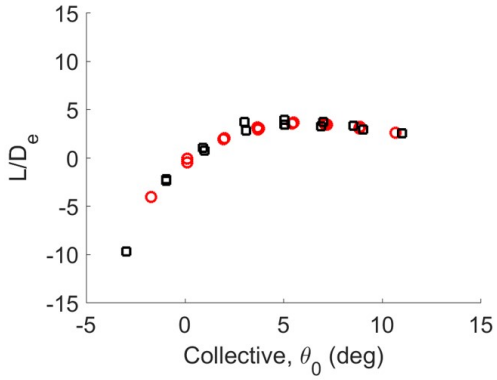


d) Lift-to-drag versus collective

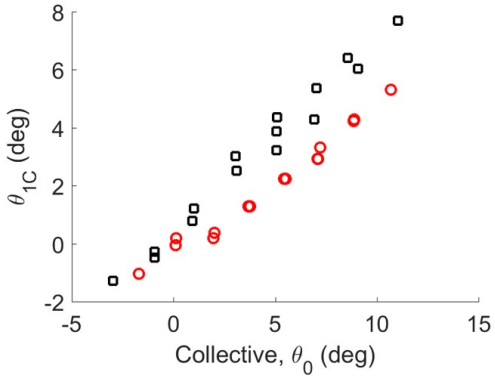


e) Lateral cyclic versus collective

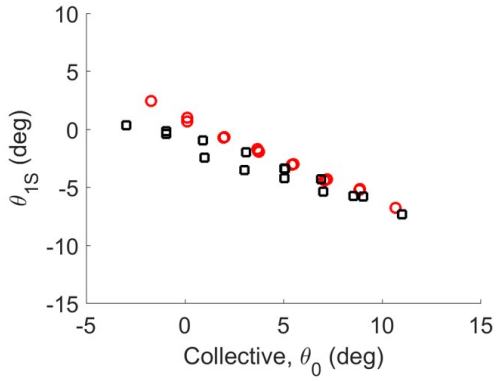


f) Longitudinal cyclic versus collective

Figure 4.18: Effect of fuselage at low advance ratio ($\mu = 0.3$) for instrumented and non-instrumented blades.

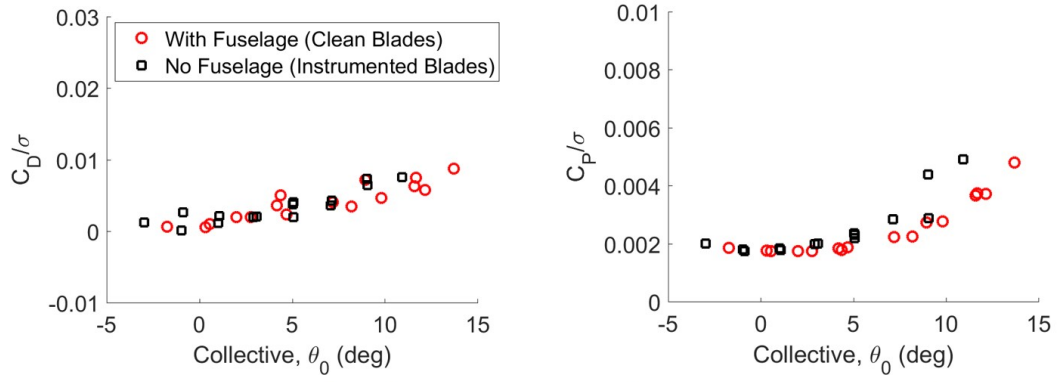


a) Drag versus collective




b) Shaft power versus collective

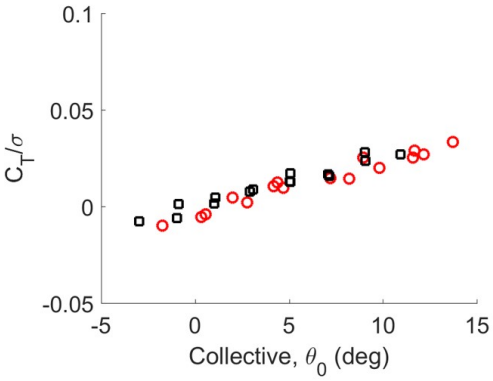


c) Thrust versus collective

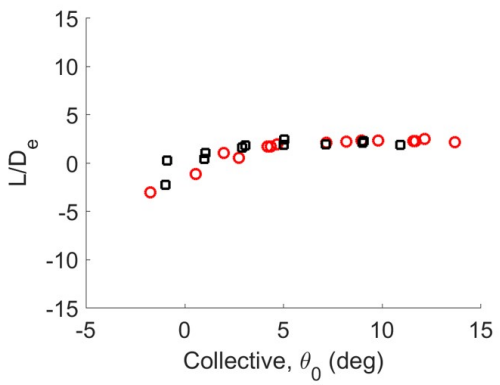


d) Lift-to-drag versus collective

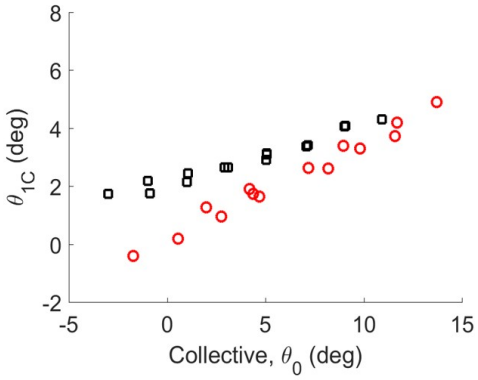


e) Lateral cyclic versus collective

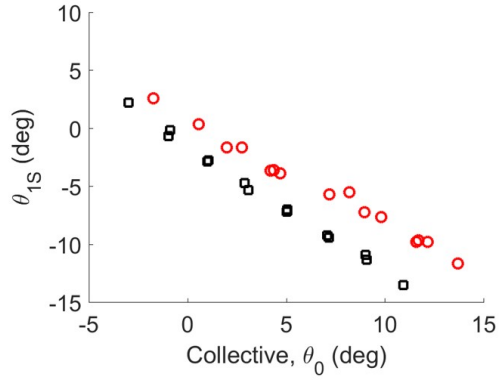


f) Longitudinal cyclic versus collective

Figure 4.19: Effect of fuselage at high advance ratio ($\mu = 0.7$) for instrumented and non-instrumented blades.

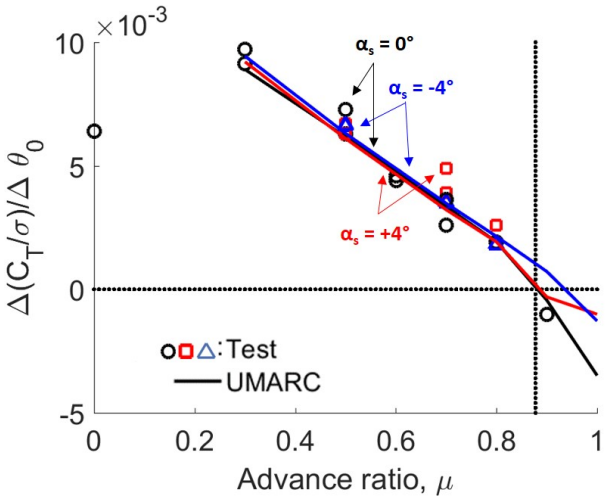


Figure 4.20: Effect of shaft tilt on thrust sensitivity to collective pitch.

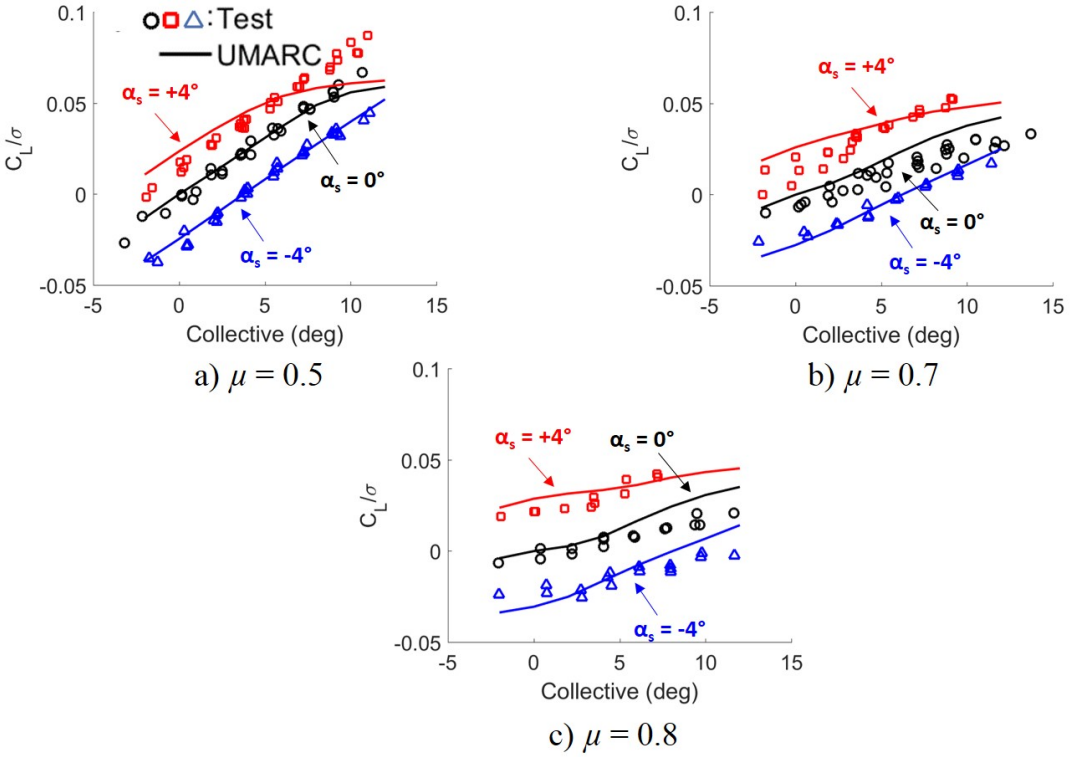


Figure 4.21: Effect of shaft tilt on rotor lift for 900 RPM and 1200 RPM.

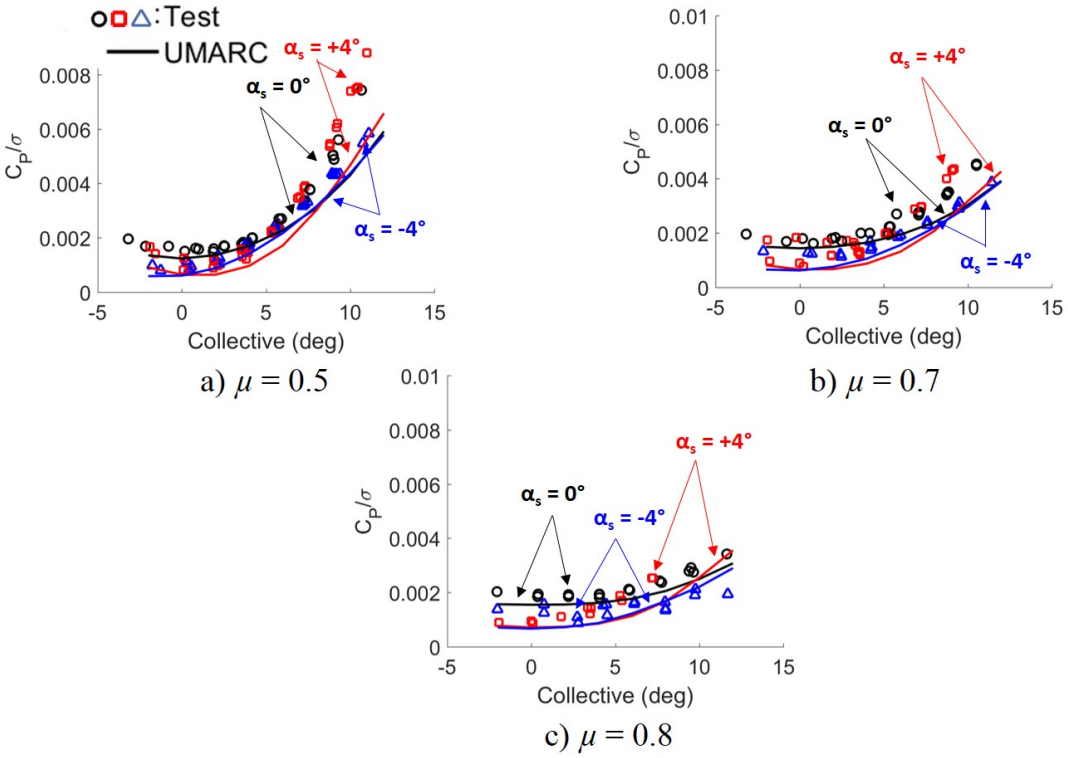


Figure 4.22: Effect of shaft tilt on shaft torque for 900 RPM and 1200 RPM.

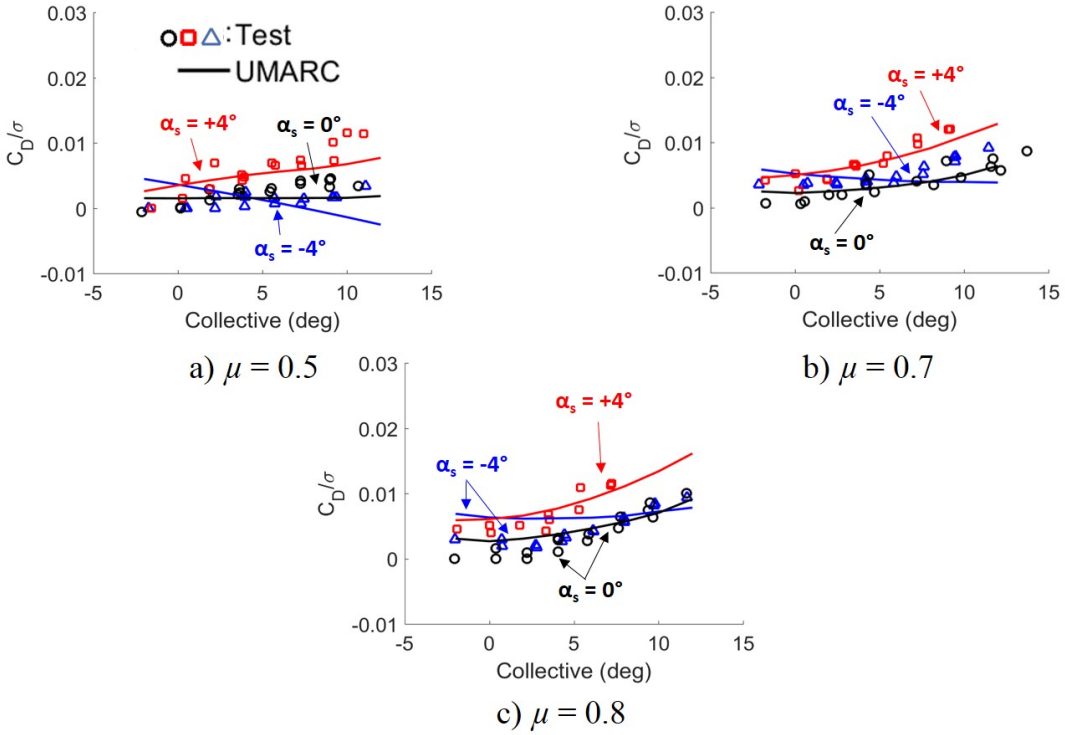


Figure 4.23: Effect of shaft tilt on drag for 900 RPM and 1200 RPM.

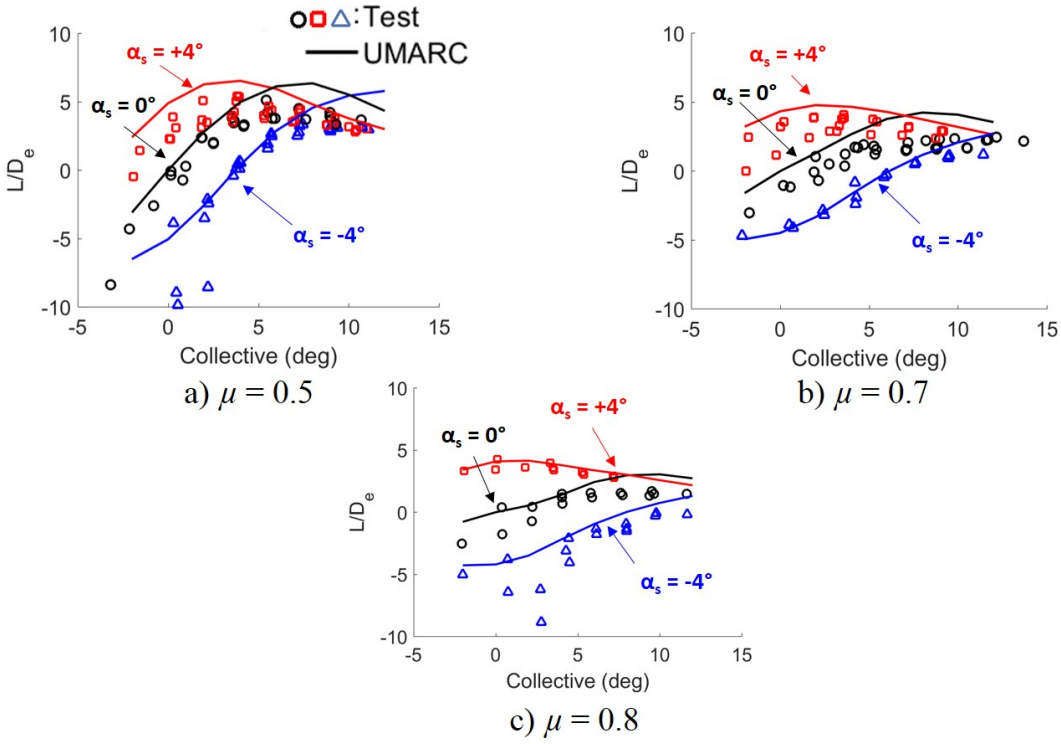


Figure 4.24: Effect of shaft tilt on rotor lift-to-drag for 900 RPM and 1200 RPM.

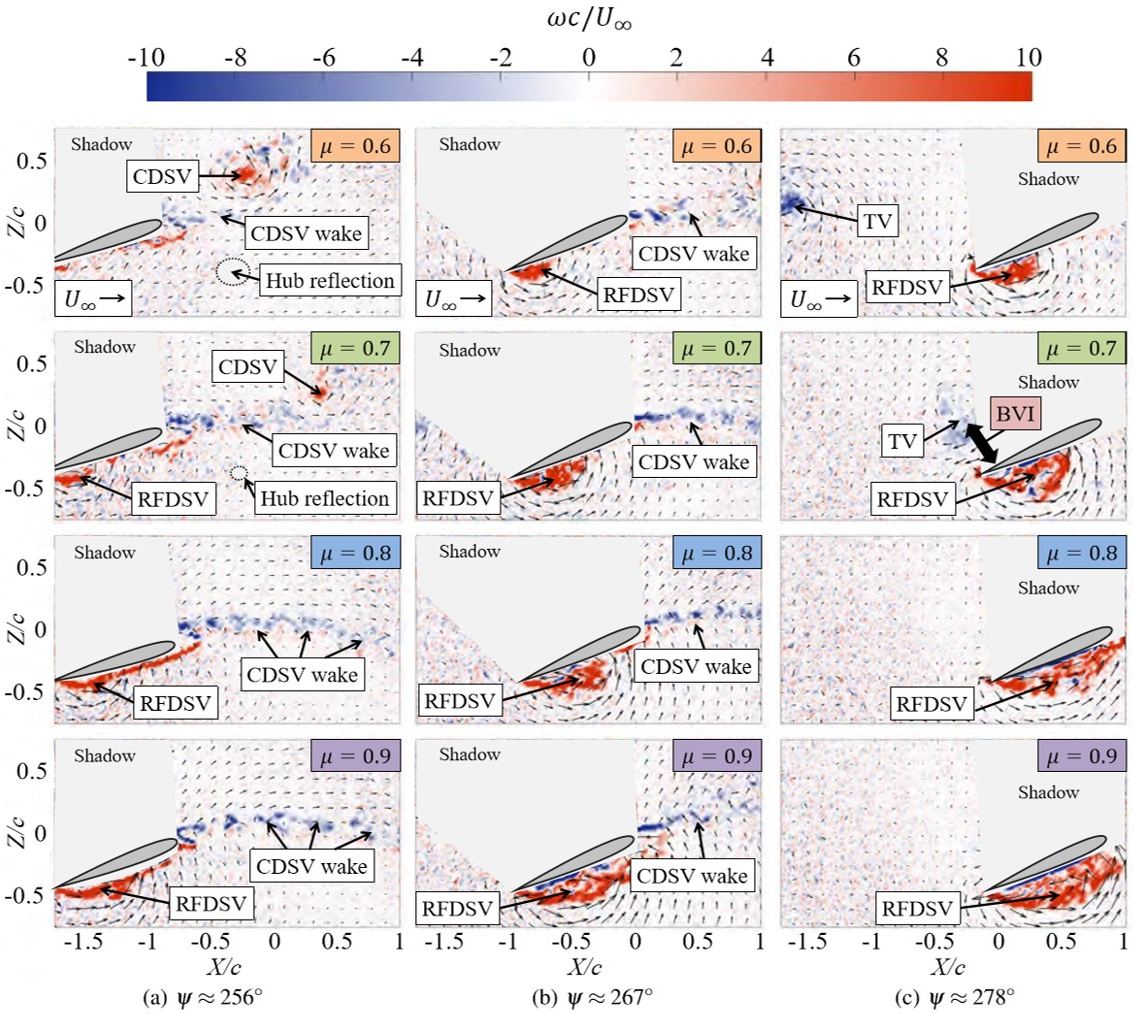


Figure 4.25: Lind et al. [45] observed the unsteady flow in the reverse flow region (40% span) of a rotor at advance ratios up to $\mu = 0.9$. A reverse flow dynamic stall vortex (RFDSV), thought to be the primary cause of unsteadiness in the reverse flow region, is evident in the time-resolved and phase-averaged PIV data. Tip vortices (TV), classical dynamic stall vortices (CDSV), and a blade-vortex interaction (BVI) are observed as well.

# Chapter 5: Conclusion

This final chapter summarizes the results of the presented work, provides a list of key contributions, and suggests alterations and additional tests to continue this work into the future.

## 5.1 Summary of Research

The purpose of this work is to further investigate the performance and vibratory loads of a Mach-scale rotor with highly similar blades at advance ratios up to 0.9. The advance ratios tested are well above the $\mu = 0.4$ limit of a conventional single main rotor helicopter, and are applicable for the design of future compound configurations.

The aeromechanics of a 4-bladed, fully articulated rotor with uniform, highly similar blades were investigated in a wind tunnel at advance ratios from 0.3 to 0.9. Collective sweeps were performed at each flight condition for 900 RPM and 1200 RPM and longitudinal shaft tilt angles of $-4$, 0, and 4 degrees. Rotor performance, vibratory hub loads, blade pitch and flap motion, and control settings were measured and used to validate predictions from the comprehensive analysis tool, UMARC. The untwisted, untapered NACA 0012 blades had a hinge offset of 6.4%R, a root cutout

of 16.4%R, and a nominal angular velocity of 2300 RPM. Collective sweeps from -2° to 12° were performed for each flight condition, and blade motion and hub forces were measured using an instrumented hub and a fixed-frame 6-component balance.

## 5.2 Key Conclusions

The following list details the key conclusions that have drawn from this research effort.

1. Non-instrumented composite rotor blades were built in-house that demonstrated no more than 2.5% variance in their structural and inertial properties, one-fourth of the variance of the instrumented rotor blades used by other researchers at the University of Maryland. Bending and torsional stiffnesses, natural frequencies, blade flap inertia, and mass distribution were successfully measured for each blade.

2. Highly similar rotor blades demonstrated significant improvement in rotor track and trim over previous tests for advance ratios up to 0.7, evidenced by a peak-to-peak flapping that was 66% less than the maximum flapping of the instrumented set of blades. Sustained dissimilarities in the blades and an imbalance in the rotor and hub, exaggerated by the high advance ratio regime, resulted in the rotor being slightly out-of-track and 0.5° outside of the original trim target for advance ratios above $\mu = 0.7$.

3. Tests at higher rotor RPMs (40-50% of the nominal hover speed of 2300 RPM) demonstrated a maximum advancing tip Mach number of 0.53, which is much

closer to the design tip Mach number of 0.60, providing more realistic performance data and drag measurements than in previous work.

4. The vibratory hub loads generally increase with advance ratio, and vertical out-of-plane forcing reaches a maximum at $\mu = 0.9$. The vertical hub load harmonics show a dominant 4/rev component and a smaller 8/rev component. A large 1/rev component in the in-plane forces indicated a mass imbalance in the rotor and hub, while the same feature in the normal force indicated an aerodynamic imbalance.

5. A comparison of rotor performance measurements to predictive results from UMARC demonstrated good overall agreement for advance ratios from 0.3 to 0.7. At high collectives, the thrust was slightly over-predicted and the power was slightly under-predicted, while the rotor lift-to-drag ratio was satisfactorily predicted. Thrust reversal was shown to occur at $\mu = 0.9$ for this rotor in both experimental and predicted results.

6. The effects of 4 degrees of positive and negative longitudinal shaft tilt on rotor performance were studied for advance ratios of 0.5, 0.7, and 0.8. Rotor lift-to-drag ratio was shown to significantly increase for lower collectives at high $\mu$ simply by adding 4° of rearward shaft tilt: a 10% increase in lift-to-drag was measured at $\mu = 0.8$ and $\theta_0 = 0°$. UMARC analyses correlated well with zero and aft shaft tilt; however, the predictions under-estimated power and overestimated thrust, which resulted in a slight over-prediction in lift-to-drag ratio.

7. A 3-D printed fuselage was designed and manufactured for this work to support future tests involving various compound configurations. A limited number of cases were run with and without the fuselage to characterize the effects on the rotor, and results indicated the fuselage induces no significant changes in rotor performance for advance ratios between 0.3 and 0.9. Lateral cyclic was affected by the fuselage at high $\mu$, and the increased slope of $\theta_{1C}$ versus $\theta_0$ was likely caused by an increased upwash over the front portion of the rotor disk.

## 5.3 Future Work

There are many opportunities to expand on the work carried out in this research, some of which are detailed in the list below.

1. **Blade similarity:** Blade similarity has been shown to have a significant effect on the track and trim state of the rotor, but does not address the potentially varied effects of different levels of uniformity and similarity. An investigation into the degree of similarity required to achieve a tracked and trimmed rotor above advance ratios of 1.0 would provide a benchmark for future testing. Non-instrumented blades also limit the data that can be measured to performance and vibratory hub loads; lessons learned could be applied to the fabrication and testing of instrumented blades with embedded pressure sensors and inset strain gauges to minimize dissimilarity in the structural and inertial properties of instrumented blades.

2. **Vibratory loads measurements:** The 1/rev component in the hub load harmonics of this work indicated a mass imbalance and a slight aerodynamic disparity in the rotor and hub, which should be carefully analyzed and mitigated in future tests. Pitch link loads would also provide a beneficial look into the oscillatory loads over the azimuth, and their measurement would not require instrumented blades. Testing at higher rotor RPMs (approximately 50%NR) may help clarify trends in vibratory loads; 1200 rotor RPM was observed to demonstrate a clear increase in magnitude with advance ratio. Additionally, a new dynamic calibration of the rotor test stand will be performed in the wind tunnel to better understand the frequency and vibratory response of the test stand mounted on the wind tunnel balance as well as its effects on the vibratory loads measurements.

3. **Rotor stability:** Difficulties experienced in trimming the rotor could be re-examined and potentially mitigated by using higher-harmonic inputs on the swashplate. At advance ratios above 1.0, when two-per-rev harmonics begin to dominate, this higher level of control would potentially allow for a more precisely trimmed rotor and provide more accurate performance and vibratory loads measurements for validation purposes.

4. **Airframe-rotor interactions:** The fuselage used in this work is designed to be used for future investigations of airframe-rotor interactions. A mathematically-derived curvature allows for accurate modeling in future CFD analysis, which could model the hub wake and the upwash on the rotor disk more accurately to

validate the UMARC lifting-line model. Additional structures such as wings or a tail rotor could also be mounted onto the fuselage, and wind tunnel tests could be carried out systematically to gain an understanding of the aerodynamic interactions of compound configurations at high advance ratios.

# Bibliography

[1] Defense Advanced Research Projects Agency. Vertical Take-off and Landing Experimental Plane (VTOL X-Plane). [Online; Accessed May 18, 2017]. `http://www.darpa.mil/program/vertical-takeoff-and-landing-experimental-plane`.

[2] C. A. Snyder, M. Robuck, J. Wilkerson, and C. Nordstrom. Summary of the Large Civil Tiltrotor (LCTR2) Engine Gearbox Study. In *Proceedings of the International Powered Lift Conference*, Philadelphia, PA, October 2010.

[3] A. Karem. Hummingbird A160 and Optimum Speed Rotor (OSR). In *Proceedings of the AHS International Specialists' Meeting - Unmanned Rotorcraft: Design, Control, and Testing*, Candler, AZ, January 2005.

[4] J. DiOttavio and D. Friedmann. Operational Benefits of an Optimally, Widely Variable Speed Rotor. *Proceedings of the 66th Annual Forum of the American Helicopter Society*, May 2010.

[5] Renata Ellington and Laurie Pierce. Contract Activity: Next Generation Rotorcraft Transmission (NGRT). Technical Report W911W6-16-2-0005, Applied Aviation Technology Directorate, March 2016.

[6] Lockheed Martin Sikorsky. X2 Technology Demonstrator. [Online; Accessed March 20, 2017]. http://www.lockheedmartin.com/us/products/x2-helicopter-technology-demonstrator.html.

[7] Lockheed Martin Sikorsky. S-97 RAIDER Demonstrator. [Online; Accessed March 20, 2017]. http://lockheedmartin.com/us/products/s-97-raider-helicopter.html.

[8] Carter Aviation Technologies. 2+2 Place Personal Air Vehicle. [Online; Accessed September 30, 2016]. http://www.cartercopters.com/pav.

[9] Airbus Helicopters. History of the X3. [Online; Accessed September 30, 2016]. http://www.airbushelicopters.com/website.html.

[10] John B. Wheatley and Manley J. Hood. Full-Scale Wind Tunnel Tests of a PCA-2 Autogiro Rotor. Technical Report NACA Report No. 515, Langley Aeronautical Laboratory, January 1935.

[11] George E. Sweet and Julian L. Jenkins. Results of Wind-Tunnel Measurements on a Helicopter Rotor Operating at Extreme Thrust Coefficients and High Tip-Speed Ratios. *Journal of the American Helicopter Society*, 8(3), 1963.

[12] Julian L. Jenkins. Wind-Tunnel Investigation of a Lifting Rotor Operating at Tip-Speed Ratios from 0.65 to 1.45. Technical Report NASA-TN-D-2628, NASA Langley Research Center, February 1965.

[13] J. L. McCloud III, J. C. Biggers, and R. H. Stroub. An Investigation of Full-Scale Helicopter Rotors at High Advance Ratios and Advancing Tip Mach Numbers. Technical Report NASA-TN-D-4632, NASA Ames Research Center, July 1968.

[14] B. Charles and W. Tanner. Wind Tunnel Investigation of Semirigid Full-Scale Rotors Operating at High Advance Ratios. Technical Report Bell Helicopter Report 576-099-010, Bell Helicopter Company, January 1969.

[15] J. R. Ewans and T. A. Krauss. Model Wind Tunnel Tests of a Reverse Velocity Rotor System. Technical Report Contract No. N00019-71-C-0506, Fairchild Republic Division, January 1973.

[16] T. R. Norman, P. Shinoda, R. L. Peterson, and A. Datta. Full-Scale Wind Tunnel Test of the UH-60A Airloads Rotor. In *Proceedings of the 67th Annual Forum of the American Helicopter Society*, Virginia Beach, VA, May 2011.

[17] R. M. Kufeld and W. G. Bousman. UH-60A Helicopter Rotor Airloads Measured in Flight. *Aeronautical Journal*, 101(1005):217–227, 1997.

[18] A. Datta, H. Yeo, and T. R. Norman. Experimental Investigation and Fundamental Understanding of a Full-Scale Slowed Rotor at High Advance Ratios. *Journal of the American Helicopter Society*, 58(2):1–17, 2013.

[19] Ben Berry and Inderjit Chopra. Wind Tunnel Testing for Performance and Vibratory Loads of a Variable-speed Mach-scale Rotor. In *American Helicopter Society 67th Annual Forum Proceedings*, Virginia Beach, VA, May 2011.

[20] Ben Berry and Inderjit Chopra. Performance and Vibratory Load Measurements of a Slowed-Rotor at High Advance Ratios. In *Proceedings of the 68th Annual Forum of the American Helicopter Society*, Fort Worth, TX, May 2012.

[21] Ben Berry and Inderjit Chopra. High Advance Ratio Wind Tunnel Testing of Two Mach-Scale Rotor Geometries. In *Proceedings of the 69th Annual Forum of the American Helicopter Society*, Phoenix, AZ, May 2013.

[22] Ben Berry and Inderjit Chopra. High Advance Ratio Wind Tunnel Testing of a Model Rotor with Pressure Measurements. In *Fifth Decennial AHS Aeromechanics Specialists Conference*, San Fransisco, CA, January 2014.

[23] Ben Berry and Inderjit Chopra. Slowed Rotor Wind Tunnel Testing of an Instrumented Rotor at High Advance Ratio. In *40th European Rotorcraft Forum*, Southampton, UK, September 2014.

[24] Ben Berry and Inderjit Chopra. Wind Tunnel Testing of an Instrumented Rotor at High Advance Ratio. In *56th AIAA Structures, Structural Dynamics, and Materials Conference*, Kissimmee, FL, January 2015.

[25] X. Wang, A. Saxena, and I. Chopra. Measurement and Validation of a Mach-Scale Rotor Performance and Loads at High Advance Ratios. In *Proceedings of*

*the 72nd Annual Forum of the American Helicopter Society*, West Palm Beach, FL, May 2016.

[26] Franklin D. Harris. Rotor Performance at High Advance Ratio: Theory versus Test. Technical Report NASA/CR-2008-215370, NASA Ames Research Center, 2008.

[27] M. Floros and W. Johnson. Performance Analysis of the Slowed-Rotor Compound Helicopter Configuration. *Journal of the American Helicopter Society*, 54(2), 2009.

[28] G. Bowen-Davies and I. Chopra. Performance and Loads Correlation of the UH-60 Rotor at High Advance Ratios. In *40th European Rotorcraft Forum*, Southampton, UK, September 2014.

[29] Graham Bowen-Davies and Inderjit Chopra. Aeromechanics of a Slowed Rotor. *Journal of the American Helicopter Society*, 60(3):1–13, 2015.

[30] M. Potsdam, A. Datta, and B. Jayaraman. Computational Investigation and Fundamental Understanding of a Slowed UH-60A Rotor at High Advance Ratios. *Journal of the American Helicopter Society*, 61(2):1–17, April 2016.

[31] Ben Berry. *Fundamental Understanding of Rotor Mechanics at High Advance Ratio Through Wind Tunnel Testing*. PhD thesis, University of Maryland, 2016.

[32] Graham Bowen-Davies. *Performance and Loads of Variable Tip Speed Rotorcraft at High Advance Ratios*. PhD thesis, University of Maryland, 2015.

[33] Mahendra J. Baghwat. Comments and Action Items from the Kick-off Meeting for the Vertical Lift Research Center of Excellence Cooperative Agreement. Technical Report W911W6-17-2-0004, Department of the Navy, January 2017.

[34] Anand Saxena. *Primary Control of a Mach Scale Swashplateless Rotor Using Brushless DC Motor Actuated Trailing Edge Flaps*. PhD thesis, University of Maryland, 2015.

[35] Jewel Barlow. Glenn L. Martin Wind Tunnel: Facilities and Specifications. [Online; Accessed March 10, 2017]. `http://www.glmwt.umd.edu/research/facilities.html`.

[36] H. J. Langer, R. L. Peterson, and T. H. Maier. An Experimental Evaluation of Wind Tunnel Wall Correction Methods for Helicopter Performance. In *Proceedings of the 52nd Annual Forum of the American Helicopter Society*, Washington, DC, June 1996.

[37] Joseph Schmaus. *Aerodynamics of a High Speed Coaxial Helicopter Rotor*. PhD thesis, University of Maryland, 2017.

[38] J. B. Barlow, W. H. Rae, and A. Pope. *Low-Speed Wind Tunnel Testing*. John Wiley and Sons, Inc., New York, NY, 3rd edition, 1999.

[39] D. H. Hodges and E. H. Dowell. Nonlinear Equations of Motion for the Elastic Bending and Torsion of Twisted Nonuniform Rotor Blades. Technical Report NASA TP-1566/AVRADCOM TR 80-A-1, NASA Ames Research Center, 1980.

[40] M. J. Bhagwat. *Mathematical Modeling of the Transient Dynamics of Helicopter Rotor Wakes Using a Time-Accurate Free-Vortex Method*. PhD thesis, University of Maryland, 2001.

[41] J. Gordon Leishman. Validation of Approximate Indicial Aerodynamic Functions for Two-Dimensional Subsonic Flow. *Journal of Aircraft*, 25(10):914–922, 1988.

[42] J. G. Leishman and T. S. Beddoes. A Semi-Empirical Model for Dynamic Stall. *Journal of the American Helicopter Society*, 34(3):3–17, 1989.

[43] J. Gordon Leishman. *Principles of Helicopter Aerodynamics*. Cambridge University Press, 2006.

[44] L. Trollinger, X. Wang, and I. Chopra. Refined Measurement and Validation of a Mach-Scale Rotor Performance and Loads at High Advance Ratios. In *Proceedings of the 43rd European Rotorcraft Forum*, Milan, Italy, September 2017.

[45] A. Lind, L. Trollinger, F. Manar, I. Chopra, and A. Jones. Flowfield Measurements of Reverse Flow on a High Advance Ratio Rotor. In *43rd European Rotorcraft Forum*, Milan, Italy, September 2017.